Numerical optimization and manufacturing of a bio-based 3D structure through robotic filament winding

Krijnen, Lotte P.J.

Award date:
2023

Numerical optimization and manufacturing of a bio-based 3D structure through robotic filament winding

Master Thesis

L.P.J. Krijnen

Eindhoven, May 2023

Final thesis version 1.0

Title	Numerical optimization and manufacturing of a bio-based 3D structure through robotic filament winding
Subtitle	Graduation Thesis for the final graduation project of the Master variant Structural Engineering and Design of the master 'Architecture, Building and Planning' at Eindhoven University of Technology
Date	May 5th, 2023
Location	Eindhoven, The Netherlands
Author	L.P.J. (Lotte) Krijnen
Student ID	1620991
Email	l.p.j.krijnen@student.tue.nl
Department	Built Environment
Master	Architecture, Building and Planning
Master track	Structural Engineering and Design
Chair	Innovative Structural Design
Graduation Committee	Ir. A.P.H.W. Habraken Assistant Professor Innovative Structural Design Ir. M.T. Ferguson EngD Innovative Structural Design Dr. Ir. S.P.G. Moonen Associate Professor Innovative Structural Design

I. Preface

The fascination for innovative structural engineering started during my bachelor's degree. I set up a parametric script that automates the design of a steel distribution centre. By setting parameters to desired dimensions, a geometrical and structural design of a steel hall was generated in Grasshopper. By one click, the full model including connections could be exported to Tekla Structures, IDEA StatiCa and SCIA Engineer. During this bachelor's graduation project, I experienced the possibilities of parametric design in Grasshopper. I saw opportunities for the built environment to optimize and automate processes, to reduce environmental impact and time and labour intensiveness. When I started my master's at TU/e, I was immediately interested in the Form And Material Optimization (FAMO) atelier of Ir. A.P.H.W. Habraken. During an exploratory meeting for graduation research topics, the research project to design an optimized lightweight structure of biobased materials came up. The structure had to be numerically optimized for axial compression, and manufactured by robotic filament winding. This project combined all of my interests in innovative techniques, optimization and automation. Furthermore, considering the environmental pollution caused by current engineering processes, it was interesting to research the application of biobased sisal rope for structural purposes.

This research project is part of the Form And Material Optimization atelier within the chair of Innovative Structural Engineering and Design. This project aims to design an optimized lightweight structure of biobased material through robotic filament winding, to limit environmental pollution and create opportunities for structural design. This graduation project is part of the master track Structural Engineering and Design within the master Architecture, Building and Planning at TU/e.

I would like to thank the graduation committee for their guidance throughout the project. Special thanks to Ir. A.P.H.W. Habraken for his enthusiasm towards the project, and for his weekly feedback which was very helpful. Ir. M.T. Ferguson especially for sharing his knowledge regarding robots, and providing help during the test manufacturing phase. Dr. Ir. S.P.G. Moonen for his commitment, and for sharing his knowledge regarding biobased materials and robotic filament winding reference projects. Also, I would like to thank the staff from the SED lab for their support and involvement throughout the manufacturing and test phase of the project. Lastly, a special thanks to my colleague students. V.B. Staat for his commitment throughout the project, and for brainstorming together. L.M.J. Roex, D. Jansen and R.T. Damoiseaux for their helping hands during the winding process.

II. Summary

In this research, an optimized three-dimensional lightweight structure is designed to transfer an axial compressive force. The structure is manufactured through robotic filament winding using bio-based sisal rope. The presented work investigates the application of resin-impregnated biobased sisal rope for structural purposes.

To find the optimized column design, a numerical optimization is set up in the parametric modelling software Rhinoceros, through a script written in the visual programming plug-in Grasshopper. This optimization is divided into two parts, namely, a geometrical optimization and a sizing optimization. The Multi-Objective Evolutionary Optimization plug-in Octopus is used to find an optimized design that is maximized in buckling resistance and minimized in internal elastic energy and mass. After this, a sizing optimization is conducted based on the strain energy. This optimization is an iterative process that optimizes the number of ropes for each line.

The optimized design is manufactured through robotic filament winding using 4 mm three-strand sisal rope, impregnated with SR InfuGreen 810 / SD 8824 epoxy resin. Robotic filament winding with bio-based materials provides opportunities for the built environment to create innovative structural elements in a fully digitized manufacturing process. Moreover, the combination of numerical optimization, innovative structural design and robotic filament winding with bio-based materials, allows to design and manufacture lightweight structures with a large degree of freedom. This can result in reduced environmental pollution caused by the construction sector's traditional design and manufacturing processes.

After manufacturing, the fibre composite columns were stored for a maximum of 20 hours at 20 degrees Celsius, after which they were post-cured at 40 degrees Celsius for 8 hours. Column imperfections such as skewing were noticed, caused by the manually attached formwork. Furthermore, some columns felt somewhat sticky as a result of the hardener reacting with carbon dioxide and moisture while being stored at ambient temperature before post-curing.

The manufactured fibre composite columns were tested in axial compression, which resulted in a maximum compressive strength of 21.4 kN. The numerical result for the buckling load factor was 1.87 times higher than the average force at which local buckling started to occur. Since the filament-winded columns are not one single element but an interaction of multiple elements, local buckling occurs before the column buckles globally.

From this research, it can be concluded that it is feasible to manufacture a numerically optimized column design through robotic filament winding using biobased sisal rope. Besides some imperfections, the structural behaviour of the winded columns was promising. Further research should be conducted to reduce imperfections and conclude whether robotic filament winding with sisal rope is suitable for large-scale structural purposes.

Table of contents

1 Introduction 7

2 Design 9

2.1 Design scope 9

2.2 References 9

2.3 Literature study 10

2.4 Parameters 12

3 Materialization 14

3.1 Natural sisal fibre 14

3.2 Epoxy system 15

3.3 Mechanical properties 16

4 Production method 17

4.1 Robot 17

4.2 End effector 18

4.3 Filament winding process 19

4.3.1 Resin impregnation 20

4.4 Curing 21

5 Numerical optimization 22

5.1 Optimization goal 22

5.2 Process model 23

5.3 Structural analysis 24

5.4 Geometrical optimization 25

5.4.1 Final geometrical design 26

5.4.2 Verification structural analysis 27

5.5 Sizing optimization 28

5.6 Eulerian winding path 30

5.7 Robot Components 31

5.8 Robot Studio 32

6 Manufacturing 33

6.1 Formwork design 33

6.2 Robotic filament winding 36

6.3 Curing cycle 37

6.4 Final elements 38

6.5 End node design 39

7 Testing 40
8 Test results 41
8.1 Column 1 41
8.2 Column 2 44
8.3 Column 3 45
8.4 Column 4 47
8.5 Results overview 49
9 Discussion of the results 50
10 Conclusions 52
11 Recommendations 54
Bibliography 56
List of figures and tables 60
Appendixes 62

1 Introduction

Ever since the beginning of the Industrial Revolution, numerous countries around the world experienced economical and industrial growth, which increased worldwide environmental pollution significantly (Ahmed, 2022). The growing construction industry contributes to a large extent to this environmental pollution, concerning energy consumption, greenhouse gas emissions, waste generation and material depletion (Amziane & Sonebi, 2016). Moreover, the construction sector causes 36% of the energy consumption and 39% of the greenhouse gas emissions produced globally (Crawford, 2022). Already a third of these emissions is generated by the production process of steel and cement (Fennell et al., 2022). Considering The Netherlands, almost a quarter of the total CO_2-emissions produced during the first quartile of 2022 was generated by the built environment only (Statistics Netherlands, 2022). Hence, the environmental contamination caused by the built environment needs to be reduced to create a healthier environment. Therefore, the Dutch government set a goal in line with the internationally established 2030 Sustainable development goals and the Paris Agreement, for the Dutch economy to be completely circular by 2050 (Ministry of Infrastructure and Water Management, 2021).

Increasing the use of bio-based materials in the construction sector can reduce environmental pollution. Bio-based materials are composed of renewable resources, which contribute to a circular economy that aims to maximize the worth of resources and to limit the generation of waste by regenerating materials at the end of their lifecycle (Sustainability of bio-based materials in a circular economy, n.d.). In addition, reusing and recycling materials reduces material depletion and lowers the amount of greenhouse gas emissions normally generated during the production process of non-renewable materials. Consequently, the utilization of primary resources reduces, and the lifespan of existing materials extends. Nevertheless, the building industry is hesitant in implementing bio-based materials due to the lack of test results and therefore relatively unknown material properties (Habraken, 2021). Experimental testing with bio-based materials is required to be able to guarantee structural safety.

Furthermore, sustainability can be improved by reconsidering the structural design and manufacturing process. Traditional design methods are time and labor intensive, which involve high costs. Moreover, structural designs often get over-dimensioned due to limited accuracy and prescribed shapes and dimensions in production, which limits design freedom and the ability to optimize material use. Hence, digitizing the design process reduces time and labor intensiveness, guarantees accuracy, and allows for a higher level of design complexity and optimization processes. Consequently, using optimization processes allows for designing lightweight structures, which are minimized in mass and maximized in stiffness. Besides digitizing the design process, robotics can be used to automate the manufacturing process as well, which reduces labor intensiveness and allows to manufacture complex structures with a large degree of freedom.

This research aims to design an optimized three-dimensional lightweight structure to transfer an axial compressive force, and to manufacture this structure by robotic filament winding using bio-based sisal rope. This project is part of the Innovative Structural Engineering and Design (ISD) field and focuses on minimizing material use and integrating architectural and structural design. The research question of this project is formulated as follows:

'How can an axially loaded, bio-based, three-dimensional structure be manufactured by robotic filament winding and be optimized through numerical optimization?'

The numerical optimization will be performed in the parametric modelling software Rhinoceros (Rhino), through a script written in the visual programming plug-in Grasshopper. While changing geometrical parameters, the script searches for an optimized lightweight structure to take an axial compressive force. After the numerical optimization, the structure will be manufactured out of bio-based sisal rope through robotic filament winding. The final product is an optimized robotically filament-winded structural column, tested in axial compression.

Robotic filament winding with bio-based materials provides opportunities for the built environment to create innovative structural elements in a fully digitized manufacturing process. Moreover, the combination of numerical optimization, innovative structural design and robotic filament winding with bio-based materials, allows to design and manufacture lightweight structures with a large degree of freedom. As a result, environmental pollution caused by the traditional design and manufacturing processes of the construction sector, can be reduced.

2 Design

2.1 Design scope

For this research project, a lightweight simply supported fibre composite column of one meter is designed and robotically fabricated through filament winding. The structural column is optimized for axial compression and manufactured using bio-based sisal rope, which distinguishes the project from previously conducted research. Furthermore, the column must be able to be part of a spaceframe, which implies that the design of end nodes is included. Figure 1 provides a schematized representation of the research question, where the dotted line represents the optimized filament-winded structure to be designed.

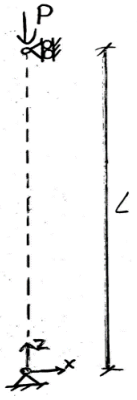

Figure 1 Schematization research question

2.2 References

Figures 2 to 7 show six robotically fabricated lightweight fibre composite structures, designed by the architect and professor Achim Menges in corporation with the Institute for Computational Design (ICD) and the Institute of Building Structures and Structural Design (ITKE) at the University of Stuttgart. The research pavilions are a result of years of biomimicry research in architecture, and represent the combination of advanced computational technologies with structural principles found in nature (Menges, 2019).

Figure 2 Left: ICD/ITKE Research Pavilion 2012 (Arch2O, 2020)
Figure 3 Right: ICD/ITKE Research Pavilion 2013-14 (Fredrickson, 2014)

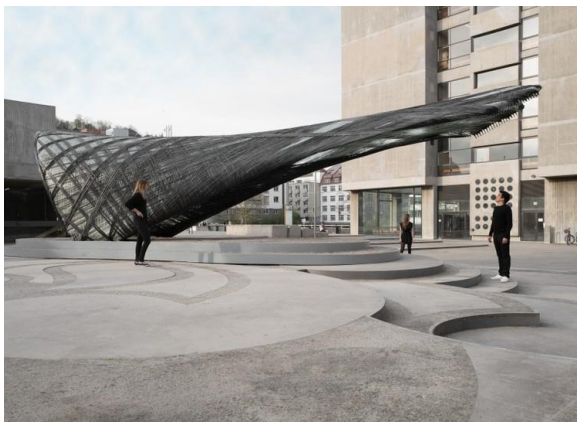

Figure 4 Left: ICD/ITKE Research Pavilion 2014-15 (Halbe, 2016)
Figure 5 Right: ICD/ITKE Research Pavilion 2016-17 (Burggraf / Reichert, 2017)

Figure 6 Left: Elytra Filament Pavilion, Victoria & Albert Museum (Halbe, 2016)
Figure 7 Right: BUGA Fibre Pavilion 2019 (Halbe, 2019)

The University of Stuttgart highlighted three items that are of importance for robotically filament-winded structures. First, robotic filament winding is a tension-driven process with fibers spanning between anchor points or contact points with other fibers. Since fibers are stronger in tension and prone to buckle in compression, the fiber use in tension should be maximized at all times. Secondly, the fiber span should be reduced to increase the buckling strength, which can be done using fiber interlocking. Thirdly, adding surface curvature perpendicular to the stress direction increases the buckling strength. Furthermore, a robotic winding path is defined by a single start and end point, which implies that horizontal tension rings to increase the strength could not be manufactured since they interrupt the winding path (J. Christie et al., 2021).

A study on lightweight structures, conducted by Beukers & Hite (2013), also shows that nature can be used as inspiration for structural design, since nature uses a minimum amount of energy. This principle can be seen in the shape of a tree, which is based on the history of loading. Therefore, lightweight structures should be designed based on the flow of forces to minimize energy and material use.

2.3 Literature study

The governing failure mechanism of slender structures loaded in axial compression is buckling (Vellaichamy et al., 2019). Buckling can be seen as a sudden failure of the structural member, occurring before the ultimate compressive stresses in the material are reached (Chem Europe, n.d.). The German-Swiss mathematician Euler analyzed buckling in the 18th century and established several Euler conditions to predict the critical load. Figure 8 shows the buckling shape and formula to predict the critical load for a simply supported column loaded in axial compression (Beukers & Hite, 2013). Since the length of the pin-ended column is set to one meter, the critical length will also be one meter. This in turn means that the critical load is only depending on 2 variables: the Young's modulus of the material and the moment of inertia of the cross-section. Moreover, the moment of inertia is the only parameter that can be affected by the column design. An increased moment of inertia results in a directly proportional increase of the critical load. The moment of inertia can be increased by distributing the material as far from the principal axes of the column as possible, while the wall thickness remains thick enough to prevent local buckling (Chem Europe, n.d.). Consequently, columns with a tubular cross-section result in a higher critical load and therefore buckling resistance.

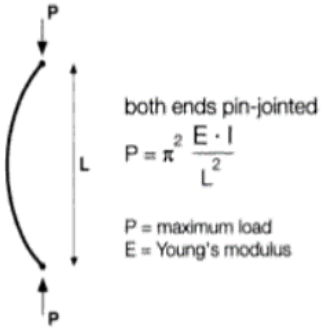

Figure 8 Euler buckling shape and formula to predict critical load (Beukers & Hite, 2013)

Inspired by the book of Beukers & Hinte (2013), Pawlyn (2016) researched biomimicry in architecture. As a result of this research, Pawlyn shows Figure 9 which represents four equally stiff columns, loaded in axial compression. By using shape and material optimization, it can be seen that a convex-shaped column with a circular hollow cross-section has the same stiffness as a column with a solid squared cross-section, while only using 14% of the material. The shape of the optimized column is based on the flow of forces for axial compression. Furthermore, material is placed where the highest stresses occur and where high bending resistance is required, which refers to the Euler buckling shape of Figure 8.

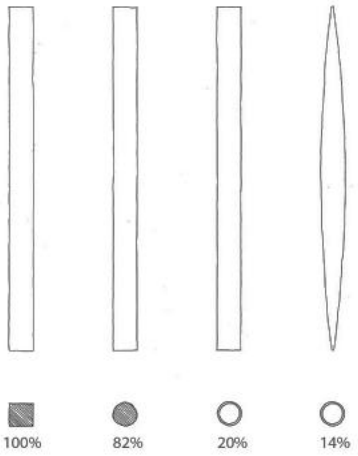

Figure 9 Four equally stiff elements using shape and material optimization (Pawlyn, 2016)

A 2D topology optimization with the Interactive 2D TopOpt App was conducted to analyze the flow of forces for an axially loaded column. The App wants to maximize stiffness while looking for the optimal material distribution within the defined boundary conditions. The top of the structure is subjected to a point load, axially placed above a support. Figure 10a shows the result of the typology optimization, where it can be seen that a convex-shaped structure is created to travel the applied force to the support. Furthermore, the cross-sectional area of the structure increases towards the middle of the column, where the highest resistance against buckling is required.

The Karamba3D plug-in was used to conduct a 2D Finite Element Analysis (FEA) in Grasshopper to get insight into the flow of forces and principle stresses. A simple 2D surface with a point load and support is created in Rhinoceros. The result of the FEM-analysis can be seen in Figures 10b to 10e. Figure 10b visualizes the flow of forces and Figure 10c the principle stresses, where red represents compression and blue represents tension. It can be observed that the same convex shape occurs, similar to the result of the topology optimization. Furthermore, the result of the FEM-analysis and typology optimization verify the research conducted by Beukers & Hinte (2013) and Pawlyn (2016). As a result of these findings, the Grasshopper script should be able to generate a convex-shaped column. Section 2.4 Parameters elaborates on the required parameters to generate this shape.

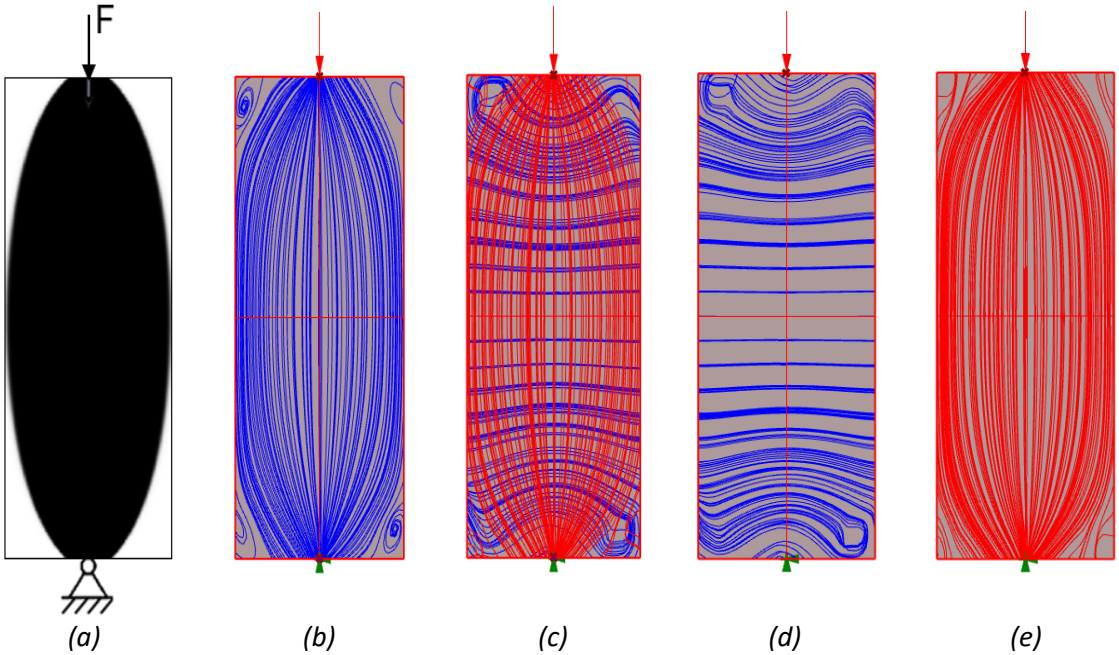

Figure 10 (a) Typology optimization (b) Flow of forces (c) Principle stresses (d) Tensile stresses (e) Compressive stresses

2.4 Parameters

The numerical optimization is performed in the parametric modelling software Rhinoceros, through a script written in Grasshopper. The first part of the Grasshopper script defines the geometry of the structural column, which can be influenced by six different parameters that are defined based on the conducted literature study.

The first parameter defines the number of nodes that will be placed on a line with a predefined length of one meter, visualized in Figures 11a and 11b. In a larger stage, auxiliary rings will be created around these nodes, to wind the sisal rope around. This parameter can be used to set the base shape of the column. For a straight column, only two nodes are required, however, to create a convex-shaped column the number of nodes should be increased. The maximum number of nodes is set to nine due to practical reasons.

The second parameter sets the height of each node, which provides the opportunity to create different types of convexity. Since the column will be simply supported and axially compressed, there will be symmetry over midspan. Therefore, only three different heights can be set, visualized in Figure 11c as heights Z1, Z2 and Z3.

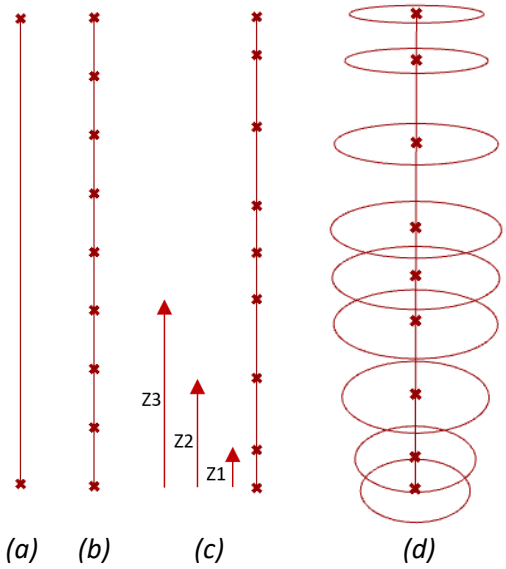

Figure 11 Parameters to determine base geometry

From the literature study it was found that adding surface curvature perpendicular to the stress direction increases the buckling strength (J. Christie et al., 2021). Furthermore, research conducted by Pawlyn (2016) showed that using a circular hollow cross-section decreases the amount of material to a large extent, while the stiffness remains equal. Moreover, a tubular cross-section can increase the moment of inertia and therefore also the buckling resistance of the column (Chem Europe, n.d.). As a result of these findings, the Grasshopper script creates circles around the generated nodes. The third parameter defines the radius of each circle, which provides the design freedom to generate either straight, concave or convex-shaped columns. After these first three parameters, the base geometrical shape of the column is determined. Figure 12 visualizes different geometries that the script is able to generate.

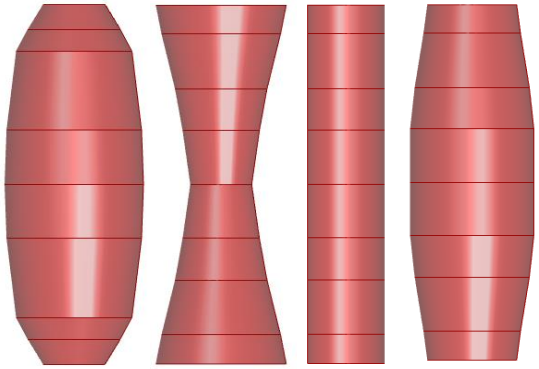

Figure 12 Examples of geometrical shapes that can be generated by the Grasshopper script

After defining the geometrical shape, parameters four to six define the rope design. First, the fourth parameter defines the number of nodes that will be placed on the generated circles, which is a single value equal to all circles. A minimum value of six nodes is set to this parameter to guarantee a certain level of complexity in the model. Furthermore, the maximum amount of nodes is set to 20 for practical reasons and to prevent an overcomplicated rope design. When the number of nodes is defined, vertical lines are created along the column length, crossing the created nodes, visualized in Figures 13a and 13b.

Next, diagonal lines are created as geodesic curves between two nodes over the circular surface that is created between two circles, visualized by Figures 13c and 14. The fifth parameter influences the angle of the diagonal lines by setting a value to the number of nodes a diagonal line has to shift, for each circular surface. If this value is set to zero, the lines run vertically to the node straight above. If the value is set to one, the lines run in a clockwise manner to the next node in the ring above. Figure 13e visualizes an example where the diagonals shift a different amount of nodes between different circles, varying between two and three nodes. The script can also create diagonal lines spanning from the first circle directly to the third, fourth or fifth circle, skipping the intermediate circles (Figure 13d). The last and sixth parameter generates diagonals that shift the same amount of nodes between two circles, over the whole column. Figure 13f shows an example geometry where all diagonals shift one node between each circle. After creating all geodesic curved lines, the lines are cut at the intersections with the vertical lines and replaced by straight line elements as shown in Figure 14. This is done since robotic winding is a tension-driven process where fibers span between anchor points or contact points. The diagonal lines will always be winded over the vertical lines to maximize the number of contact points and reduce the fibre span, to increase buckling resistance.

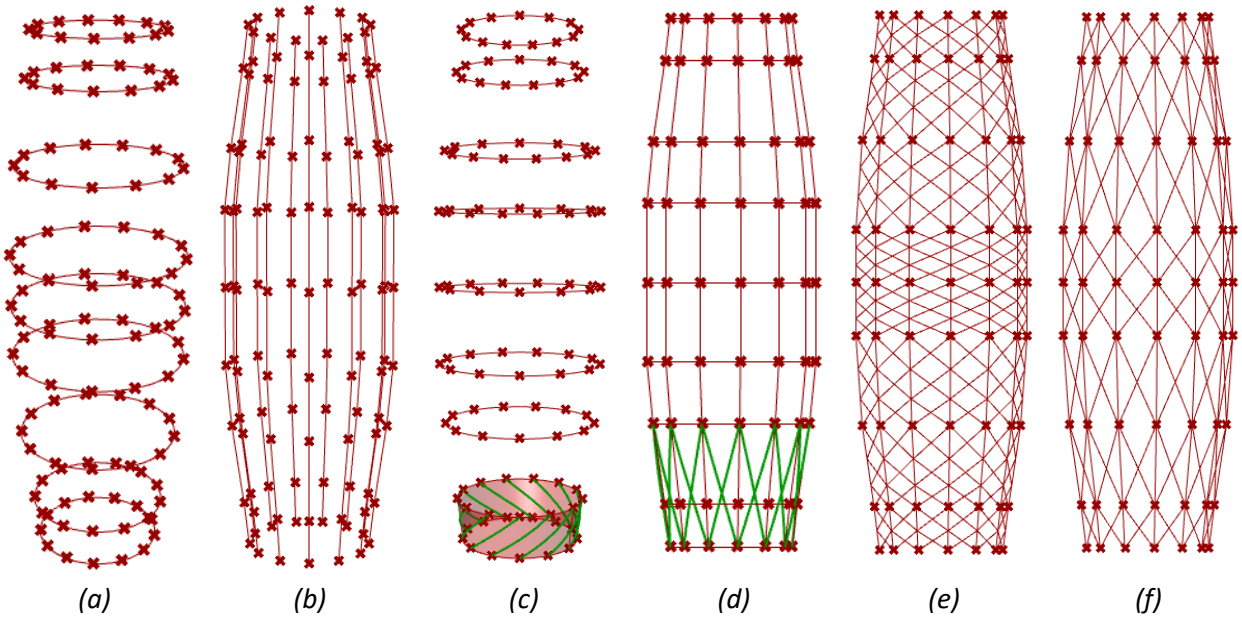

Figure 13 Parameters to determine wire design

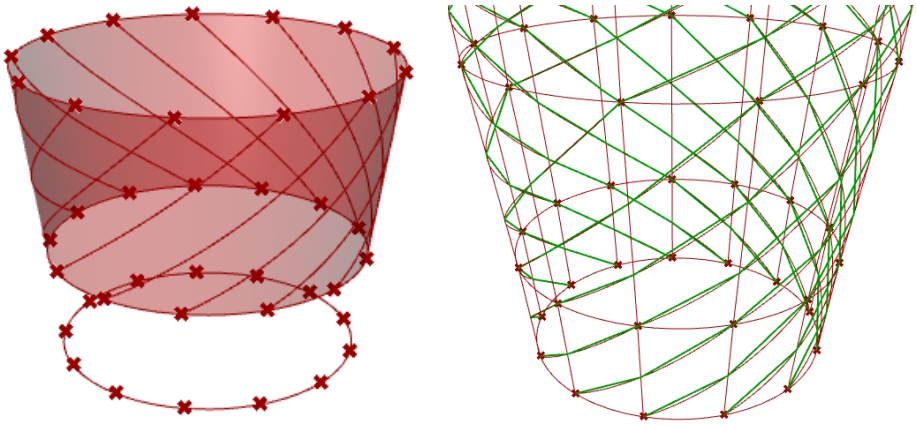

Figure 14 Convert geodesic lines into straight lines between intersection points with vertical lines

3 Materialization

3.1 Natural sisal fibre

This research focuses on the application of bio-based sisal rope for structural purposes. The hierarchical structure of a rope is visualized in Figure 16. Sisal rope is made from natural sisal fibre, which can be derived from the leaves of the Agave sisalana plant. The fibres are renewable, biodegradable, and abundantly available (Zhang et al., 2014). Natural fibres such as sisal fibre characterize unidirectional properties and a high tensile strength, which is why they are mostly used for structural purposes such as ropes and reinforcement. Furthermore, due to their low density and high strength-to-weight ratio, natural fibers create opportunities for the built environment to design and manufacture lightweight structures (Karimah et al., 2021). A large variety of natural fibers is therefore also used for robotic filament winding.

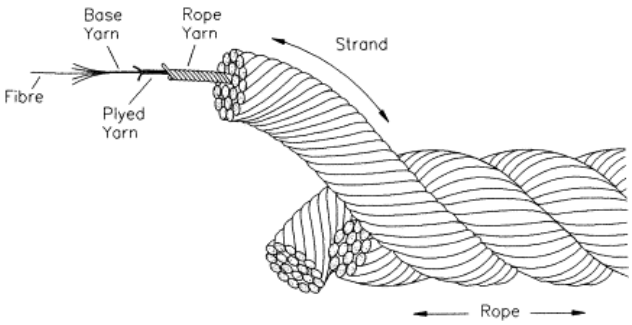

Figure 16 Hierarchical structure of sisal rope made from natural fibres (Leech, 2002)

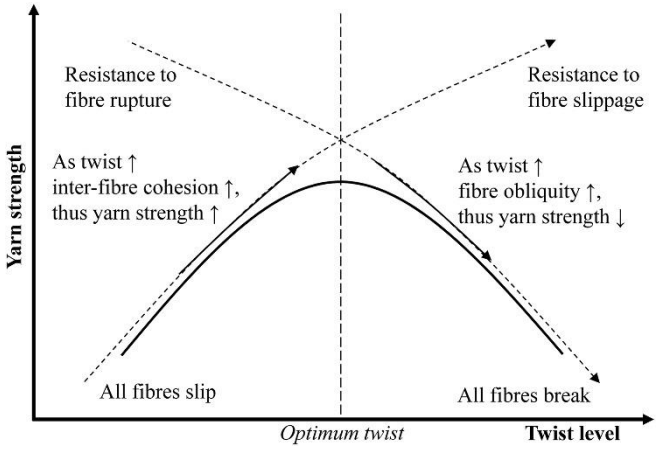

Figure 15 Effect of yarn twist on the tensile strength (Shah et al., 2013)

Since natural fibres derive from nature, the cross-section throughout the fibre length and mechanical properties can vary strongly due to the growth location and environmental conditions during growth such as rainfall (Jawaid et al., 2019). Natural fibres characterize a high moisture absorption compared to glass and carbon fibres, which is why the latter can strongly influence the mechanical properties (Zhang et al., 2014). Furthermore, the mechanical properties of woven fibers highly depend on the yarn twist, fiber orientation and fiber cohesion (Palaniswamy & Mohamed, 2005). Figure 15 shows the effect of the yarn twist on the tensile strength. It can be seen that increasing the yarn twist up to the optimum twist level increases the fibre strength by improving the inter-fiber cohesion. Next to the optimum twist level, fibre obliquity effects are significant which causes a decrease in yarn strength. The varying mechanical properties of natural sisal fibre are presented in Table 1.

Table 1 Differences in mechanical properties of natural sisal fibre

Reference	Density [g/cm^3]	Tensile strength [MPa]	Elastic modulus [GPa]
(Väisänen, Das & Tomppo, 2017)	1.5	100-800	9-22
(Idicula, Joseph & Thomas, 2009)	1.45	350	3.8
(Jawaid et al., 2019)	1.33-1.5	400-700	9-38

3.2 Epoxy system

For this research, a three-dimensional structural column of one meter will be manufactured of bio-based sisal rope, impregnated with epoxy resin. The type of resin used can have a significant influence on the strength of the material. Furthermore, the properties of the resin should fit the needs of the manufacturing and curing process.

The main criteria for selecting resin are the gelling time, viscosity, exothermic peak temperature, and hardening temperature (Lepelaar, Hoogendoorn, Blok, & Teuffel, 2016). The gelling time and viscosity influence the manufacturing process, while the exothermic peak temperature and hardening temperature affect the curing cycle after manufacturing. Louer (2022) compared four types of epoxy systems with possible hardeners based on these four main criteria, availability and the e. The four systems are the SuperSap CLR Bio Epoxy, Resoltech 1800 ECO, SR GreenPoxy 56 and SR InfuGreen 810 epoxy system. As a result of this study, the SR InfuGreen 810 with SD 8824 hardener was used for manufacturing. For this research, the curing cycle and carbon green content are added to the criteria list as well. The carbon green content of the four systems Louer (2022) compared, is presented in Table 2.

Table 2 Carbon green content for different epoxy systems

Epoxy system	Carbon green content	Reference
SuperSap CLR Bio Epoxy	17-21%	(*Technical Data Sheet SUPER SAP® CLR Epoxy System*, 2013).
Resoltech 1800 ECO	33%	(*Bio-Epoxy Infusion 1800 ECO*, n.d.)
SR GreenPoxy 56	50-58%	(Sicomin Epoxy Systems, 2015)
SR InfuGreen 810	35-41%	(Sicomin Epoxy Systems, 2017)

With an average carbon green content of 38%, SR InfuGreen 810 epoxy resin has a relatively low environmental impact compared to standard epoxy systems (Sicomin Epoxy Systems, 2017). Table 2 shows that the SR GreenPoxy 56 system has a lower environmental impact with an average bio-based carbon content of 54%. However, SR GreenPoxy 56 was found to have a relatively high viscosity compared to the SR InfuGreen 810 (Sicomin Epoxy Systems, 2015). The two-component epoxy system SR InfuGreen 810 has a low viscosity at an ambient temperature of 20 degrees Celsius, which enhances the workability during winding. Furthermore, the curing cycle of the SR GreenPoxy 56 takes at least 36 hours at three different temperatures. In contrast, it takes only eight hours at 40 degrees Celsius for the SR InfuGreen 810 system to cure.

The structure will be cured in the climate room of the Structural Engineering and Design (SED) lab, during opening hours. Therefore, a curing cycle of more than eight hours at different temperatures is not feasible. The carbon green content, low viscosity, short curing cycle, availability, and acceptable price make the SR InfuGreen 810 an appropriate epoxy system for this specific research. Moreover, the SR InfuGreen 810 / SD 8824 system is previously used at TU/e during research conducted by Louer (2022), Jansen (2021), and Janssen and Roex (2022). Test results gained during this research can be used as a reference for this project. Therefore, the bio-based sisal rope is impregnated with the two-component epoxy system SR InfuGreen 810 with SD 8824 hardener. The technical datasheet of the Sicomin epoxy system is added to Appendix 1 Sicomin technical datasheet.

3.3 Mechanical properties

Recent graduates of Eindhoven University of Technology conducted material tests with sisal rope of Ø 4 mm and robotically winded several two-dimensional elements. The results of these tests are used as a reference to determine the mechanical properties for the numerical optimization.

Louer (2022) conducted four tensile tests on single fiber specimens and three tensile tests on bundled fibre specimens, varying between 26 and 52 fibres bundled. All tests were conducted with sisal rope Ø 4 mm cured with Sicomin SR InfuGreen 810 epoxy resin and SD 8824 hardener. Table 3 provides the values for the breaking strength and Young's modulus, resulting from the stress-strain diagrams.

Table 3 Tensile test results of single fibre and bundles fibre specimens of sisal rope Ø 4 mm cured with Sicomin SR InfuGreen 810 epoxy resin and SD 8824 hardener (Louer, 2022)

Test	Type of test	Breaking strength [MPa]	Young's modulus [MPa]
1	Single fibre	163.90	5598.77
2	Single fibre	131.65	4691.07
3	Single fibre	100.66	5035.92
4	Single fibre	117.40	5035.92
5	Bundled fibres	57.28	2300.97
6	Bundled fibres	77.74	3548.07
7	Bundled fibres	54.94	1687.54
Average of seven tensile tests		100.51 MPa	3985.46 MPa

From Table 3, a wide variety of results can be observed. It can be seen that the tensile strength and Young's modulus of the test specimens are relatively low compared to the basic mechanical properties of bio-based sisal fibre, provided in Table 1. These decreased mechanical properties can be caused by the yarn twist, fibre cohesion, or environmental conditions as discussed in Section 3.1 Natural sisal fibre. Furthermore, the breaking strength and Young's modulus are relatively lower for bundled fibres than for single fibre specimens. Research conducted by Hurk (2020) shows that a decreased Young's modulus can be caused by an increased moisture content. Natural fibres characterize a high moisture absorption, which increases with increasing fibre content (Ramakrishnan et al., 2022). The lowered breaking strength and Young's modulus of bundled fibre specimens can therefore be caused by an increased moisture content.

Besides the increased moisture absorption, many fibres bundled together can result in a high exothermic peak temperature. This is the peak temperature reached during the chemical reaction between the SR InfuGreen 810 and the SD 8824 hardener. A high exothermic peak temperature should be prevented to prevent damage to the fibres (Lepelaar, Hoogendoorn, Blok, & Teuffel, 2016). Therefore, in the numerical model, a maximum value will be assigned to the number of fibres bundled.

For this research, the same material is used as the material Louer (2022) used to conduct tensile tests, namely, sisal rope of Ø 4 mm cured with Sicomin SR InfuGreen 810 / SD 8824. The average tensile strength and Young's modulus of the seven tensile tests will be used as a guideline for the numerical model. Therefore, in the numerical evaluation, a tensile strength of 100 MPa and a Young's modulus of 4000 MPa will be taken into account. After testing, the results of the numerical model will be compared to test results.

4 Production method

The optimized structural element will be manufactured through robotic filament winding: a manufacturing process where resin-impregnated uncured fibres are sequentially wrapped around a minimal formwork, following a given path. Filament winding is a tension-driven process where fibers span between anchor points or contact points with other fibres. Figure 17 visualizes two types of filament winding, namely, filament winding around a mandrel and coreless winding. To be able to wind a tubular element, a rotating mandrel is often used to wind the fibres around (Figure 17a). The mandrel is then connected to a moveable work object that communicates with the robot. This principle is used to manufacture composite products such as vessels, shafts and tubes (Ma et al., 2019). Figure 17b schematizes coreless filament winding, a manufacturing method where the full surface mandrel is reduced to anchor points arranged on a linear scaffolding (Estrada et al., 2020). The elements of the BUGA fibre pavilion 2019 are produced by coreless robotic filament winding, as shown in Figure 18.

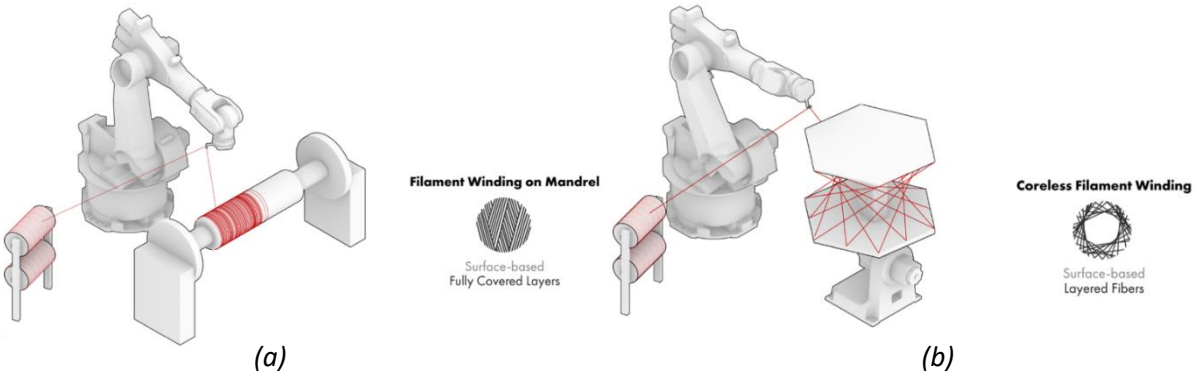

Figure 17 Schematization (a) filament winding on mandrel (b) coreless filament winding (Estrada et al., 2020)

Figure 18 BUGA Fibre Pavilion 2019 elements produced by coreless filament winding (urbanNext, 2023)

For this research, a convex-shaped column will be manufactured. To create this shape, a minimal non-structural core is required. The formwork will be connected to a moveable work object, which makes sure the structure is rotated to its correct position, while the robot only moves from left to right along the column length. Section 6.1 Formwork design further elaborates on the design of the non-structural core.

4.1 Robot

The robot used for manufacturing is ABB IRB 1200-5/0.9 with a reach of 0.9 meter. This robot is available for manufacturing in the Structural Engineering and Design lab at TU/e. Appendix 2 Product specifications ABB IRB 1200-5/0.9 provides technical information on the specific robot (ABB, 2022).

Considering the robot's reach and the dimensions of the structural column, the formwork is placed horizontally on the robot bed, connected to the moveable work object at one end. The moveable work object represents the rotation table that communicates with the robot during winding. The location of the robot and rotation table are calibrated. This data provides input for Robot Components and Robot Studio. Figure 19 shows a Robot Studio illustration of the robot and the rotating table, placed on the robot bed.

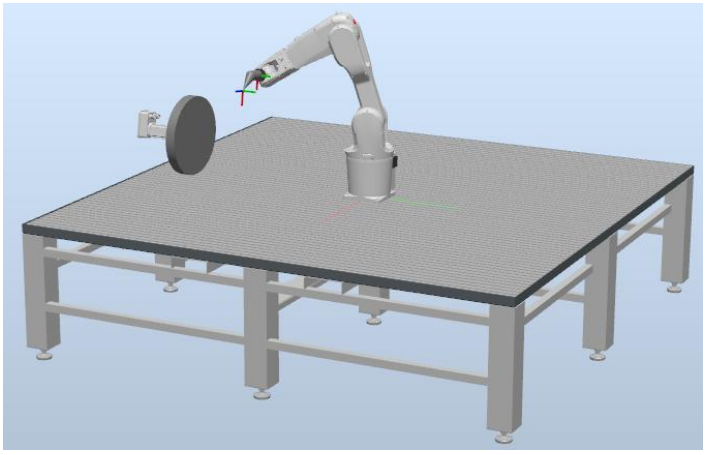

Figure 19 Robot Studio illustration of ABB IRB 1200-5/0.9 and rotation table placed on robot bed

4.2 End effector

An end effector is a device that is attached to the end of the robot arm, allowing the robot to interact with the environment. For this research, it should be able to guide the resin-impregnated rope to specific target points.

Since filament winding is a tension-driven process, the end effector should be strong enough to withstand the pulling force of the rope. Otherwise, the resulting stresses can cause breakage of the end effector. The angle at which the rope enters and leaves the end effector influences these stresses. If the angle is too sharp, the stresses in the end effector increase, which can cause it to break. Figure 20a shows the end effector designed by previous graduates of TU/e. Louer (2022) and Jansen (2021) 3D-printed the end effector of polyethylene and winded several two-dimensional elements with it. The bottom of the end effector was designed to connect a rubber, which should increase the radius of the curve and therefore lower the forces on the end effector. For this research, the end effector design was modified to be able to attach it to the new end effector connector. Afterwards, the end effector was 3D-printed of polyethylene and bolted to the new connector, as can be seen in Figure 20b. However, during test winding, the end effector broke multiple times at the same location (Figure 20c). The 3D-printed end effector appeared not strong enough to resist the pulling force of the rope.

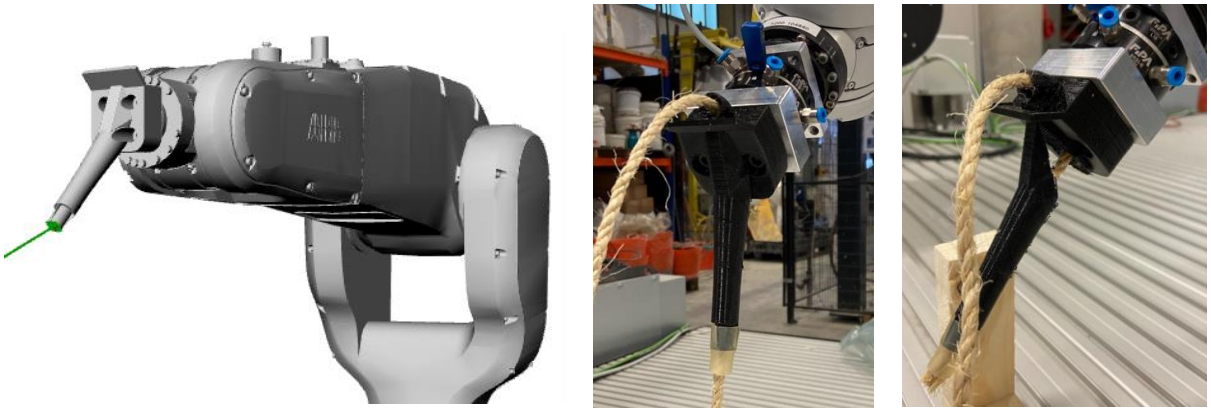

(a) *(b)* *(c)*

Figure 20 End effector designed by Louer (2022) and Jansen (2021)

A new end effector was made from available materials in the SED lab. Figure 21a shows the end effector, made of aluminium and steel elements. The previous end effector consisted of rubber and 3D-printed polyethylene, since these materials do not bond with epoxy resin. Aluminium and steel can however bond with epoxy resin, therefore, a rubber is placed in the steel tube which prevents the tube from being damaged by the resin. Furthermore, the rubber increases the radius of the curve. This decreases the stresses on the end effector, ensures smoother winding, and prevents the rope from shearing sharply along the steel tube. The latter could also cause the resin to be scraped off the rope, leading to degraded impregnation. The rubber can be replaced after each winding session if necessary.

At the end nodes of the non-structural formwork, the robot winds the rope around bolts. The height of the bolts should be smaller than the height from bottom end effector to the aluminium block in which the steel tube is clamped, to prevent collision between the bolts and the end effector. The tip of the end effector is calibrated, after which the end effector is drawn in Rhino and connected to the ABB IRB 1200-5/0.9 robot in Robot Components, as can be seen in Figure 21b and 21c.

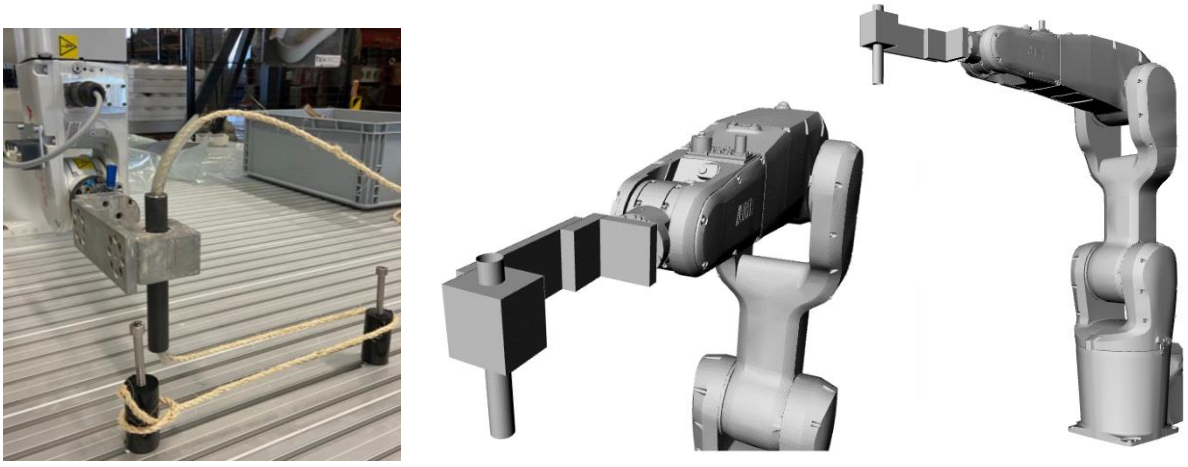

(a) *(b)* *(c)*

Figure 21 Final design end effector

4.3 Filament winding process

Before the sisal rope reaches the robot end effector, it needs to be unwound from the spool, impregnated with epoxy resin, and pre-tensioned. During this winding process, it is preferred to prevent all equipment and material of the SED lab from being damaged by the resin.

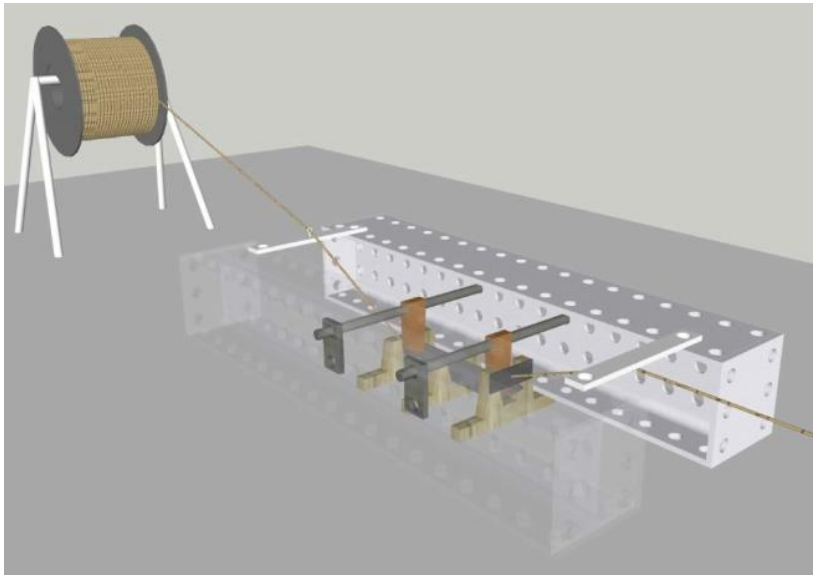

Figure 22 Filament winding process (Louer, 2022)

The filament winding process from spool to end effector is visualized in Figure 22. First, due to the rotating formwork, the sisal rope unwinds from the spool. From the spool on, the rope is guided through a steel

eye towards the resin bath. This bath is made of a disposable aluminium tray, provided with two panels. The panels feature a rubber semicircle at the bottom, which guides the rope through the bath. The submerging panels ensure the rope is fully impregnated. At the end of the resin bath, a disposable rubber is placed with a circular opening of Ø 4 mm. If the sisal rope passes through the narrow opening, the rope is tensioned and redundant resin is released. From test winding, it was observed that the rubber resulted in sufficient tension on the rope, without the use of nip rollers. The rubber can be replaced easily if the circular opening is enlarged after a winding session. Lastly, the tensioned and impregnated rope is guided to the end effector passing through another steel eye.

4.3.1 Resin impregnation

The SR InfuGreen 810 / SD 8824 is mixed in small batches, according to the prescribed mixing ratio by weight of 100 / 22 (Sicomin Epoxy Systems, 2017). The resin batches do not exceed 200 / 44 grams at a time, to prevent an exothermic reaction to occur during manufacturing, causing the resin to heat up and boil.

Louer (2022) conducted a soaking experiment to determine the required impregnation time for sisal rope. The experiment concluded that an impregnation time of one second is enough to fully impregnate sisal rope of Ø 4 mm. Furthermore, Appendix 1 Sicomin technical datasheet shows that the viscosity of Infugreen 810 / SD 8824 starts to increase after 44 minutes at an ambient temperature of 20 degrees Celsius (Sicomin Epoxy Systems, 2017). Therefore, it is preferred to wind the structure within 44 minutes. Figure 23 shows that the total filament winding process takes 30 minutes, when the robot winds with an average speed of 100 mm/s.

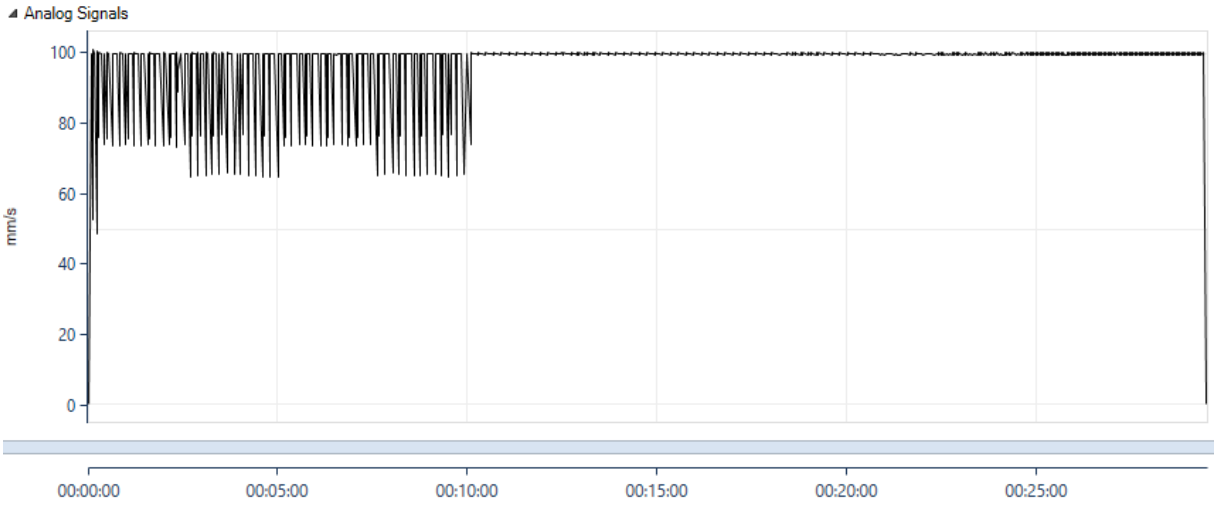

Figure 23 Duration to wind one column (Robot Studio)

The required length of the resin bath can be calculated according to Formula 1.

$$s = v \cdot t \qquad [1]$$

s = length resin bath (mm)
v = robot speed (mm/s)
t = minimum required impregnation time (s)

$$s = 100 \cdot 1 = 100\ mm$$

The aluminium disposable trays used for the resin bath ensure 200 mm of fiber impregnation and therefore a sufficient soaking time of two seconds.

4.4 Curing

After manufacturing, the resin should be cured at elevated temperatures to harden. Appendix 1 Sicomin technical datasheet compared three different curing cycles for the SR InfuGreen 810 / SD 8824 system. The mechanical properties were optimized for a post-curing cycle of eight hours at 40 degrees Celsius. Before post-curing the structure should be stored at a minimum ambient temperature of 20 degrees Celsius. The Sicomin technical datasheet does not prescribe the relative humidity for optimal curing.

5 Numerical optimization

The numerical model is divided into several parts. This chapter elaborates on the full numerical optimization process, addressing the plug-ins used. Furthermore, the final column design resulting from the optimization will be discussed.

5.1 Optimization goal

The numerical optimization aims to find an optimized lightweight structure to transfer an axial compressive force. As mentioned in Section 2.2 References, lightweight structures feature a strong relationship between shape and force. The goal is to minimize material to lower self-weight without losing strength, stiffness and stability. Therefore, the unidirectional properties of the sisal fibre should be optimized and the material must be placed according to the flow of forces. Consequently, the first two optimization criteria are minimizing mass and maximizing stiffness.

Two benchmarks for structural stiffness are displacement and internal elastic energy. Where the maximum displacement can strongly be influenced by local extremes, the internal elastic energy considers the structure as a whole. The internal elastic energy is the energy stored as a result of force application. Figure 24 explains that the structure has a certain displacement Δx, due to the application of force F. The displacement depends on the stiffness of the structure, represented by factor k. If the force F remains equal, and the stiffness of the structure increases, the displacement will decrease. The internal energy U can be calculated as the area under the force-extension curve. The smaller this area, the more efficient the structure. Therefore, to maximize stiffness, the internal elastic energy should be minimized.

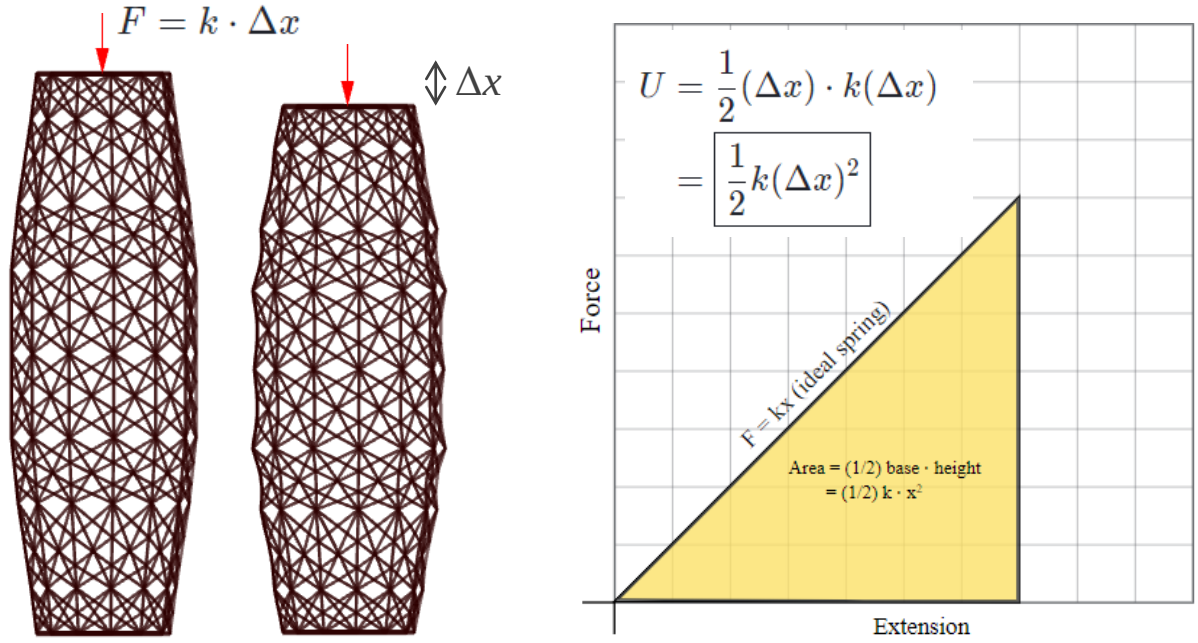

Figure 24 Internal elastic energy (Khan Academy, n.d.)

Section 2.3 Literature study discussed the governing failure mechanism for slender structures loaded in axial compression, namely buckling. Since this research aims to optimize for axial compression, the third optimization criterion is to maximize the resistance of the column against buckling. This is done by maximizing the Buckling load factor (BLFacs), resulting from the Karamba3D structural analysis. This non-negative factor indicates the factor by which the applied force can be multiplied before buckling occurs.

In total, there are three optimization goals: minimize mass and internal elastic energy, and maximize resistance against buckling. Therefore, the Multi-Objective Evolutionary Optimization plug-in Octopus is used. Octopus allows solving for multiple optimization objectives at once, resulting in a range of optimized trade-off solutions between the extremes of each goal (*Octopus*, 2023).

5.2 Process model

Figure 25 represents the process model of the numerical optimization performed in Rhinoceros through a script written in the visual programming plug-in Grasshopper. First, basic Grasshopper components, several plug-ins, and Python programming are used to generate the geometry, which can be influenced by the six parameters discussed in Section 2.4 Parameters.

After defining the basic geometry, a structural analysis is done through the Karamba3D plug-in. Karamba3D is an iterative, parametric structural engineering tool that allows for accurate and quick Finite Element Analysis (FEA) (Karamba3D, n.d.). Afterwards, the Koala plug-in is used to create an XML-file that can be imported into SCIA Engineer, to verify the structural analysis of Karamba3D.

The results of the first Karamba3D structural analysis are used for the geometrical optimization in Octopus. While changing the geometrical parameters, Octopus searches for an optimized structure that is minimized in mass and internal elastic energy, and maximized in resistance against buckling.

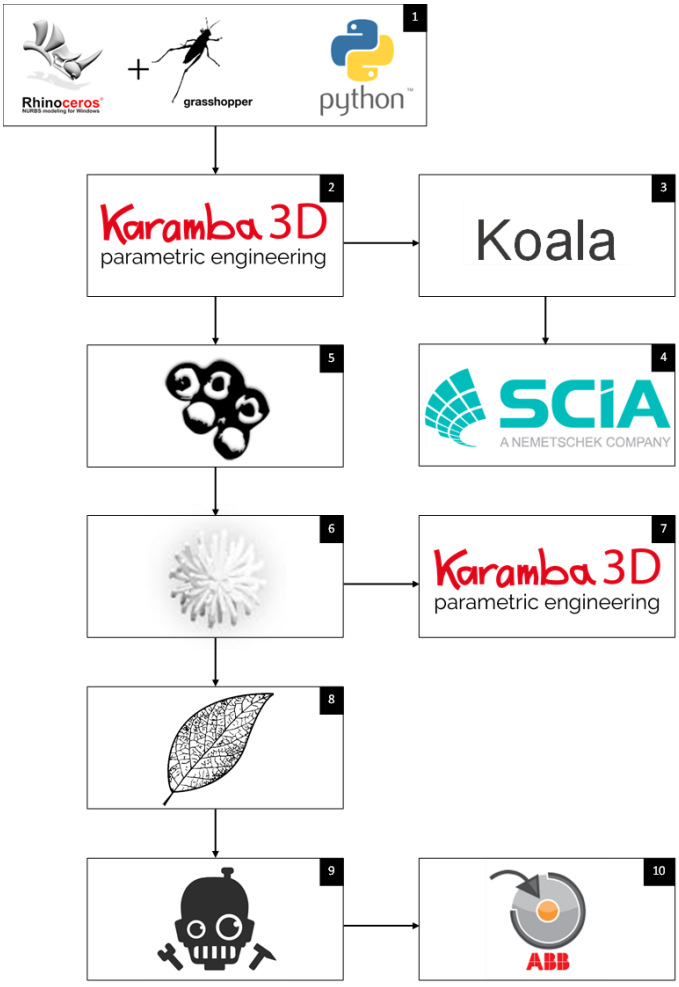

Figure 25 Process model numerical optimization

After the geometrical optimization, a sizing optimization is performed based on the strain energy. For this, an iterative loop is created using the Anemone plug-in. This optimization results in a final design, of which a final structural analysis is performed in Karamba3D.

When the final geometry is known, the winding path is determined. The Leafvein plug-in is used to define this Eulerian path. The resulting point sequence can be used as input for the Robot Components plug-in. The RAPID-code created by this plug-in can finally be loaded into Robot Studio, to simulate the robotic winding path and to manufacture the structure.

5.3 Structural analysis

The structural analysis is conducted using the parametric, structural engineering tool Karamba3D. An important property of the plug-in is that it divides lines into segments at intersection points. To manage the data correctly, this is done manually before the Karamba3D part of the script. As a result, Karamaba3D does not create new line segments, and the data is managed in such a way that it is clear which line segments form one line. This is done by making use of the data tree management in Grasshopper. Each branch of the tree represents one line, which is subdivided into several segments. The line segments provide the Karamba3D input.

Firstly, the 'LineToBeam' component is used to transform all line segments into beam elements with a certain cross-section (Figure 26). To define a cross-section, the 'Material Properties' component is used to manually create a material, that is unknown in the Karamba3D material library. For this, the material properties discussed in Section 3.3 Mechanical properties are used.

Secondly, the boundary conditions are defined. The winded column should be simply supported. Therefore, at the top and bottom stiff elements are implemented in the model, as can be seen in Figure 28. These elements represent the end node of the column, which should be able to be bolted to a spaceframe connection. The 'Beam-Joint' component is used to define the connection between the stiff elements and the winded column. This component ensures that rotation is allowed, and translation is restricted. Additionally, supports are added to the centroid of the stiff elements, visualized by the green triangles in Figure 28. The bottom hinge allows rotation, and prevents translation in X-, Y-, and Z-direction. The top support also prevents translation in X- and Y-direction. However, it allows the structure to translate in the Z-direction. Furthermore, at the top, rotation in the Z-direction is restricted, to prevent torsional movements. After adding the supports and joints to the model, the column is axially loaded with a point load of 1 kN (Figure 29). The stiff elements transfer this force to the winded column. Figure 28 shows a structure where the supports, stiff elements and applied point load are visualized.

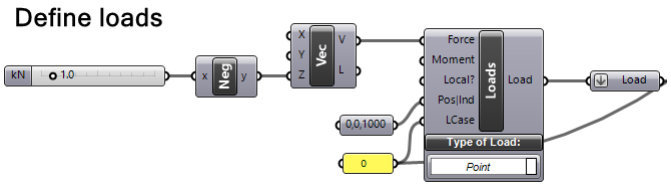

Figure 29 Defined loads (Karamba3D)

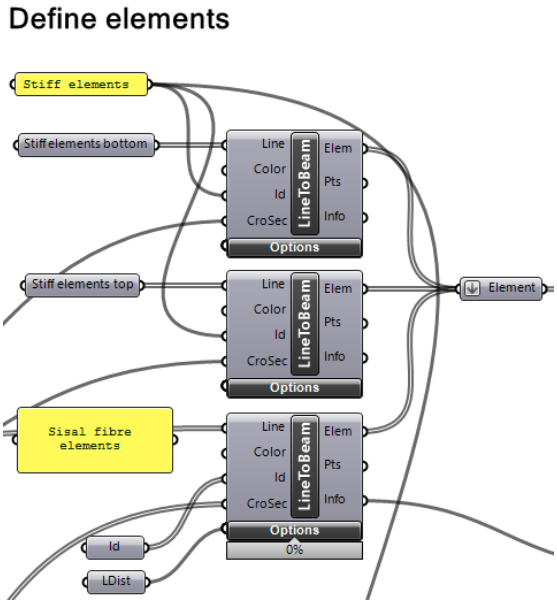

Figure 26 LineToBeam component (Karamba3D)

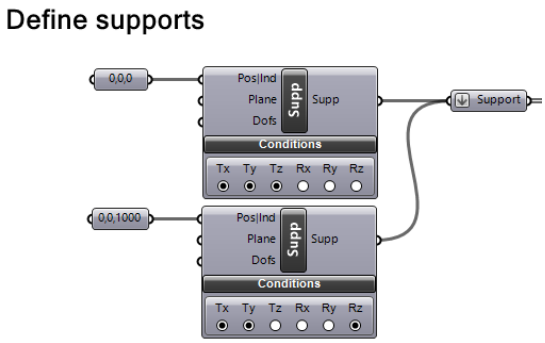

Figure 27 Defined supports (Karamba3D)

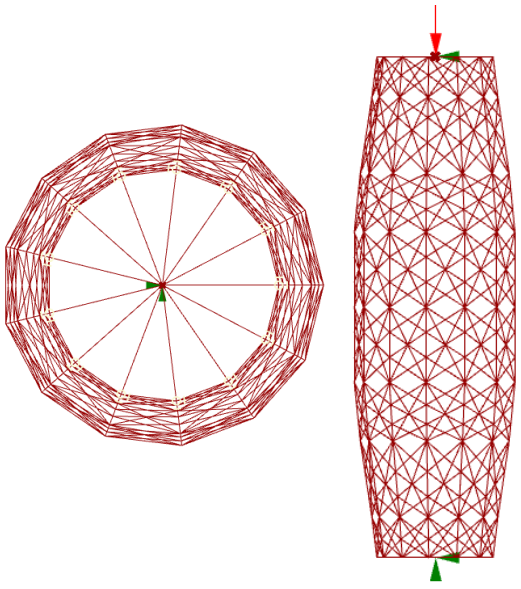

Figure 28 Visualization of the supports, stiff elements, and point load on the structure

The defined elements, supports, loads and joints provide the input for the ‘Assemble’ component, which creates a structural model of the gathered data (Figure 30). After this, the ‘Analyze’ component is used for first-order structural analysis to determine the internal elastic energy. The ‘AnalyzeThII’ component is used to conduct a second-order buckling analysis. During this second-order analysis, the deformations of the structure as a result of force application are taken into account. The results of both components can be visualized using the ‘ModelView’ and ‘BeamView’ components. The output of the structural analysis provides, among other results, the mass, maximum displacement, stresses, buckling load factor, buckling modes, and internal elastic energy. These values are used for the numerical optimization.

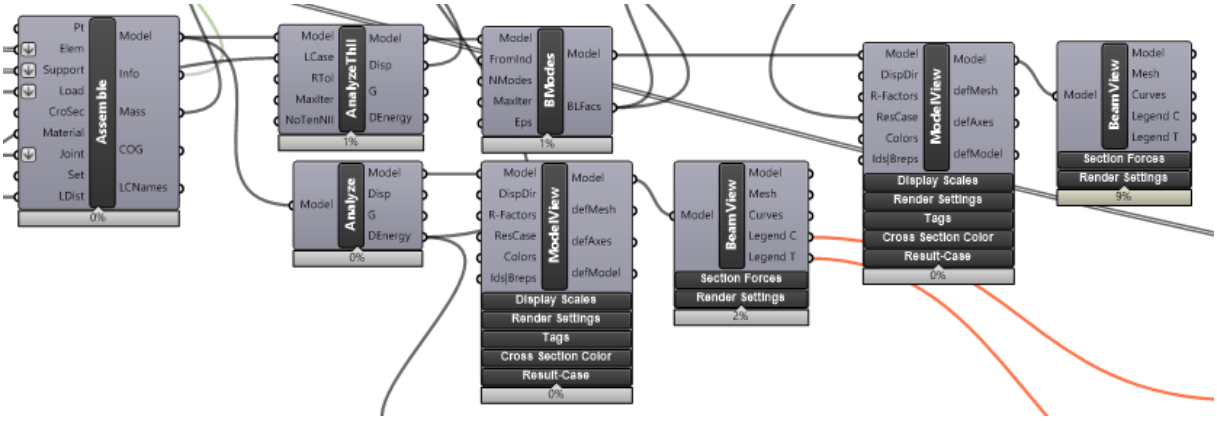

Figure 30 Overview Karamba3D structural analysis in Grasshopper script

5.4 Geometrical optimization

The geometrical optimization is performed using the Octopus plug-in. Figure 31 shows the ‘Octopus’ component used, which requires two inputs. The first input are the Genomes (G), which are the parameters discussed in Section 2.4 Parameters. These parameters are number sliders with minimum and maximum values. The second input, Octopus (O), requires the fitness function values to be optimized. Namely, the Karamba3D resulting values for the mass, internal elastic energy and buckling load factor. Octopus searches for the minimum in its default settings, therefore, the buckling load factor is multiplied by minus one.

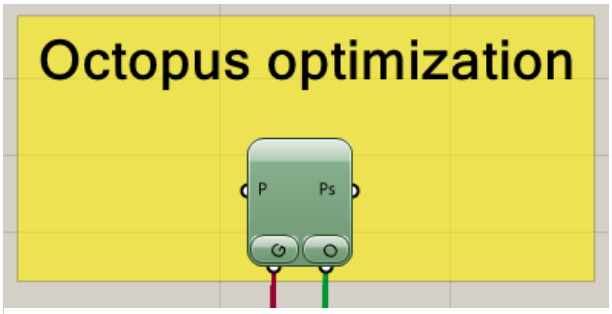

Figure 31 Octopus component for geometrical optimization

Figure 32 shows the result of the Octopus optimization. In this three-dimensional graph, the red horizontal axis represents the internal elastic energy in Kilonewton meter, multiplied by a hundred thousand. The green horizontal axis is the total mass of the structure in kilograms. The vertical axis represents the buckling load factor. Each cube represents a solution, resulting in a range of optimized trade-off solutions. Since all three fitness function values are of equal importance, the solution closest to the origin of the three-dimensional graph represents the most optimal design, which is minimized in mass and internal elastic energy, and maximized in resistance against buckling.

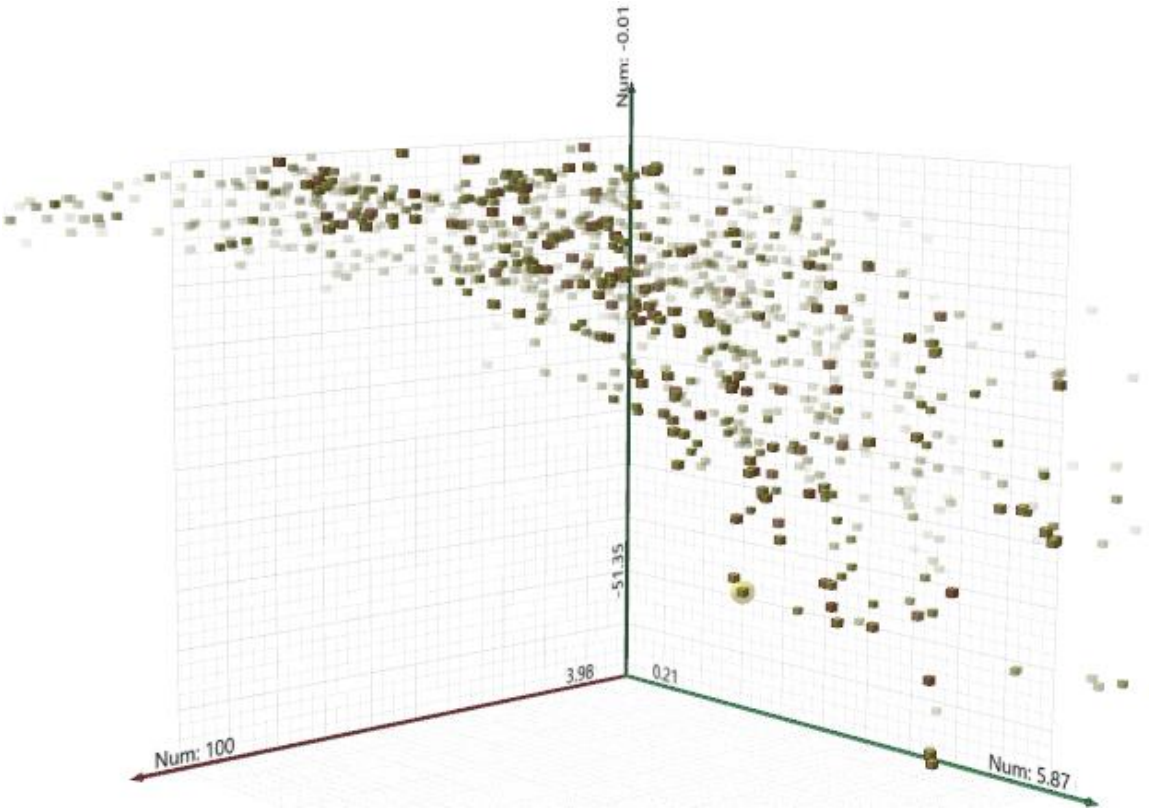

Figure 32 Solutions Octopus optimization

5.4.1 Final geometrical design

The Octopus optimization resulted in a single solution that was closest to the origin, this solution is highlighted in yellow in Figure 32. The geometry of this final design can be seen in Figure 33. Table 4 provides the parameter input for the final design.

Table 4 Parameter input final design

Auxiliary ring	Z-height [mm]	Radius [mm]	Diameter [mm]
1st/Base ring	0	117	234
2nd ring	81	127	254
3rd ring	233	150	300
4th ring	350	162	324
5th/Middle ring	500	162	324
6th ring	650	162	324
7th ring	767	150	300
8th ring	919	127	284
9th/Top ring	1000	117	234

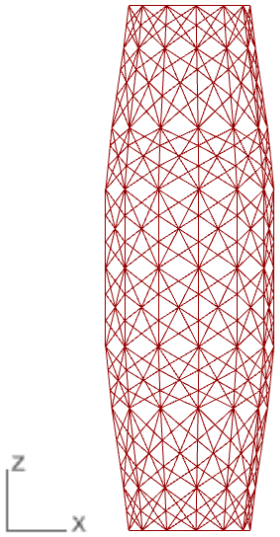

Figure 33 Design resulting from Octopus optimization (Rhinoceros) →

A slightly convex-shaped column can be observed of which the diameter increases 90 mm from base ring to midspan. The amount of nodes on each ring is set to 13, which implies there are 13 vertical lines in the model. Furthermore, the design characterizes two types of diagonals, both shifting a fixed amount of nodes between two rings over the whole column length. For the bigger diagonals, this value is set to one. For the smaller diagonals, it is set to three.

When a straight line is drawn between ring one and three, it intersects with the second ring. As a result, the second ring does not add convexity to the model and therefore does not affect the shape. For the formwork design, this implies that the second and eighth ring are not required to create the convex-shaped column.

5.4.2 Verification structural analysis

For this research, the results of the Karamba3D structural analysis are verified in SCIA Engineer. This is done since the results of Karamba3D will be compared to test results in a later stage. The Koala plug-in is used to export the structural model from Grasshopper to SCIA Engineer, by creating an XML-file. The file is imported into SCIA and the model is calculated. The results of the structural analyses are provided by Table 5. Furthermore, Figure 34 compares the first buckling modes. For the structural analyses, it is assumed that each line represents two sisal ropes.

Table 5 Verification of Karamba 3D structural analysis in SCIA Engineer

	Mass [kg]	**BLFacs [-]**	**Max displace-ment [cm]**	**Max compressive stress [MPa]**	**Max tensile stress [MPa]**
Karamba3D	2.79	35.05	0.045	3.94	1.80
SCIA Engineer	2.79	34.01	0.045	4.00	1.80

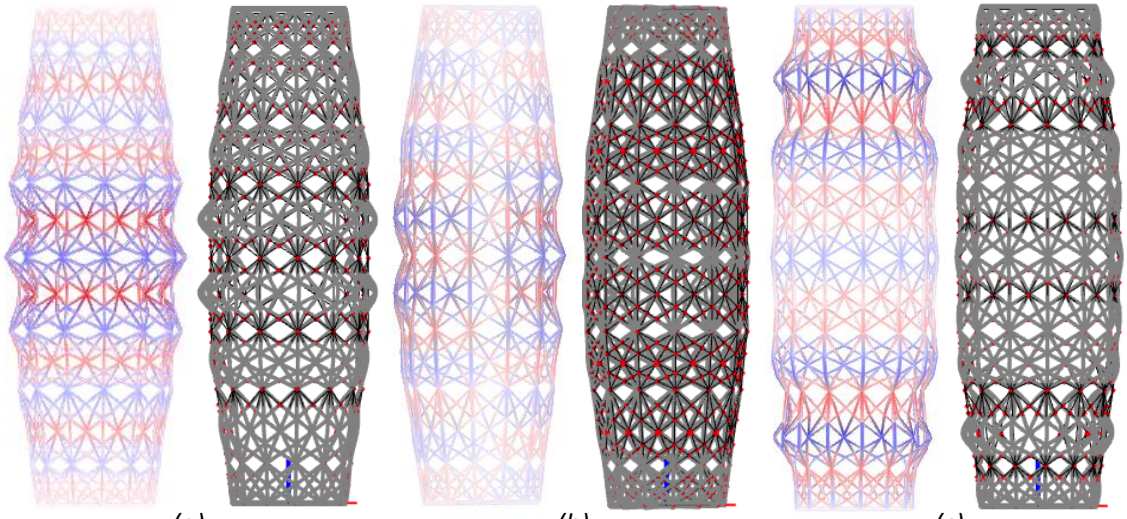

Figure 34 First buckling modes Karamba3D (left) and SCIA Engineer (right)

From Table 5 it can be observed that the resulting values for the mass, maximum displacement and maximum tensile stress correspond exactly. There is however a small difference in de buckling load factor and the maximum compressive stress. From Figure 34a, it can be seen that the first buckling mode for both analyses results in local buckling of the sisal rope around the perimeter, where the column has a radius of 162 mm. The only difference between Karamba3D and SCIA Engineer is that the rope buckles in opposite direction. In reality, the winding sequence influences the direction in which the rope buckles. Since diagonal lines are winded around vertical lines, vertical ropes are more likely to buckle inwards than outwards. For the other two buckling modes, visualized in Figure 34b and 34c, the results correspond exactly. For all buckling modes, local buckling of the sisal rope occurs before global bucking of the column occurs. The differences between the structural analyses are negligibly small. Therefore, it can be concluded that SCIA Engineer verifies the Karamba3D structural analysis.

5.5 Sizing optimization

After the optimized geometrical design is found, a sizing optimization is conducted to optimize the number of ropes for each line. This is an iterative process, where the mass is redistributed based on the strain energy. Figure 35 visualizes the process model of the iterative sizing optimization.

The iterative loop is created using the Anemone plug-in. Before starting the loop, all data should be managed correctly. Namely, Karamba3D results volumes, cross-sectional area's and maximum stresses for line segments, as mentioned in Section 5.3 Structural analysis. Making use of the Grasshopper data tree management, it is known which line segments form one line. This is important since all segments forming one line should feature the same cross-section. Consequently, the volume per line V_i, cross-sectional area per line A_i, and maximum stress per line σ_i are known. These values provide the input for the iterative loop.

The first Anemone component used to create the loop is the 'Loop Start' component. Figure 36 visualizes the input for this component, where parameter N defines the number of iterations, D0 defines the data to loop, and T the trigger which should be activated by clicking on the button to restart the loop.

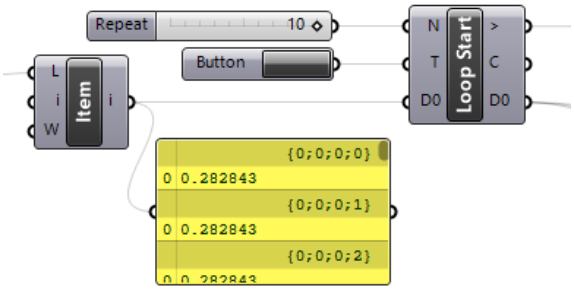

Figure 36 Start of iterative loop (Grasshopper)

For this loop, D0 is the equivalent radius in centimeters. Figure 37 shows how this radius is calculated, based on the number of ropes. As discussed in Section 3.3 Mechanical properties, a maximum value should be set to this number of ropes. This maximum is set to 8 ropes per line. The minimum is set to 0.2 ropes per line. If lines require a cross-section corresponding to 0.2 ropes, they could be removed after the iterative loop.

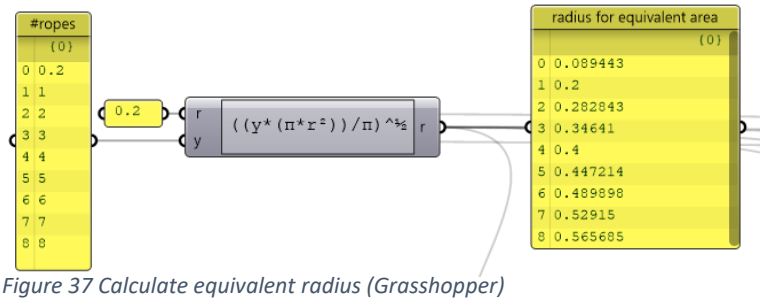

Figure 37 Calculate equivalent radius (Grasshopper)

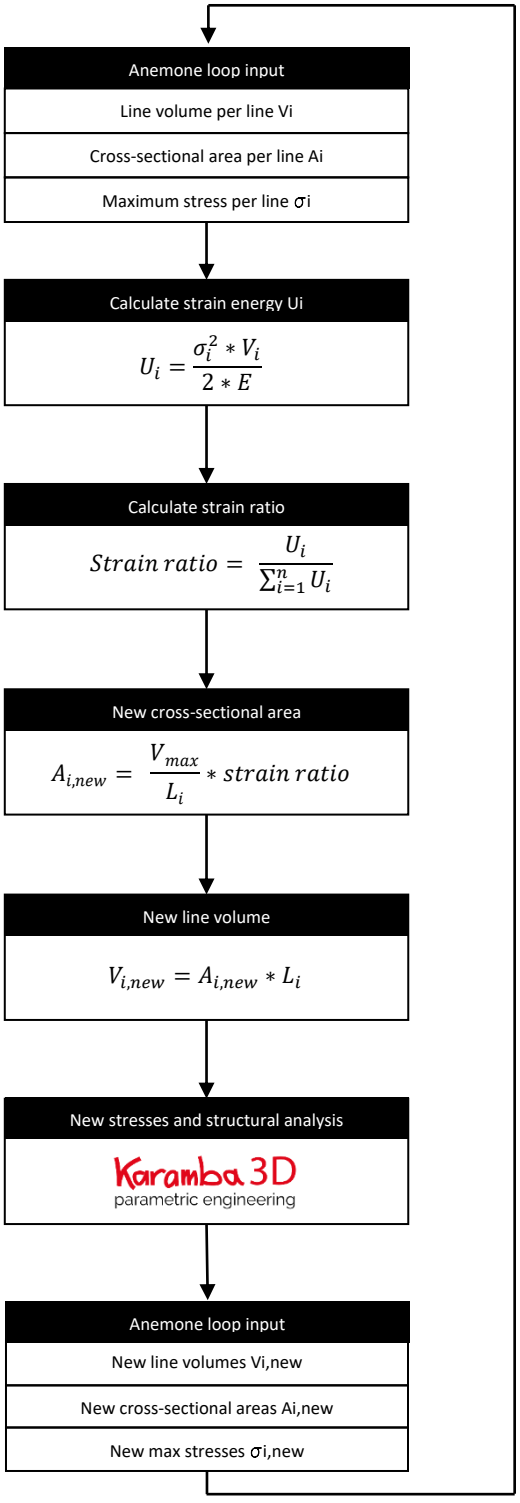

Figure 35 Process model iterative sizing optimization

For the first Karamba3D analysis, it was assumed that each line represented two sisal ropes. Therefore, the loop input D0 is an equivalent radius corresponding to two ropes for all lines. After the 'Loop Start' component, this equivalent radius is used to calculate the cross-sectional area A_i and the volume V_i per line. The latter is calculated using the line lengths, which are fixed values during the iterative process. The maximum stress per line results from the Karamba3D analysis, which is part of the loop. The strain energy U is calculated for each line, according to Formula 2.

$$U_i = \frac{\sigma_i^2 * V_i}{2 * E} \quad [2]$$

Secondly, the strain ratio is calculated by dividing the strain energy per line U_i by the total strain energy. This strain ratio is used to calculate the new cross-sectional area per line $A_{i,new}$. To prevent the iterative loop from taking too big steps per iteration, the constraint is set that the new cross-sectional area $A_{i,new}$ may not differ more dan 10% compared to the previous cross-sectional area A_i. Based on the new cross-sectional areas, the new line volumes are calculated and Karamba3D is used to structurally analyze and calculate the new model. This calculation results in new maximum stress values per line $\sigma_{i,new}$. After this, one iteration is completed and the loop can run again. Table 6 and Figure 38 show the result of the sizing optimization after 10 iterations. The number of ropes increased for highly stressed lines and decreased for less stressed lines. In the optimized design, the vertical lines are winded four times, the bigger diagonals two times, and the small diagonals one time. This results in an increased buckling resistance and decreased values for the maximum stresses, displacement, internal energy and mass. Furthermore, it can be seen that the structural analysis of the final design (Figure 38c) refers back to the conducted FEM-analysis (Figure 38e). Consequently, the final optimized design is based on the flow of forces.

Table 6 Structural analysis before and after sizing optimization

	Mass [kg]	Elastic energy change [kNm]	BLFacs	Max displace-ment [cm]	Max comp. stress [MPa]	Max tensile stress [MPa]
Before sizing optimization	2.79	2.23 x 10^-4	35.05	0.045	3.94	1.80
After sizing optimization	2.46	1.52 x 10^-4	39.10	0.030	2.91	1.58
Difference	-11.83%	-31.84%	+11.55%	-33.33%	-26.14%	-12.22%

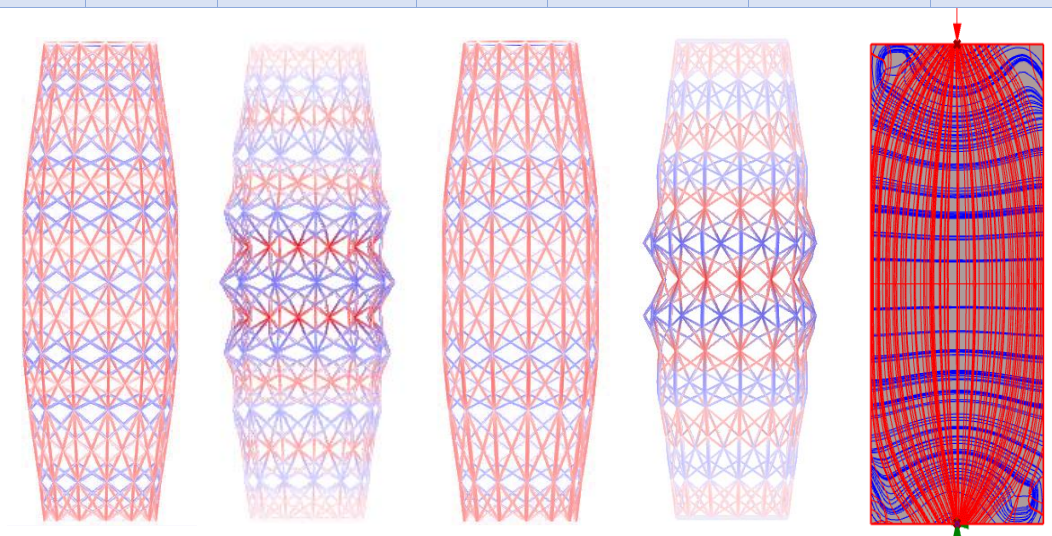

(a) *(b)* *(c)* *(d)* *(e)*

Figure 38 Structural analysis final design (a) before and (c) after sizing optimization, with corresponding buckling modes (b) before and (d) after sizing optimization. (e) Principle stress analysis

5.6 Eulerian winding path

After the numerical optimization, the final optimized column design is known. To manufacture the structure by filament winding, an Eulerian path should be defined to be able to wind the column in one continuous session. To define the winding path, it should be taken into account that the vertical lines should be winded before the diagonals, as discussed in Section 2.4 Parameters. If the diagonals would be winded first, there are limited contact points between the verticals and diagonals, which decreases the strength of the column. By winding the diagonals around the verticals, the amount of contact points increases and the fibre span reduces, which increases the buckling resistance of the column (J. Christie et al., 2021).

The Leafvein plug-in is used to define an Eulerian path for different layers to control the winding sequence. Figure 39 shows a part of the script where the winding path is determined for the first layer. The input for the 'Custom Graph' component is a set of small line segments. The component creates a graph, and uses the start and end points of the line segments to define graph nodes. The output of the component provides the input for the 'Node to Point' and 'Eulerian Cycle' components. The 'Eulerian Cycle' component results in a list of graph nodes that defines the Eulerian path. The output of the 'Node to Point' component can be used to translate the list of graph nodes to the corresponding points.

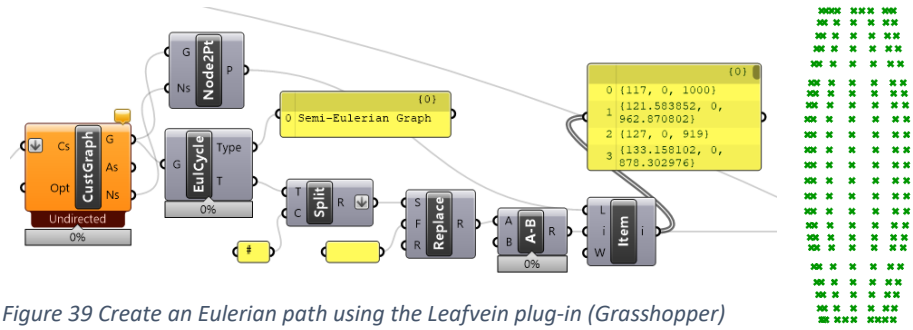

Figure 39 Create an Eulerian path using the Leafvein plug-in (Grasshopper)

This method is used to define an Eulerian path for the vertical lines and different diagonals. Figure 40 shows the winding sequence, where a polyline is drawn through the set of points to visualize the path. Figure 40a and 40b visualize the first two layers. Logically, the second layer starts where the first layer ends. The sizing optimization showed that the vertical lines had to be woven four times. Therefore, the first two layers have to be winded twice. After the verticals, the bigger diagonals will be winded twice, visualized in Figure 40c. Lastly, the small diagonals will be winded, resulting in the final design (Figure 40d). The result is a list of points, defining a winding path with a single start and end point.

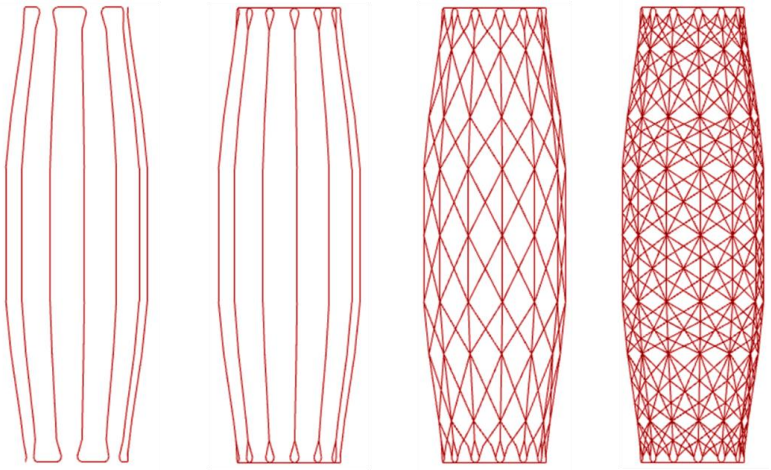

Figure 40 Eulerian path for robotic winding, visualized from left to right

5.7 Robot Components

The point list, resulting from the determined winding path, provides the input for the Robot Components script. First, all points are moved 15 mm outwards to prevent collision between end effector and formwork. The rubber end of the end effector bridges this distance and ensures smooth winding, as discussed in Section 4.2 End effector. After each layer of winding, the robot moves 4 mm outwards as well, to prevent collision with the previously winded ropes. After moving the points outwards, a start and end point is added to the list of points 10 centimeters above the first point. This is done to prevent collision between the robot and the formwork when the robot moves to its first target point (Figure 41a).

All target points should be placed on the moveable work object. Therefore, the plane orientation of the moveable work object should correspond to the plane orientation of the target points. Furthermore, the plane orientation and external axis value of each point influences how the robot approaches a point. It is preferable that the robot only moves in lateral direction, from left to right, without having to move around the structure. Therefore, the planes of the target points should be aligned pointing outwards, as visualized in Figure 41b. If the rotation table and robot are in their initial position, the plane orientations correspond. Furthermore, these plane orientations correspond to the plane orientations of the target points lying at the top of the horizontally placed formwork. Consequently, the rotation table rotates the formwork so that the plane orientation of the end effector corresponds to that of the target point. This results in the robot only winding at the top, moving in lateral direction only. Figure 41a visualizes the robot path, and the corresponding plane orientations of the end effector, rotation table, and first target point.

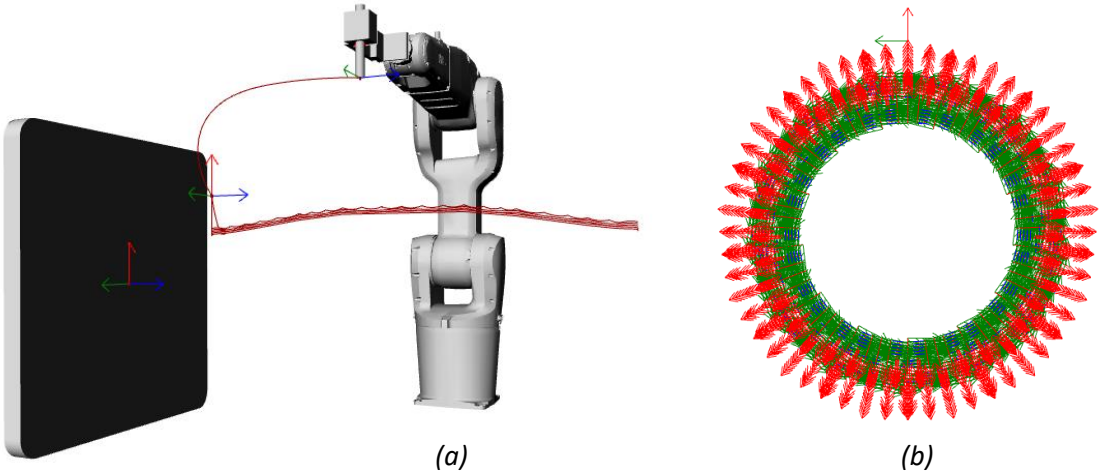

Figure 41 (a) Robot path and plane orientation end effector, rotation table and first target point (b) Aligned plane orientations of target points (Rhinoceros)

After all plane orientations are defined correctly, the 'Robot Target' component combines all data and creates a list of robot targets. This list, together with the defined moveable work object, is used to create movements. Figure 42 shows how the move instructions are created using the 'Move' component. As discussed in Subsection 4.3.1 Resin impregnation, a continuous speed of 100 mm/s is used for all movements. Furthermore, the robot moves with a joint movement to the first target point. After this, only linear movements are used, to prevent the robot from

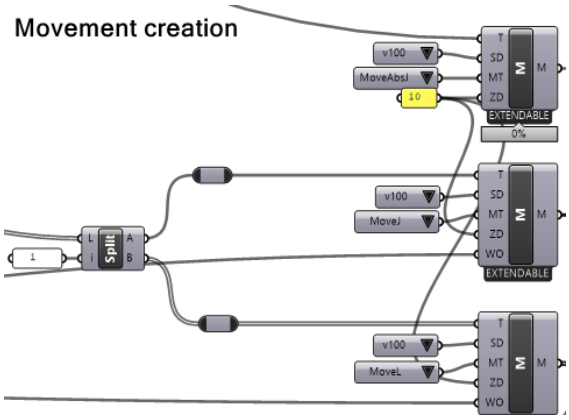

Figure 42 Robot movement creation (Grasshopper)

wrapping the rope around the robot arm, to continuously control the robot's motion, and to guarantee accuracy. For all targets, the zone data (ZD) is set to 10 mm. This value indicates the precision of the determination of the targets for the robot. The value of 10 means that the robot translates the input target to a robot position with an accuracy of 10 mm. The robot will therefore in reality not be more than 10 mm away from the target as it was defined in digital 3d space.

The created movements are combined in a list of actions. This list provides, together with the defined robot and external work object, the input for the 'Path Generator' and 'RAPID Generator' components (Figure 43). By clicking on the button, the data transfer to both components is updated. Consequently, the 'Path Generator' allows to compute the robot path and simulate its execution. The 'RAPID Generator' generates a RAPID Program Module (PM) and a RAPID System Module (SM). The PM script, also known as the MainModule, defines robot movements. The SM script, or BASE-code, defines the robot head orientation based on the applied end effector. Figure 43 visualizes the generated structure after completing the winding path. Appendix 3 Overview Grasshopper scripts elaborates on the full Robot Components script.

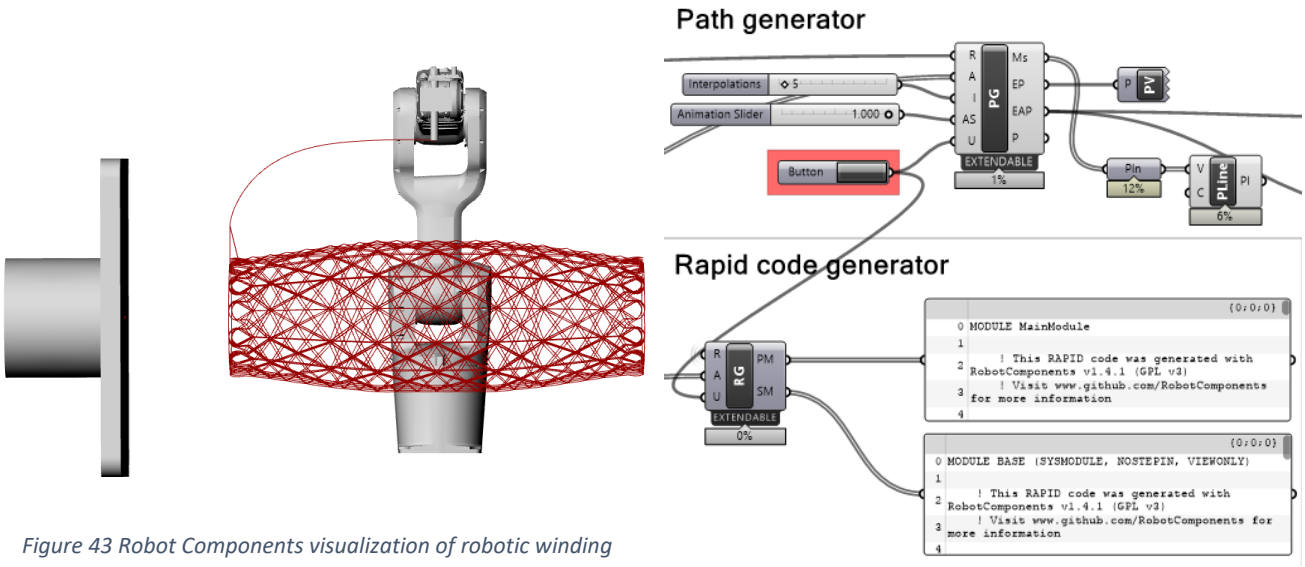

Figure 43 Robot Components visualization of robotic winding

5.8 Robot Studio

The created RAPID Program Module and System Module are loaded into Robot Studio, to simulate the complete winding path. At first, the simulation engine Robot Studio presented an error that some targets were out of reach. This problem was solved by correctly defining the external axis value for each target point, and aligning all planes as discussed in Section 5.7 Robot Components. The scripts were run again till the program ran the complete path without errors. After this, the RAPID-code scripts could be used for manufacturing. Figure 44 visualizes the final simulated robot path.

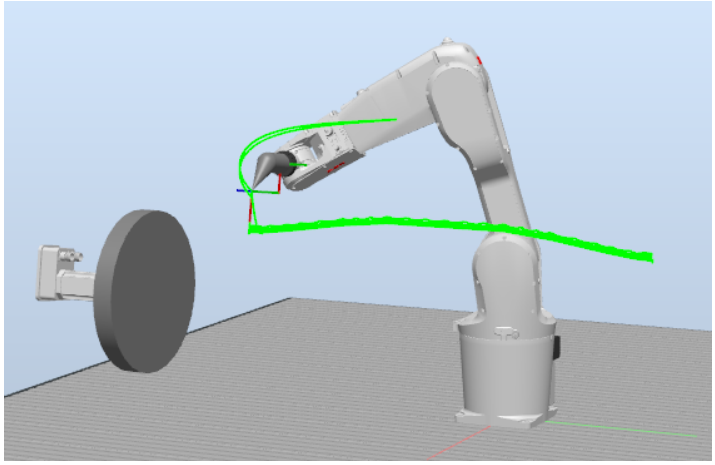

Figure 44 Simulation Robot path (Robot Studio)

6 Manufacturing

The column will be manufactured through robotic filament winding. This chapter elaborates on the full manufacturing process of the numerically optimized column, addressing the formwork design, winding process, curing cycle and end node design.

6.1 Formwork design

Since the numerical optimization resulted in a slightly convex-shaped column, a non-structural formwork had to be designed to wind the impregnated sisal rope around. The first criterion for this formwork design is that it must be able to be removed after the structure is fully cured. Secondly, the column ends feature a smaller diameter than the rest of the column. Therefore, an expanding mechanism was designed which fits through the column ends when not expanded. These expanding elements will be placed at the location of the third to seventh auxiliary ring, as discussed in Subsection 5.4.1 Final geometrical design. The mechanism consists of six elements, detailed in Figure 45.

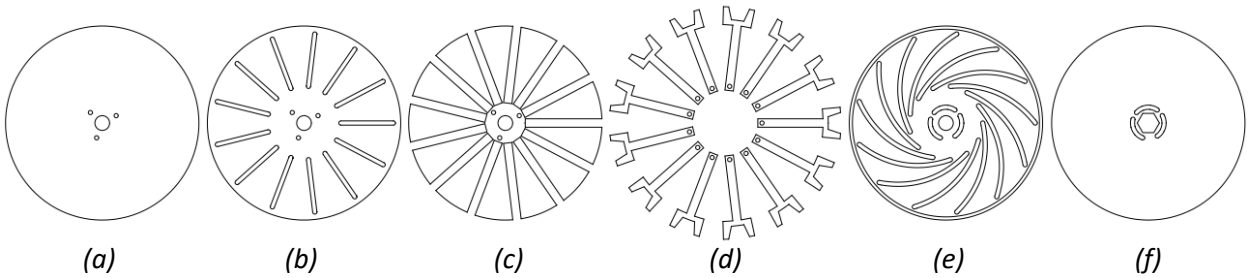

Figure 45 Elements expanding mechanism

The base circle of the expanding mechanism has a radius of 92 mm. First, elements a to c are glued together. This part of the mechanism will be fixed while rotating the mechanism. Secondly, the forks visualized in Figure 45d are placed in the slots of element c. During manufacturing, the rope will be placed in these fork elements where the fibres are pushed against each other to create bonding. The contact area between fibres must be maximized to maximize the bonding strength. Furthermore, the elements ensure the rope stays in place. Thirdly, element e is placed on top, and small pins are placed in the circular holes at the end of the fork elements. These pins ensure that the fork elements can move in and out by moving the pins along the slots of elements b and e. Lastly, element f is glued to element e, to prevent the pins from falling out. By rotating top elements e and f counter clockwise, the fork elements move outwards. Rotating again, clockwise, the elements move inwards. Figure 46 visualizes a 3D-view of the expanding formwork.

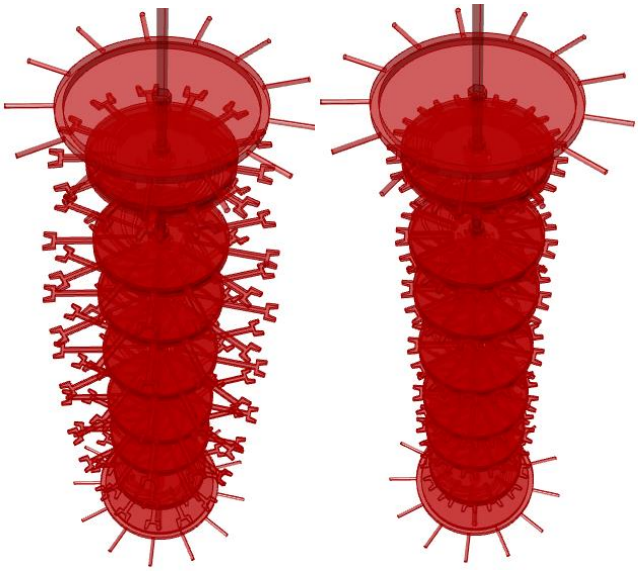

Figure 46 3D-view of expanding formwork

All elements are manufactured of MDF board. Figure 47a shows the mechanism where elements a to e are assembled. Figure 47b shows the expanded elements after rotating the top element counter clockwise. The elements are placed at correct position on a threaded rod, using nuts (Figure 47c and 47d). The three small threaded rods should make sure the bottom part of the mechanism remains fixed when the top part rotates. As can be seen in Figures 45f and 47c, the nut slightly falls into this top part. By placing two nuts, tightened against each other, the top part of all elements will rotate while rotating the threaded rod.

For the formwork ends, aluminium end nodes were designed for manufacturing. These elements, consisting of a ring and base plate, are visualized in Figure 52 in Section 6.2 Robotic filament winding. The aluminium ring features 13 M6 bolts, to wind the sisal rope around. The base plate can be placed in the ring, and can be used to connect the ring to the threaded rod by clamping it within two nuts. The two aluminium elements are connected by six M6 bolts. After curing, these bolts can be removed to remove the formwork through the aluminium ring at the column end. The aluminium end nodes and expanded elements are placed on a threaded rod, which is connected to the rotation table.

Figure 48 shows the manufacturing process, using the expanding formwork. During this test phase, the sisal rope is not impregnated with resin. In Figure 48a the convex shape of the column can be recognized. However, the convexity seemed to reduce during manufacturing, resulting in a straight column (Figure 48b). Since filament winding is a tension-driven process, the sisal rope is winded tightly around the formwork. This resulted in a compressive force on the fork elements, causing the formwork to rotate inwards.

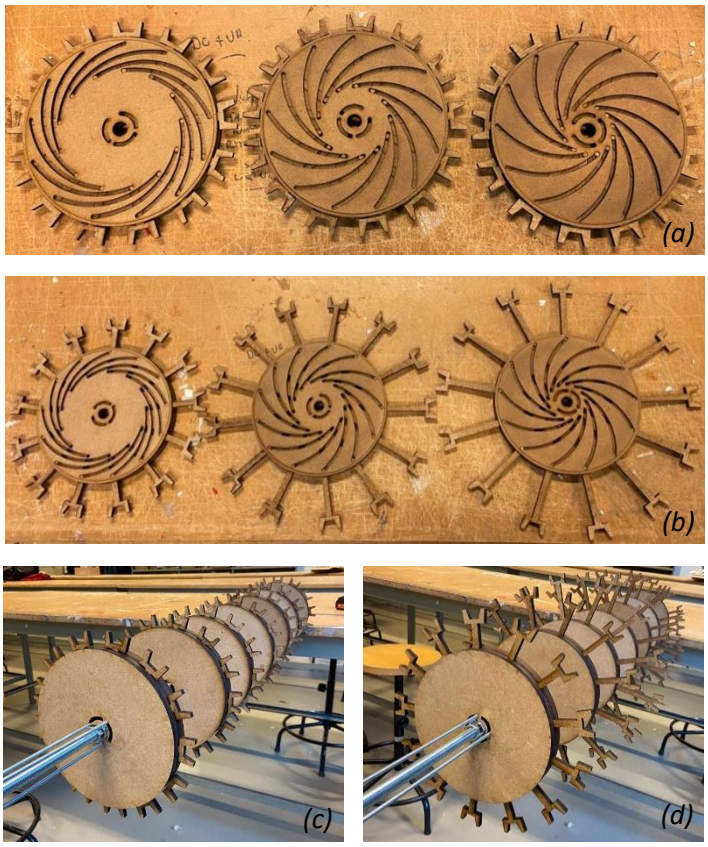

Figure 47 Expanding mechanism

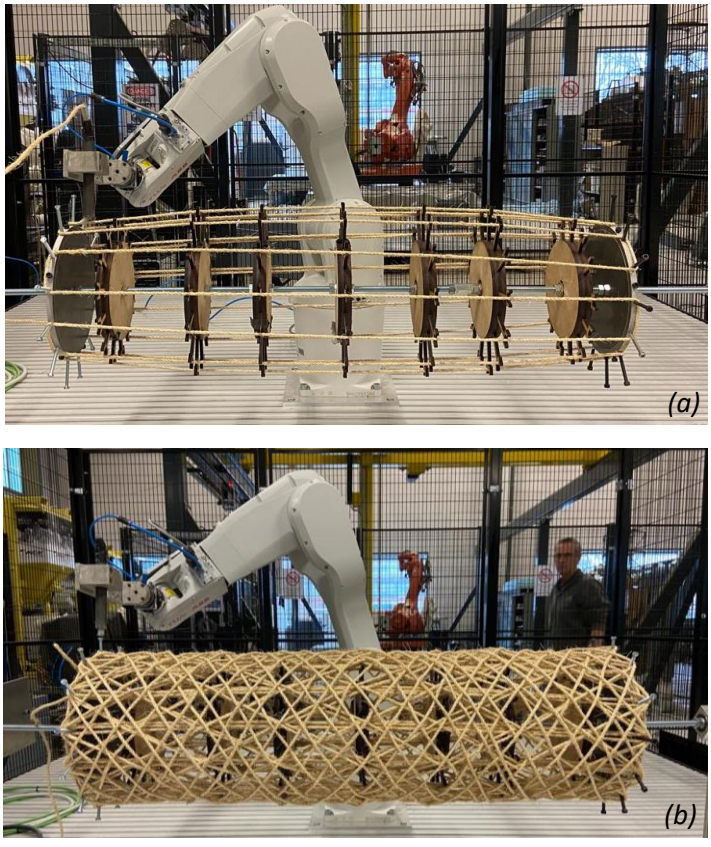

Figure 48 Test manufacturing with expanding formwork

Consequently, a new formwork had to be designed, which is visualized in Figure 49. The base circle still has a radius of 92 mm. The principle of the fork elements remained unchanged as well. However, the formwork does not move anymore. The fork elements are bolted to the base plate by small M4 bolts. After the structure is cured, the fork elements will be broken off and the base plates and bolts can be reused to manufacture a new structure. Section 6.3 Curing elaborates on the removal of the internal formwork.

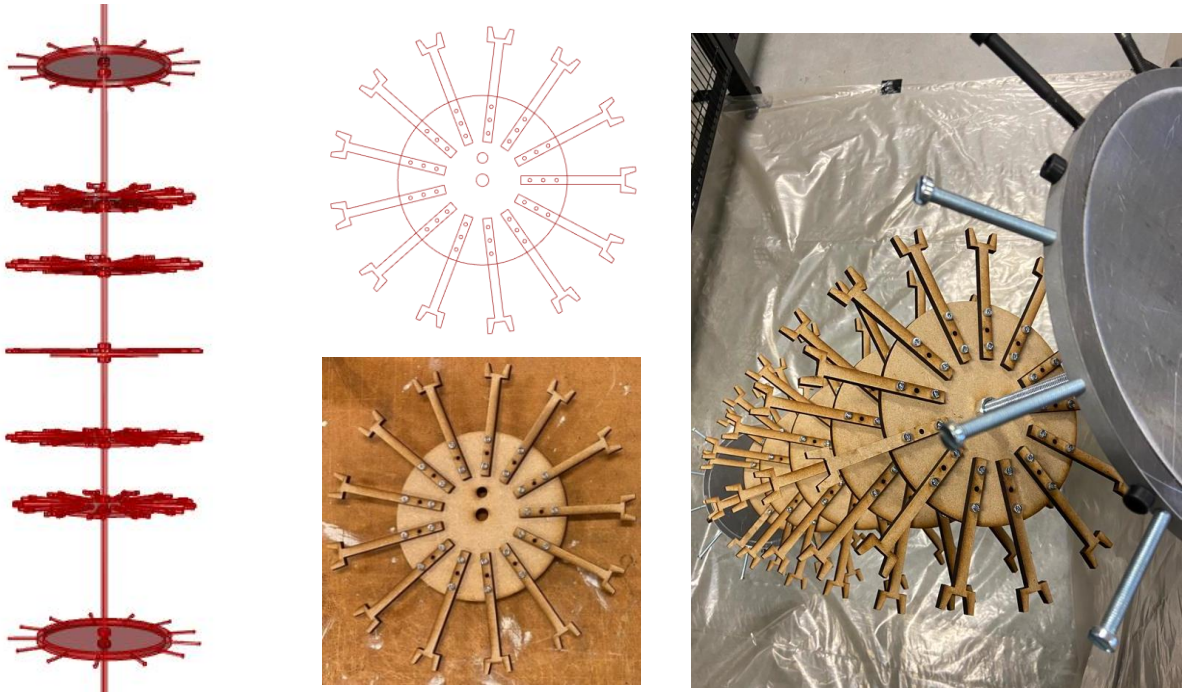

Figure 49 Final formwork design

The final formwork design is placed on the robot bed. Figure 50a shows the connection of the threaded rod to the rotation table. At the left, an aluminium plate is bolted to the moveable work object. This plate features a circular opening of Ø 12 mm in the centre. The threaded rod is placed in this opening and tightened by two nuts. Figure 50b visualizes the connection at the other end, which allows the threaded rod to rotate freely while the position is fixed.

A final test manufacturing is performed, using unimpregnated sisal rope. The optimized column was fully manufactured without errors (Figure 50c). Therefore, the formwork design and RAPID-code were ready to be used for final manufacturing.

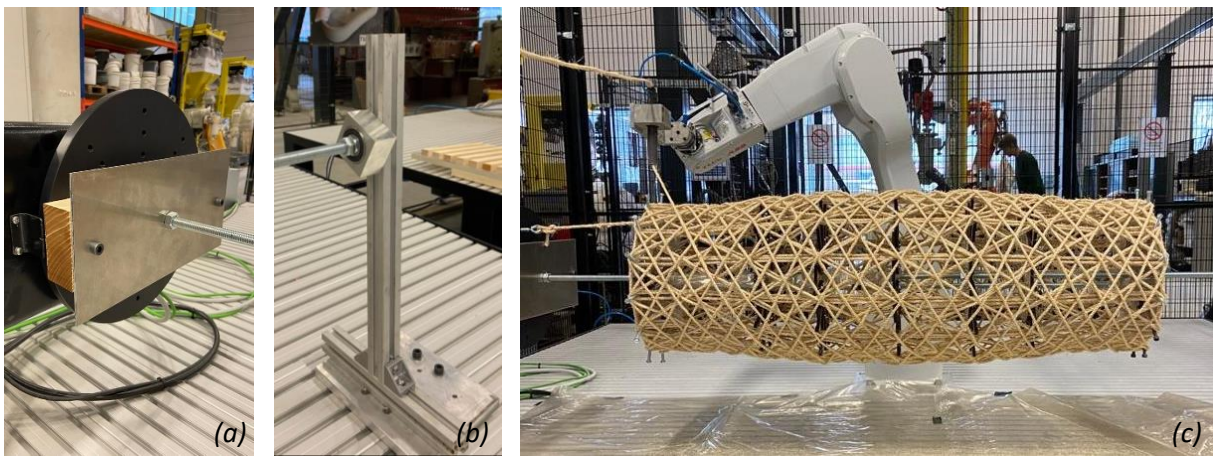

Figure 50 (a) and (b) Connection formwork to robot bed (c) Result final test manufacturing

6.2 Robotic filament winding

To manufacture the final columns by robotic filament winding, the sisal rope is impregnated with epoxy resin. The winding setup is based on the filament winding process, discussed in Section 4.3 Filament winding process. The total process is visualized by Figure 51. The required sisal rope length to wind one column is 175.4 meters. It is preferable to wind the column in one continuous session. Therefore, sisal rope spools of 220 meters are used for manufacturing. The rope is unwound from the spool and guided through a steel eye to the resin bath, where the rope is fully impregnated over 200 mm. After the resin bath, the rope passes through a rubber with a narrow circular opening to release redundant resin and create tension on the rope. The tensioned and impregnated rope is guided through another steel eye to the robot end effector, which winds the sisal rope around the created formwork.

Figure 51 Filament winding setup for manufacturing

The final RAPID Program Module and System Module scripts are loaded into Robot Studio to drive the robot and rotation table. A networking cable is used to connect the computer to the robot. The Program Module script is visible on the robot teach pendant during manufacturing, to control all movements.

As can be seen in Figure 51, the full setup is packed in PTFE-foil, to prevent material from the SED lab from being damaged by the epoxy resin. Furthermore, the formwork is packed to prevent bonding between the fork elements and the impregnated rope, and to prevent the formwork from being damaged, so that it can be reused.

In total, four columns are manufactured. A video of the manufacturing process is added to Appendix 5 Videos manufacturing process. The second column is however not fully finished. During filament winding, the end effector collided with a bolt. This caused the robot and the rotation table to be disconnected. Figure 52 shows the bolts screwed into the aluminium ring. The drill holes created for fastening the bolts are created manually, which can lead to bolts being slightly off-axis. These small imperfections caused a collision with the end effector while manufacturing the second column. For the other three columns, this problem did not arise.

Figure 52 Aluminium end node for manufacturing

6.3 Curing cycle

After filament winding, the four columns are removed from the robot bed and placed in the climate room of the SED lab, at ambient temperature. This is done to ensure a minimum temperature of 20 degrees Celsius, as described in Section 4.4 Curing. The next morning, the structures were placed for eight hours in a climate room at 40 degrees Celsius for post-curing. The full curing cycle of the four columns is provided by Table 7.

Table 7 Curing cycle of manufactured columns

Column	Temperature in degrees Celsius	Time in hours	Average relative humidity (RH)
1	20 °C (± 0.5 °C)	20 hrs	60 %
	40 °C (± 0.4 °C)	8 hrs	17 %
2	20 °C (± 0.5 °C)	20 hrs	60 %
	40 °C (± 0.4 °C)	8 hrs	19 %
3	20 °C (± 0.5 °C)	19 hrs	60 %
	40 °C (± 0.4 °C)	8 hrs	17 %
4	20 °C (± 0.5 °C)	19 hrs	60 %
	40 °C (± 0.4 °C)	8 hrs	18 %

Figure 53 Removed internal formwork after curing →

Some columns seemed to have a sticky waxy film over the sisal rope after curing. This phenomenon, called amine blush, can occur when the hardener of the two-component epoxy resin reacts with moisture and carbon dioxide (Wally, 2022). Therefore, while the columns are stored before post-curing, contact with the air should be minimized. Appendix 1 Sicomin technical datasheet describes that the structure can maximally be stored for 24 months at ambient temperature before the post-curing. It does not prescribe further requirements for storage rooms or values for relative humidity. Before post-curing, a minimum temperature of 20 degrees Celsius had to be guaranteed. Therefore, the columns were kept for a maximum of 20 hours in the climate room at 20 degrees Celsius with an average relative humidity (RH) of 60%. The RH of 60% could have caused the waxy film over the sisal rope. After the structures were fully cured, the formwork was removed. First, the fork elements are removed using a plier. Secondly, by unscrewing the six bolts that connect the aluminium plate to the aluminium ring, at both ends, the internal formwork is disconnected from the winded column. Figure 53 shows the cured structure after removing the disconnected formwork.

6.4 Final elements

Figure 54 shows the four manufactured columns, after the internal formwork is removed. It can be seen that the columns feature some imperfections. These imperfections can be caused by the connection of the formwork to the robot bed. Moreover, the formwork is manually connected at both ends of the treated rod. If the threaded rod is not tightened enough, it can cause the formwork to deflect slightly. The robot starts winding the tensioned rope tightly around the formwork, at the top of the horizontally placed column. This can result in skewing, and more convexity on one side of the column. For each new column to be manufactured, the formwork must be reconnected to the robot bed. This results in four different columns, with some having more imperfections than others.

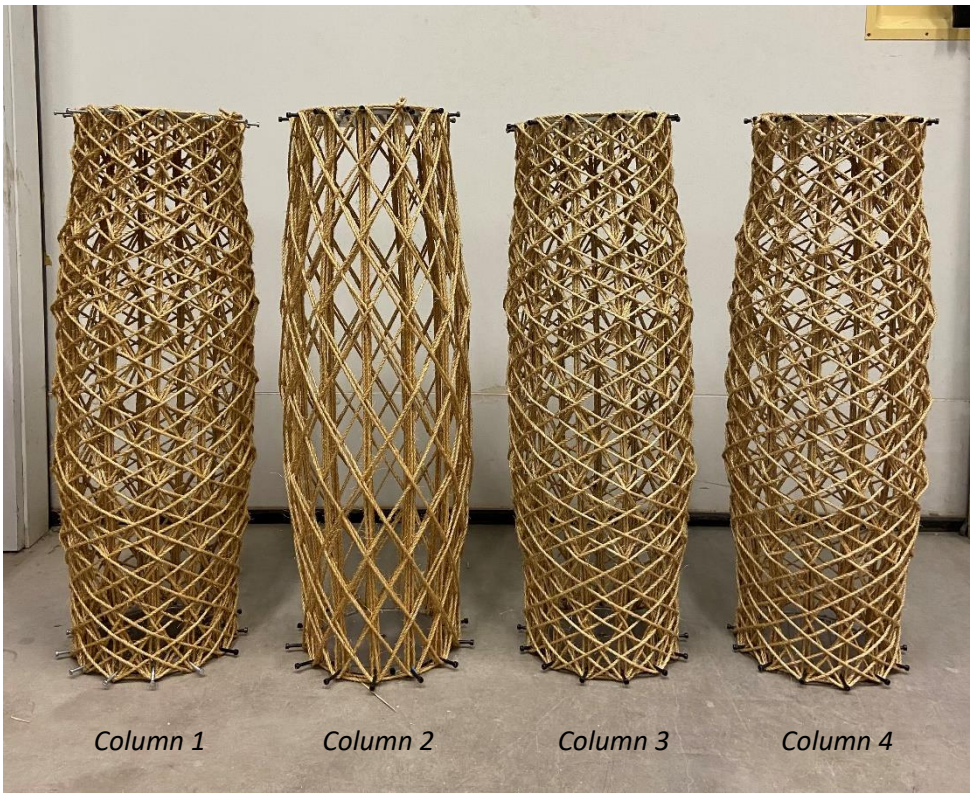

Figure 54 Final fibre composite columns after curing

6.5 End node design

The column is designed as a simply supported column, optimized for axial compression. Furthermore, the column should be able to be placed in a spaceframe. Therefore, an end node is designed to connect the column to a bolt ball node. This connection should be able to transfer the axial compressive force to the column. Figure 55 visualizes the end node design. A cone is placed at both column ends, to create a small bolt-ball node where multiple columns can be connected to. The top of the cone can be bolted to the bolt ball node by placing a sleeve over the high-strength bolt. The sleeve and bolt are connected via a dowel pin, which allows to tighten the bolt to the bolt ball.

To ensure equal force distribution and limit local effects, the inequalities of the rope should be equalized before connecting the end cone. This can be done by casting a thin layer of plaster over the sisal rope at the column ends, indicated by the red hatched area in Figure 55a. After the plaster is hardened, the U-shaped cone end can be placed over the equalized column ends. The cone is connected to the column by 13 bolts, using the bolt holes created during manufacturing. Figure 56 visualizes the final spaceframe connection. A visualization of the structural elements integrated in architectural design is added to Appendix 4 Visualizations spaceframe.

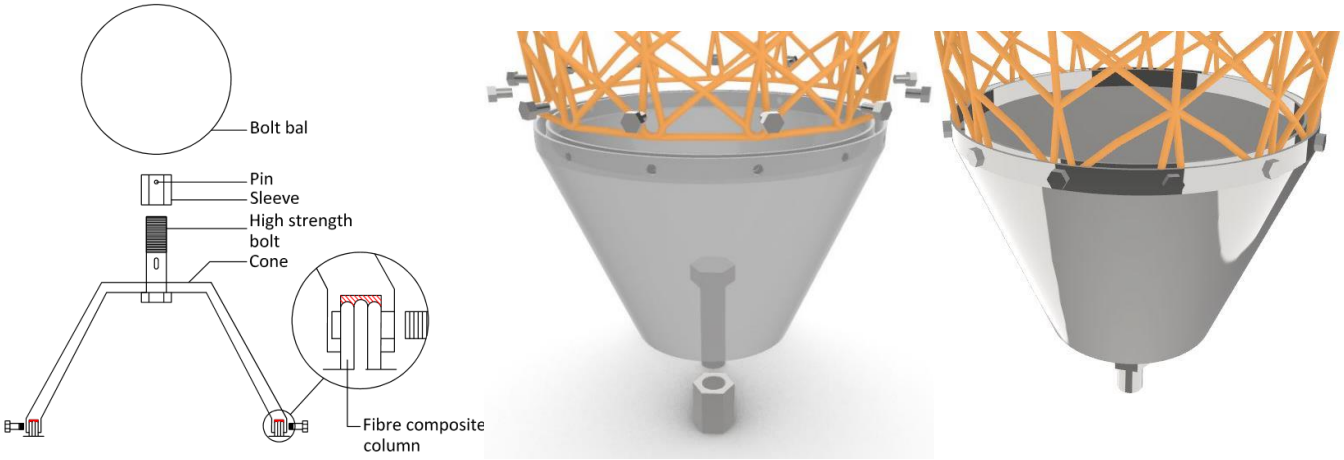

Figure 55 End node design

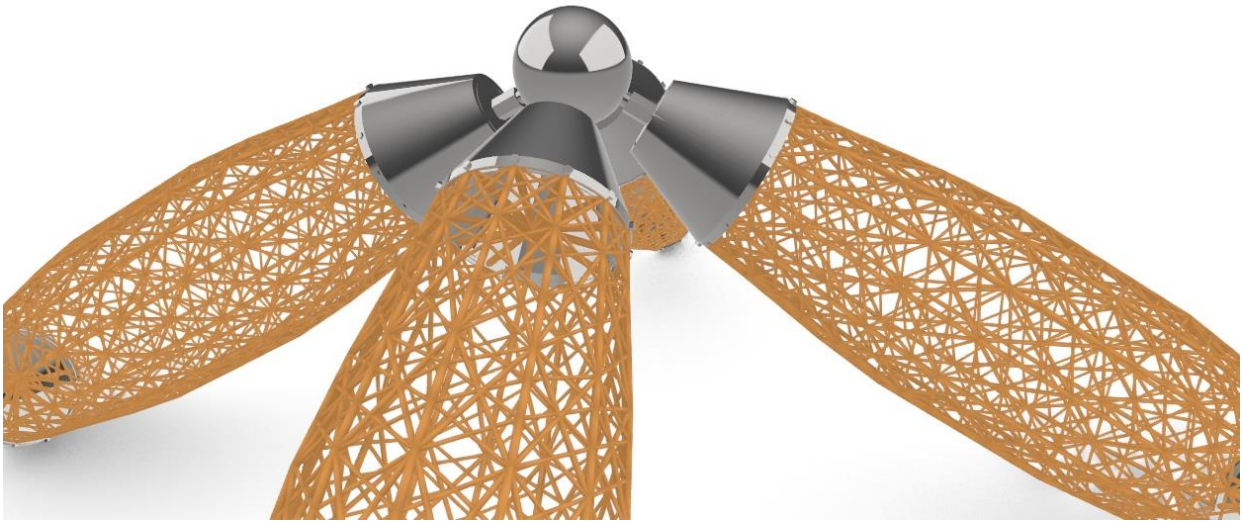

Figure 56 Spaceframe connection

7 Testing

The four fibre composite columns were tested in axial compression in the compression testing machine at the SED lab of TU/e. The columns should be simply supported. Therefore, at the column supports the structure must be free to rotate, but fixed to translate. Figure 57a shows the test setup for the first axial compression test of column 1. The aluminium end nodes used during manufacturing were not removed during this test. To prevent the aluminium from being pushed into the structure, a styrofoam ring of 50 mm was placed on top of the sisal rope. Furthermore, this foam ring should equalize rope inequalities to prevent local effects. A spherical hinge was placed at the top. A steel plate is connected to this hinge, which covers the column end and distributes the axial compressive point load over the column. At the bottom, the column was placed on a 50 mm foam ring only. This ring allows some rotation and equalizes the rope inequalities.

After testing the first column, it was discussed that the foam ring at the bottom did not allow enough rotation to mimic a pinned connection. Therefore, for the second to fourth column, a spherical hinge was placed at the top and bottom of the structural element (Figure 57b). Furthermore, the aluminium elements at the column ends should not contribute to the axial compression tests. The compression tests aimed to analyze the structural behaviour of the fibre composite columns. Therefore, the aluminium elements were removed after the first test. To equalize rope inequalities and prevent local effects, styrofoam plates of 20 mm were placed at both column ends.

For each test, three draw wire sensors were placed to measure the vertical displacement of the columns. In the first test, these sensors were connected to the bolts every 120 degrees. After removing the aluminium elements at the column ends, these sensors were connected to the steel plate in test 1b. For columns two to four, the sensors were placed between the styrofoam plates as can be seen in Figure 57b. The axial compression tests result in a force-displacement diagram incorporating the vertical displacement of the draw wire sensors and the bench displacement.

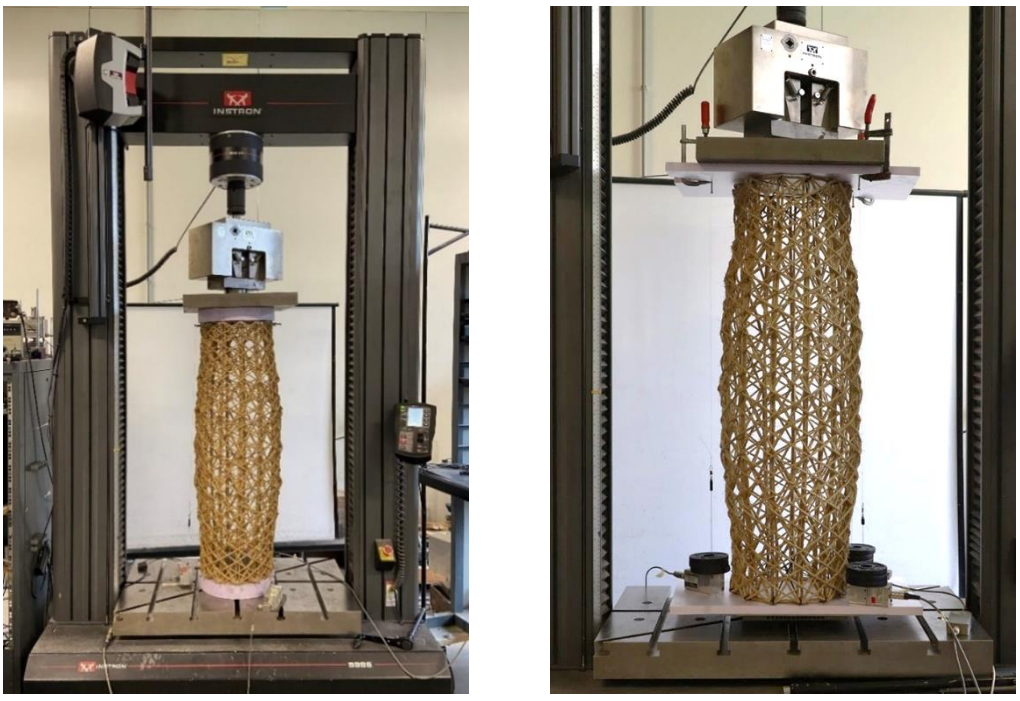

(a) *(b)*

Figure 57 Test setup axial compression test

8 Test results

8.1 Column 1

For the first test, a styrofoam ring of 50 mm was placed at both column ends. These foam rings should make sure the force is transferred to the fibre composite column, without pushing the aluminium elements into it. Furthermore, the foam should equalize rope inequalities to prevent local effects. At the top, a spherical hinge was placed to allow rotation and prevent translation. At the bottom, the styrofoam allowed the column to rotate. Three draw wire sensors were placed every 120 degrees, as can be seen in Figure 61a. These sensors were connected to the bolts that are screwed into the aluminium element. Figure 58 provides the result of the first test in a force-displacement diagram, where ADC-01 to ADC-03 represent the draw wire sensors and ADC-04 the displacement of the compression testing machine.

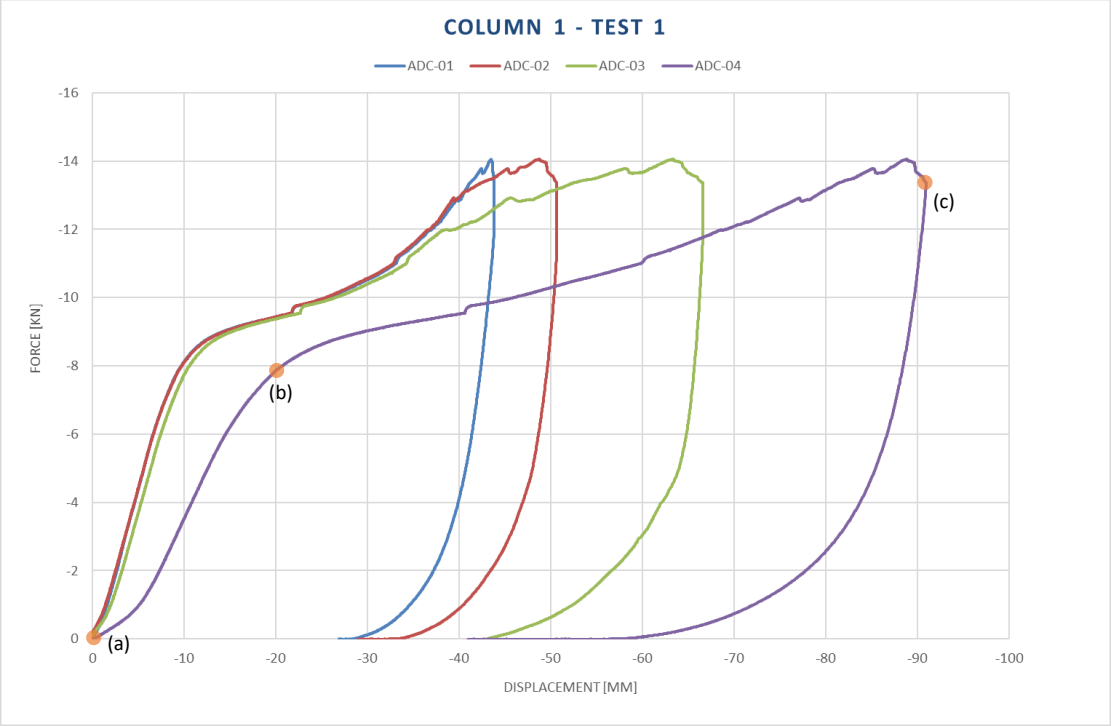

Figure 58 Force-displacement diagram axial compression test 1 – column 1

Figure 61 provides photos of the structure corresponding to points a, b and c in the graph. It can be observed that the structure behaves stiff up to a displacement of 20 mm. From the photos, it can be seen that the occurred displacement between points a and b is caused by the settlement of the ropes into the foam. In the column itself, no displacement seemed to occur in this phase. The draw wire sensors take the displacement of the bottom styrofoam into account. Since the sensors are connected to the bolts at the top, the displacement of the styrofoam ring at the top is not measured by the sensors. Therefore, the displacement of the compression testing machine is larger than the displacement measured by the draw wire sensors. From point b on, the displacement increases more significantly compared to how much the force increases. However, this decreased stiffness has nothing to do with the stiffness of the column itself, but is caused by the styrofoam being squashed. Figure 60 and 61c show the end of the first test, where it can be seen that the foam was fully crushed and pushed into the machine bed.

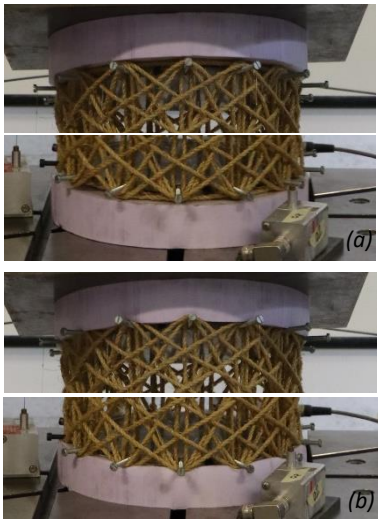

Figure 59 Settlement of the ropes into styrofoam between point (a) and (b)

The three draw wire sensors show similar behaviour up to approximately 12 kN. After this point, the displacement of ACD-03 increases strongly. From Figure 60, it can be seen that the bolt to which ADC-03 is connected, has become detached from the ropes. After the test, it was found that two ropes were not covered by the foam ring. The crushed foam pushed against these ropes, causing the aluminium element to be pushed inwards at this location. Since the draw wire sensors were connected to the bolts, the displacement measured by these sensors does not reflect the real displacement of the column.

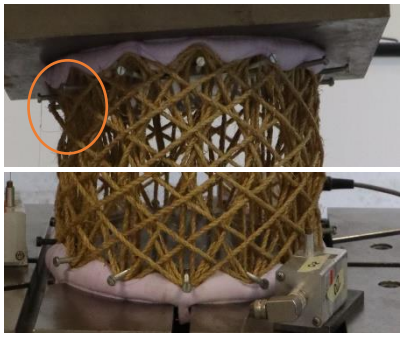

Figure 60 Situation at point (c)

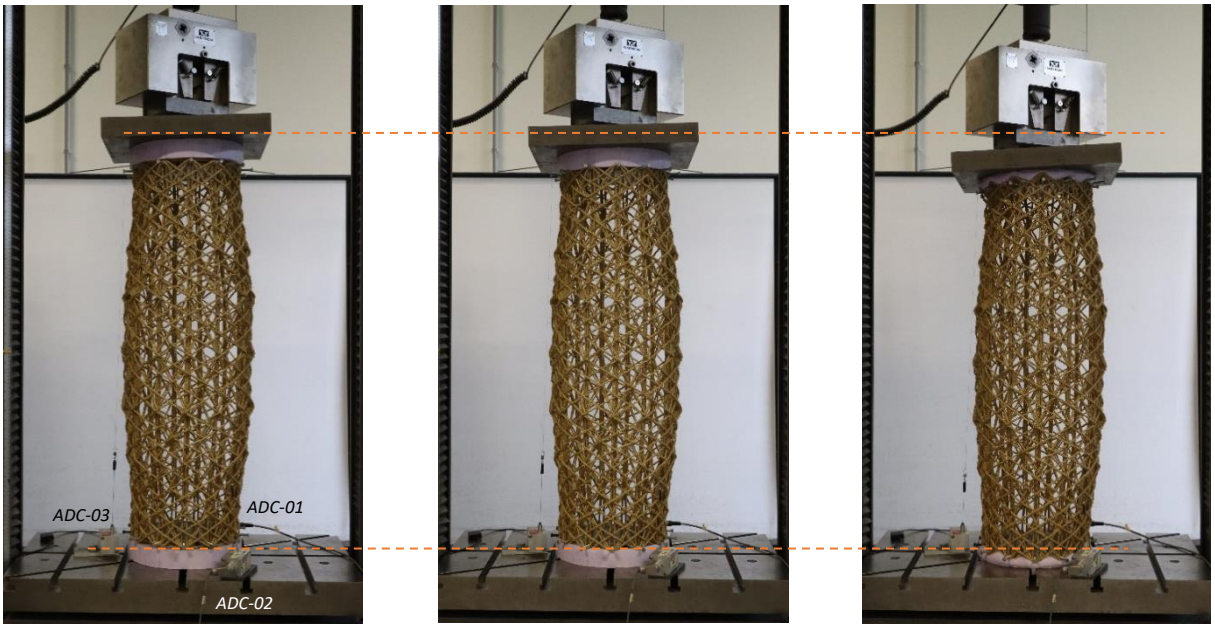

(a) *(b)* *(c)*

Figure 61 Axial compression test 1 - column 1

Just before point c, a drop in the graph can be observed. The orange circled part in Figure 60 shows that some local buckling occurred at the top of the column. After this point, the column was unloaded and the test was stopped. However, after this test, the structural behaviour of the column could not accurately be assessed. Therefore, the aluminium elements were removed from the column ends, and the column was tested again. In this test (1b), cardboard of 10 mm was placed at the column ends to equalize the rope inequalities. Furthermore, the draw wire sensors were connected to the steel plate, using magnets. Figure 62 provides the results of the compression test.

The column is placed in opposite direction in the pressure bench. Where the column started to buckle locally at the top left in test 1, is now located at the top right. Up to 10.5 kN, the column behaves stiff. The limited displacement that occurred up to this point was caused by the settlement of the ropes in the cardboard, as can be seen in Figure 63. From point b on, local buckling starts to occur at the top of the column, at the same point it started to occur in test 1. The vertical winded ropes detached from the diagonals, and buckled inwards (Figure 63c). This caused an increase in the displacement of ACD-02. Due to the spherical hinge, the other side of the steel plate was pushed upwards, resulting in a decreased displacement of ADC-03 (Figure 63c).

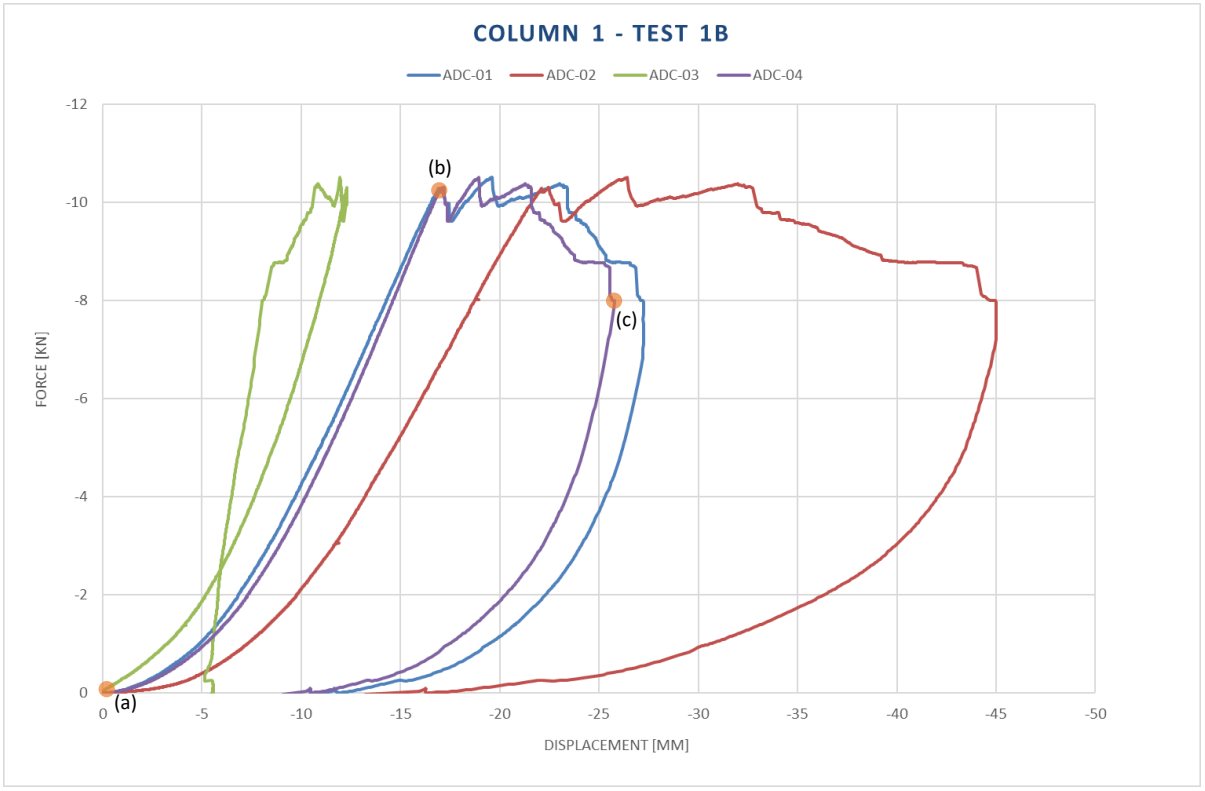

Figure 62 Force-displacement diagram axial compression test 1b – column 1

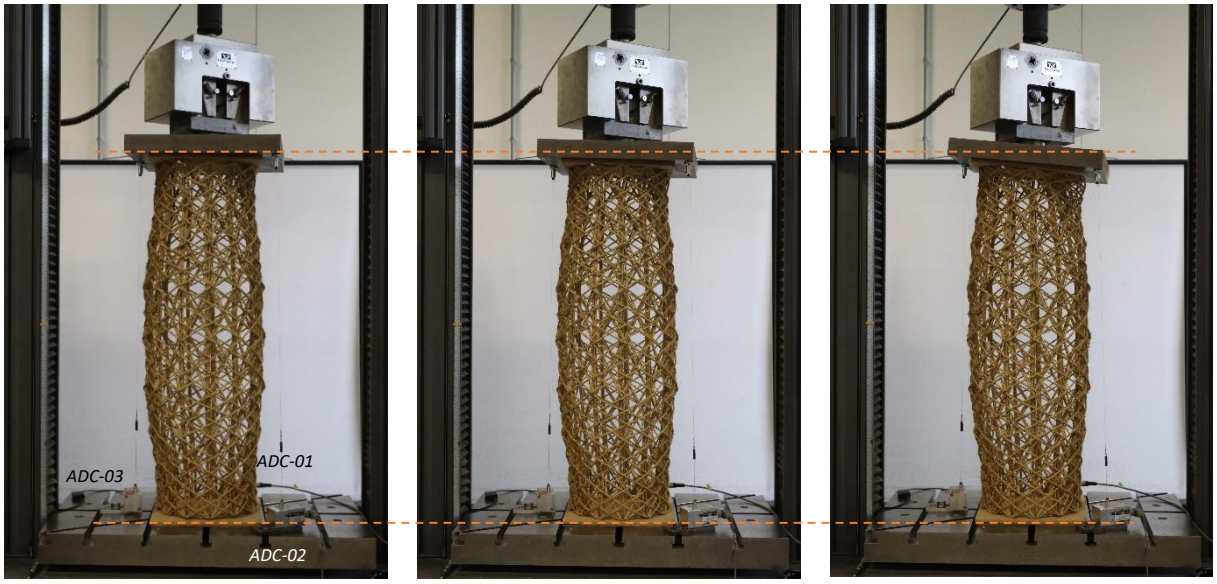

Figure 63 Axial compression test 1b - column 1

8.2 Column 2

The second column was placed in the compression testing machine between two spherical hinges. To better analyze the structural behaviour of the fibre composite column, the aluminium elements at the column ends were removed. At both column ends, a styrofoam plate of 20 mm was placed. At the bottom, three draw wire sensors were placed on top of the foam. These sensors were connected to the bottom of the top foam plate by screws. Figure 64 provides the results of the axial compression test of the second column, in a force-displacement diagram. Figure 66a shows the location of the draw wire sensors ACD-01 to ACD-03. Sensor ADC-04 represents the displacement of the testing machine.

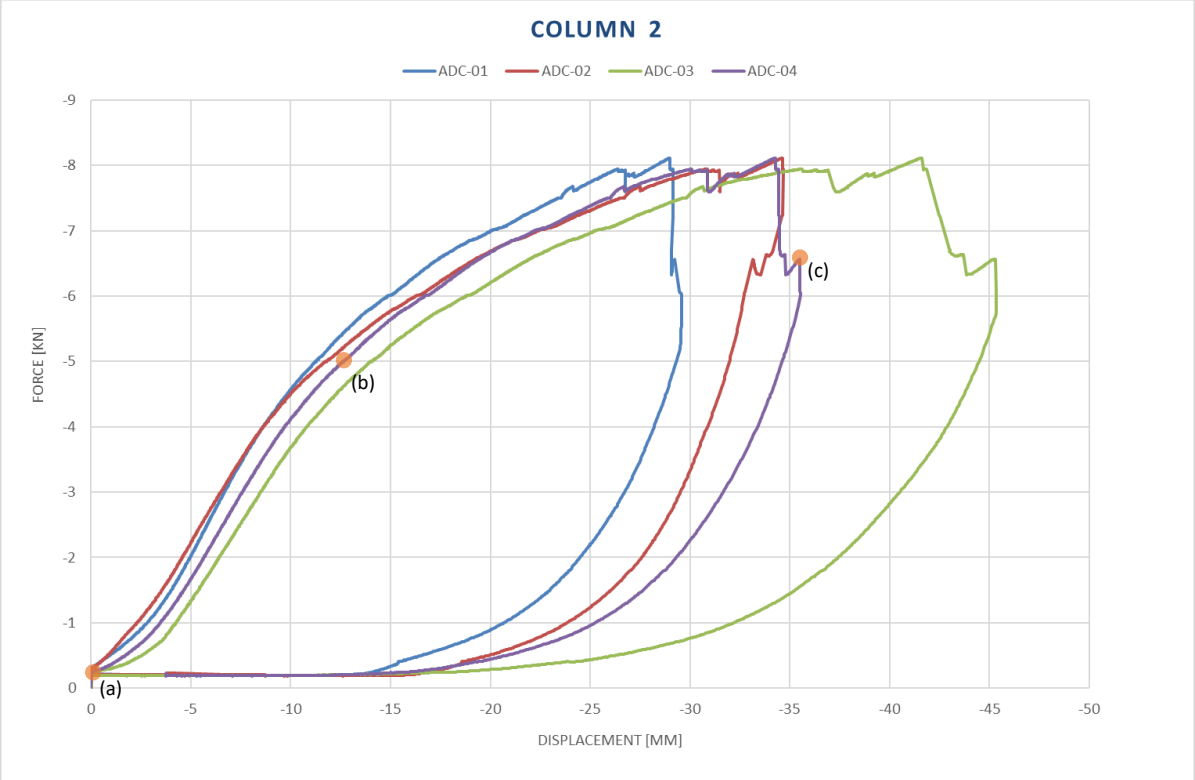

Figure 64 Force-displacement diagram axial compression test column 2

Figure 66 provides the test situation at points a, b and c, which are indicated in the graph. Up to 5 kN, stiff behaviour can be observed. Between Figure 66a and 66b, it can be seen that the displacement of 12.5 mm is caused by the settlement of the ropes into the styrofoam plate. No deformations in the column can be observed yet at this point. Between points b and c, the gap size at the location where the bolts used to be enlarges at the top. This phenomenon is explained by Figure 65 and is occurring in Figure 66c. As a result, multiple vertical winded ropes detach from the structure and buckle locally in an s-shape. This results in the rope pushing against the diagonals at some points, causing the diagonals to be pushed outwards. This phenomenon caused the increased vertical displacement measured by ADC-03 after reaching the peak load. A video of the full test is added to Appendix 6 Videos axial compression test.

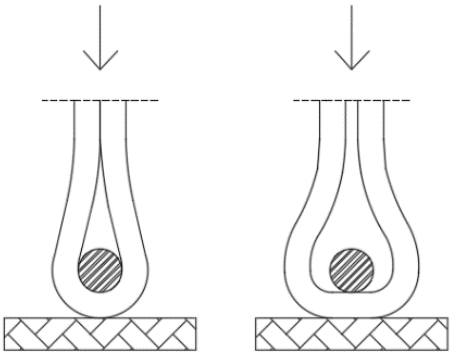

Figure 65 Local bucking sisal rope at location bolt hole

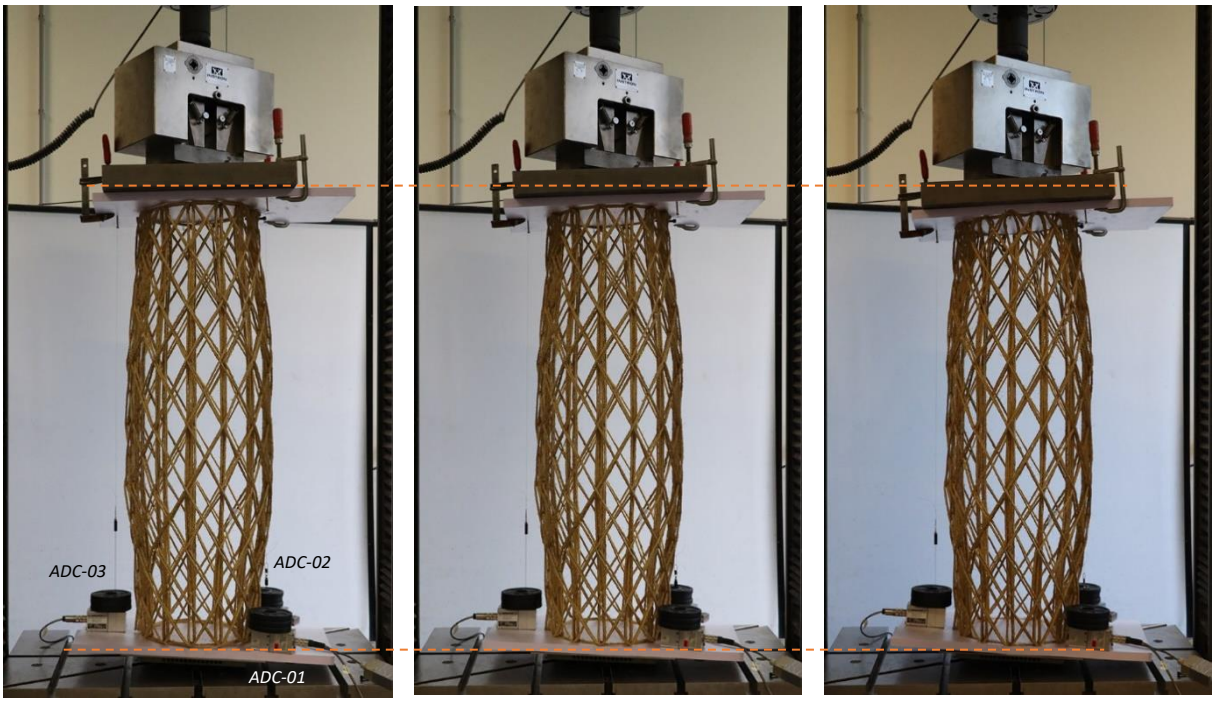

(a) *(b)* *(c)*

Figure 66 Axial compression test column 2

8.3 Column 3

The test setup for the third column is similar to that of the second column. However, for this test, cable ties were used to connect the ropes at the location where the bolts used to be (Figure 67a). These cable ties mimic the behaviour of the end node, where the U-shaped end of the end cone is placed over the ropes. This prevents the ropes at the top from buckling sideways, as occurred in Figure 60. The resulting force-displacement graph of the axial compression test is visualized in Figure 68. Furthermore, Figure 69 shows four test situations referring to points a to d in the graph.

Stiff behaviour can be observed up to point b, at approximately 7 kN. From Figure 69a and 69b, it can be seen that the small displacement measured at point b is caused by the settlement of the ropes in the styrofoam plate. Between points b and c, less stiff behaviour can be observed, which is caused by the deformation of the styrofoam plates. Figure 69c shows that the rope is fully pushed into the foam, which causes the foam to deform strongly at this location. Furthermore, pushing the ropes into the foam at the bottom causes the foam plate to move upwards around the column. Since the three draw wire sensors are placed on this foam plate, these sensors start to measure more vertical displacement than the displacement of the compression testing machine. This phenomenon is clearly visible in the video of the full test, added to Appendix 6 Videos axial compression test.

(a)

(b)

Figure 67 (a) Cable ties to mimic end node (b) Local buckling sisal rope

Up to point c, there are no visible deformations in the column (Figure 69c). From point c on, the foam between the steel plates and the ropes is fully deformed. This causes the stiff behaviour of the fibre composite column to become visible again. The force increases up to 19.7 kN, where local buckling starts to occur. Again, the gap size at the location where the bolts used to be enlarges at the top, resulting in multiple vertical winded ropes to detach from the structure and buckle locally. This results in a drop in the graph, after which the column unloading started. The resulting deformation after testing is shown in Figure 67b.

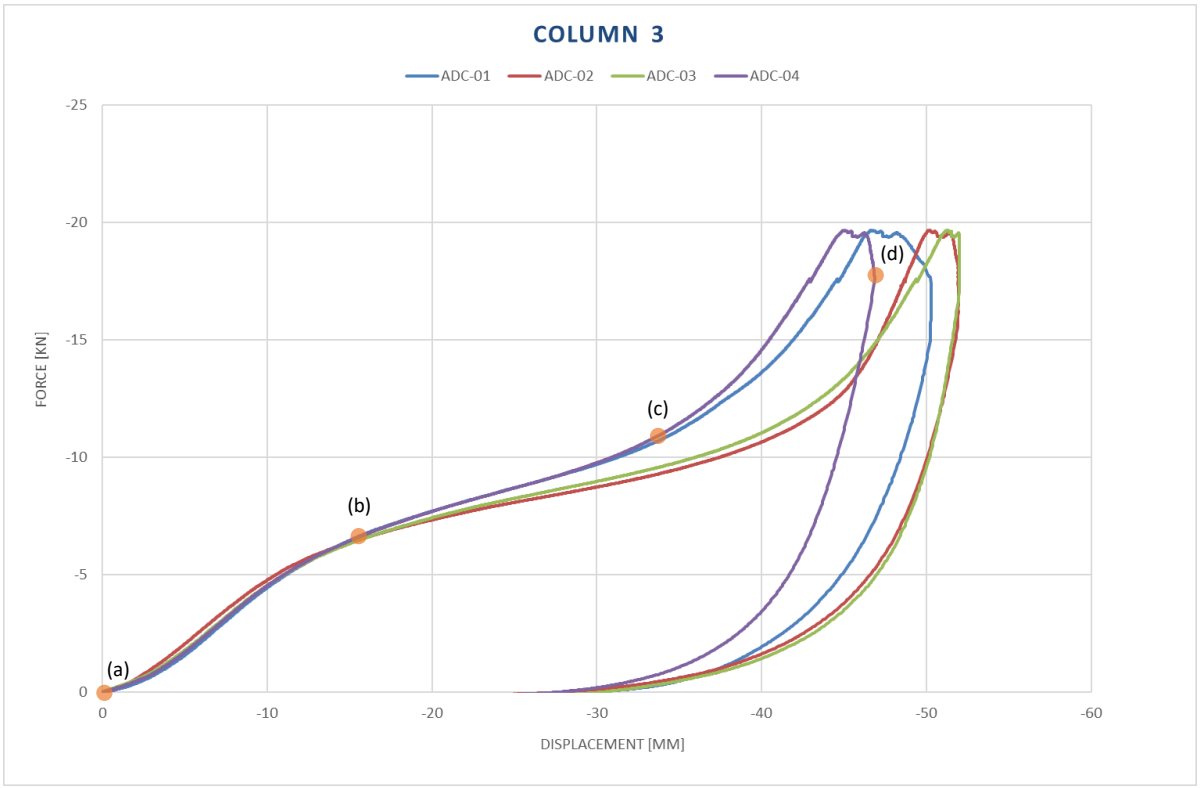

Figure 68 Force-displacement diagram axial compression test column 3

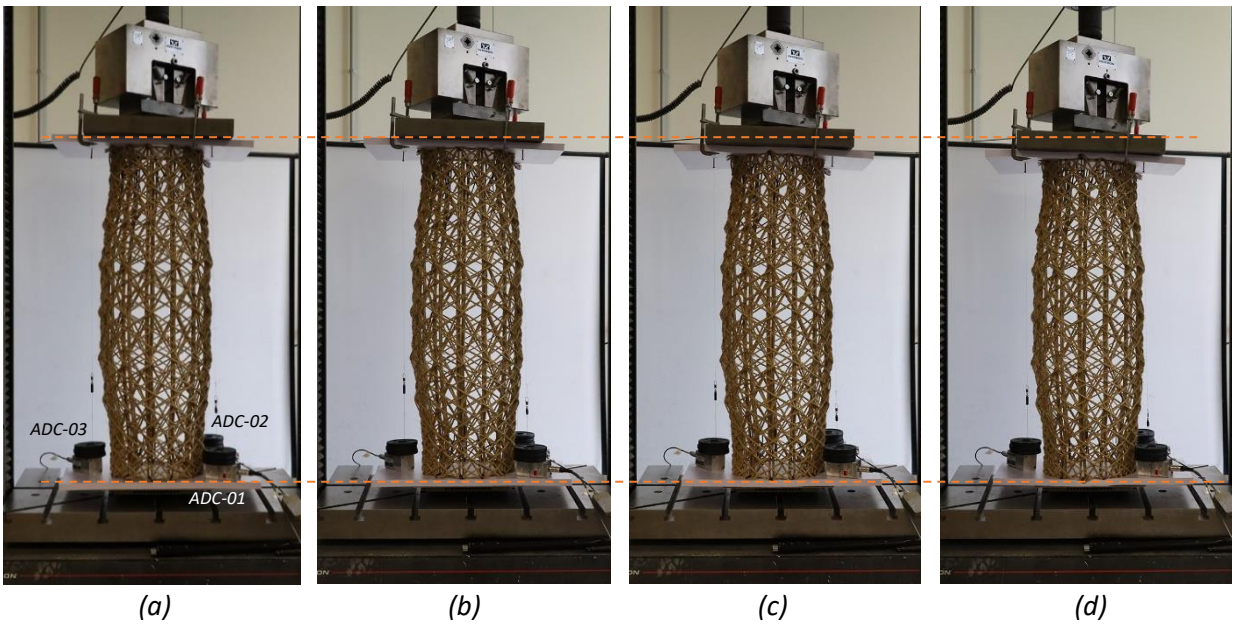

Figure 69 Axial compressive test column 3

8.4 Column 4

The fourth and final column was tested in the same manner as the third column. The test results are visualized in a force-displacement diagram in Figure 71. The observed behaviour is almost identical to that of the previously tested column. Point a to d in this graph correspond to Figure 72a to 72d. The structure behaves stiff between points a and b. The limited displacement measured in this phase is caused by the settlement of the ropes in the styrofoam (Figure 72b). Between points b and c, the displacement increases more compared to the force increase. This behaviour is caused by the ropes being fully pushed into the foam plate, as can be seen in Figure 72c. After point c, the stiff behaviour of the column becomes visible again. The force increases up to 21.4 kN, after which the force quickly drops to approximately 13 kN as a result of local buckling of the sisal rope at the top of the column (Figure 70). From the full test video added to Appendix 6 Videos axial compression test, the same failure mode as the previous tests can be observed. The gap size at the location where the bolts used to be enlarges at the top, resulting in multiple vertical winded ropes being detached from the structure and buckle inwards. Figure 73 shows the result of the column after testing, where the enlarged gap size and detached vertical winded ropes are visible.

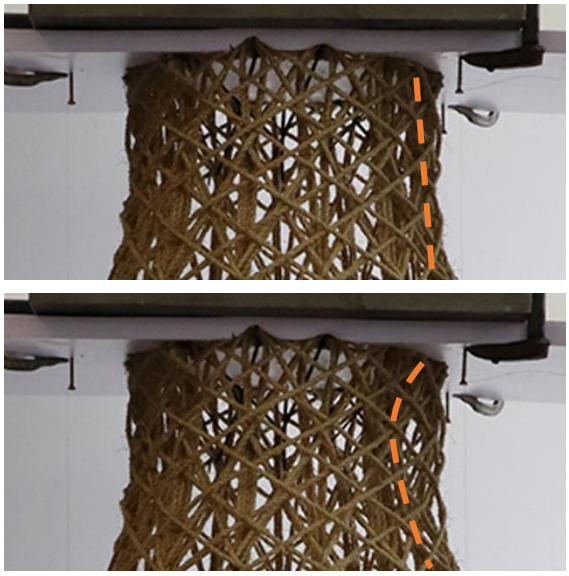

Figure 70 Local buckling occurring during axial compression test column 4

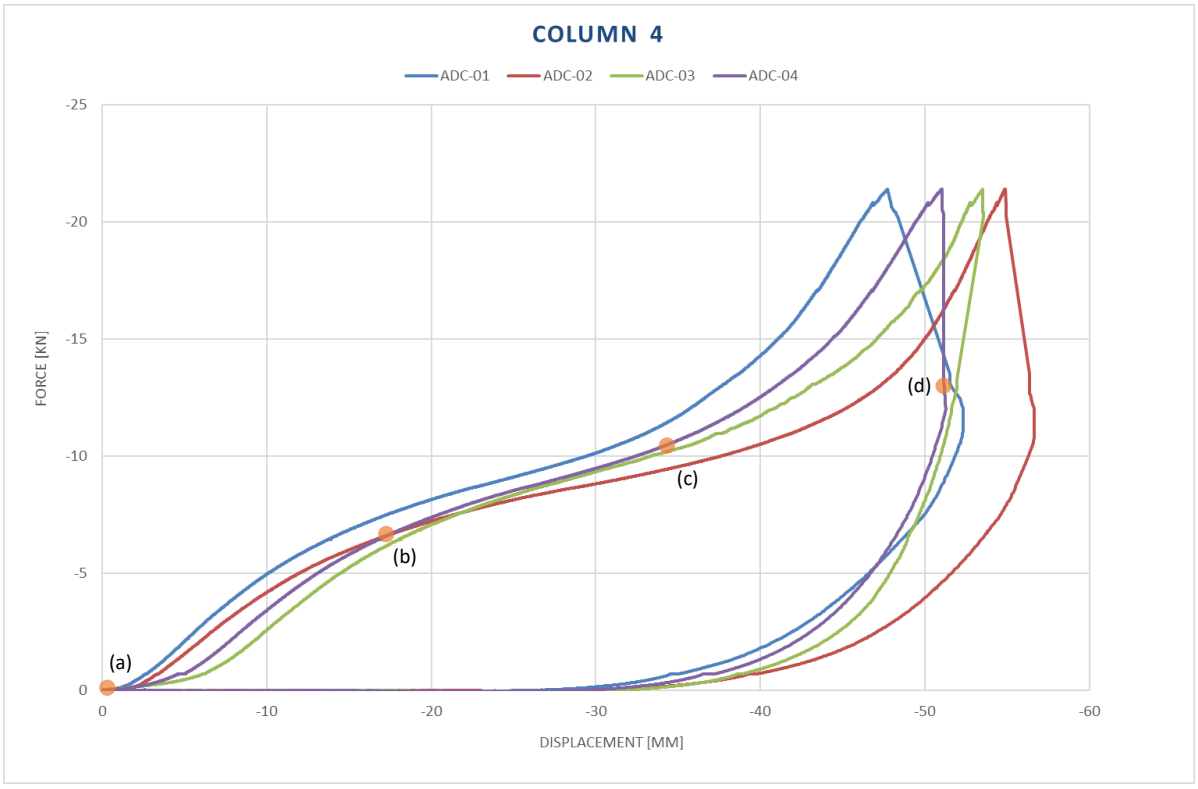

Figure 71 Force-displacement diagram axial compression test column 4

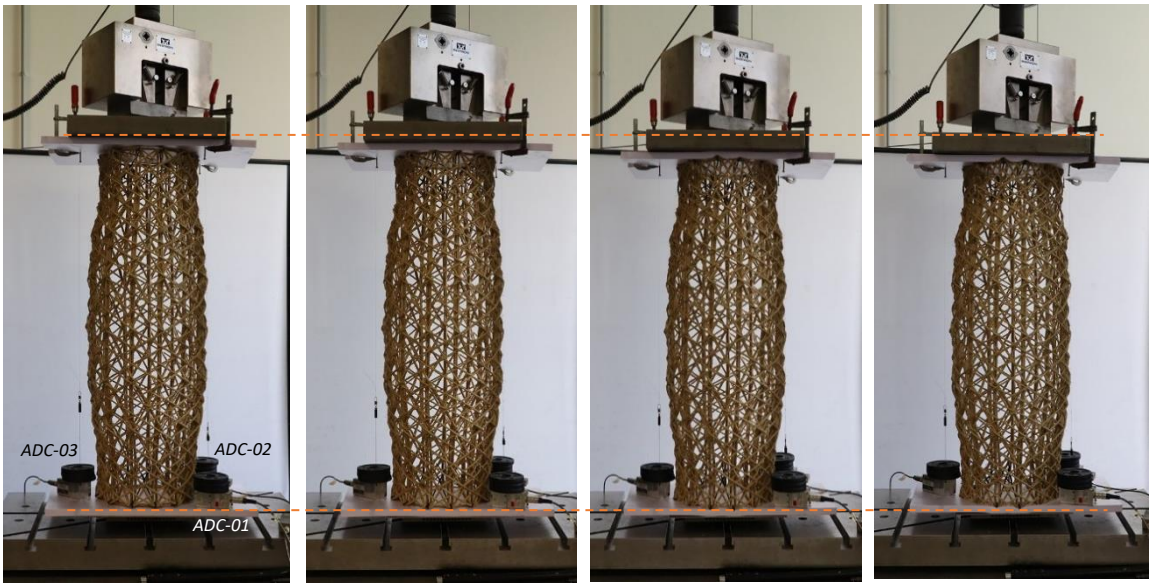

(a) *(b)* *(c)* *(d)*

Figure 72 Axial compression test column 4

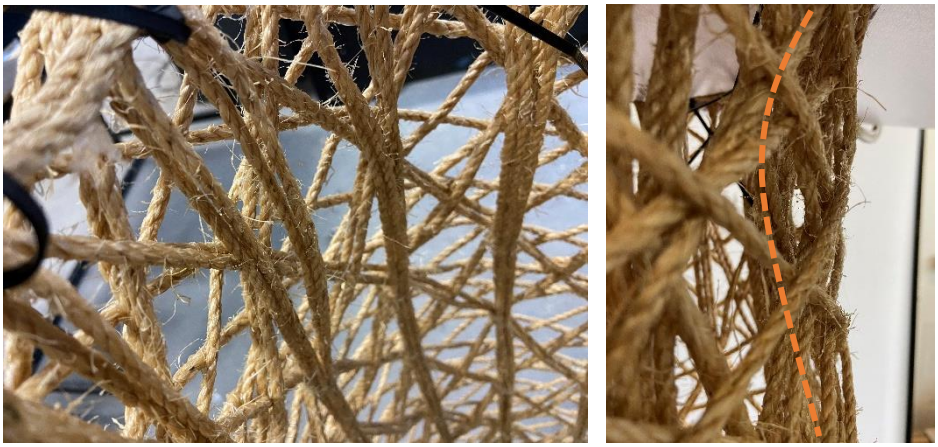

Figure 73 Visible local buckling of the sisal rope after testing

8.5 Results overview

Table 8 provides an overview of the axial compression test results, addressing the maximum compressive force reached, maximum force according to the numerical model, and failure modes. Figure 74 shows the four columns after testing.

Table 8 Test results of axial compression tests

Column	Max compressive force reached [kN]	Max force in numerical model [kN]	Factor difference [-]	Failure mechanism
1	14.06 kN	39.10 kN	2.78	Local buckling of verticals at column top
2	8.11 kN	7.08 kN	0.87	Local buckling of verticals at column top
3	19.68 kN	39.10 kN	1.99	Local buckling of verticals at column top
4	21.40 kN	39.10 kN	1.83	Local buckling of verticals at column top

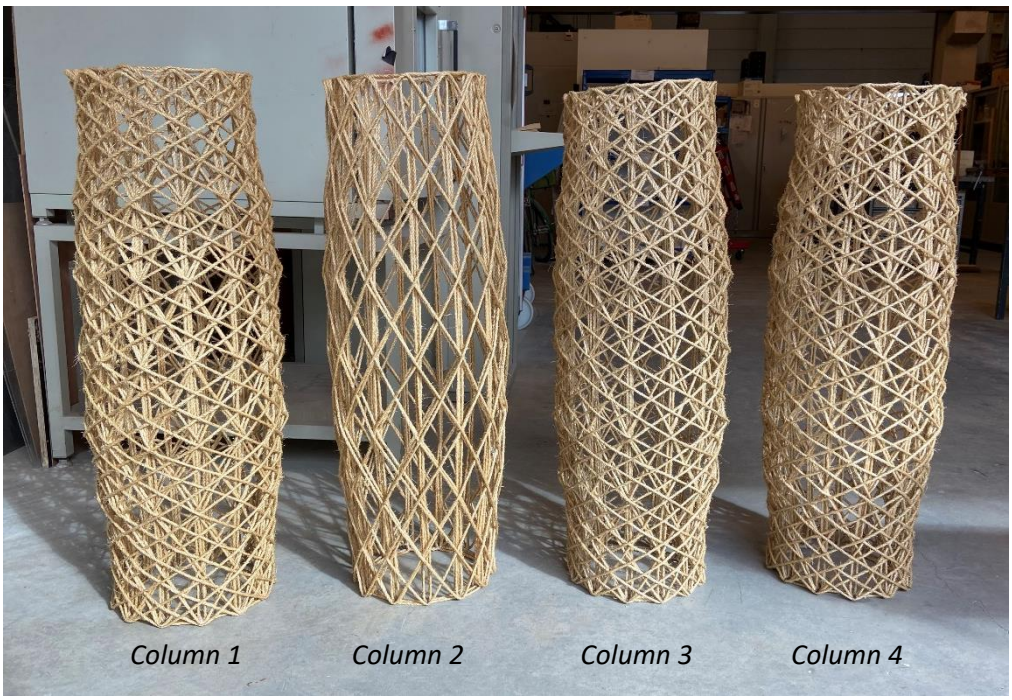

Figure 74 Four fibre composite filament winded columns after testing

9 Discussion of the results

Figure 75 provides a force-displacement diagram of the four columns combined. Up to 5 kN, the four columns show similar behaviour. After this point, the stiffness of the second column starts to decrease. This column was however not fully finished due to a robot error in the manufacturing process. Columns 1, 3 and 4 show similar behaviour up to 20 mm displacement, which is caused by the settlement of the ropes in the styrofoam. After this point, the stiffness seems to decrease for the three columns. This is however not caused by a decreased column stiffness, but by the styrofoam being completely squashed. For column 1, this phase lasts until a displacement of approximately 90 mm is measured. For columns 3 and 4, this phase lasts up to 30 mm displacement. This difference can be explained by the fact that the first column had a total styrofoam plate thickness of 100 mm, which was only 40 mm for columns 3 and 4. After the styrofoam is fully squashed, the columns show a similar stiffness as at the beginning of the tests. For the first column, this can be seen by the result of test 1b. The force increases strongly with limited deformation, until the maximum force is reached. After this point, the sisal rope buckles locally at the top of the columns, leading to a drop in the force-displacement graphs.

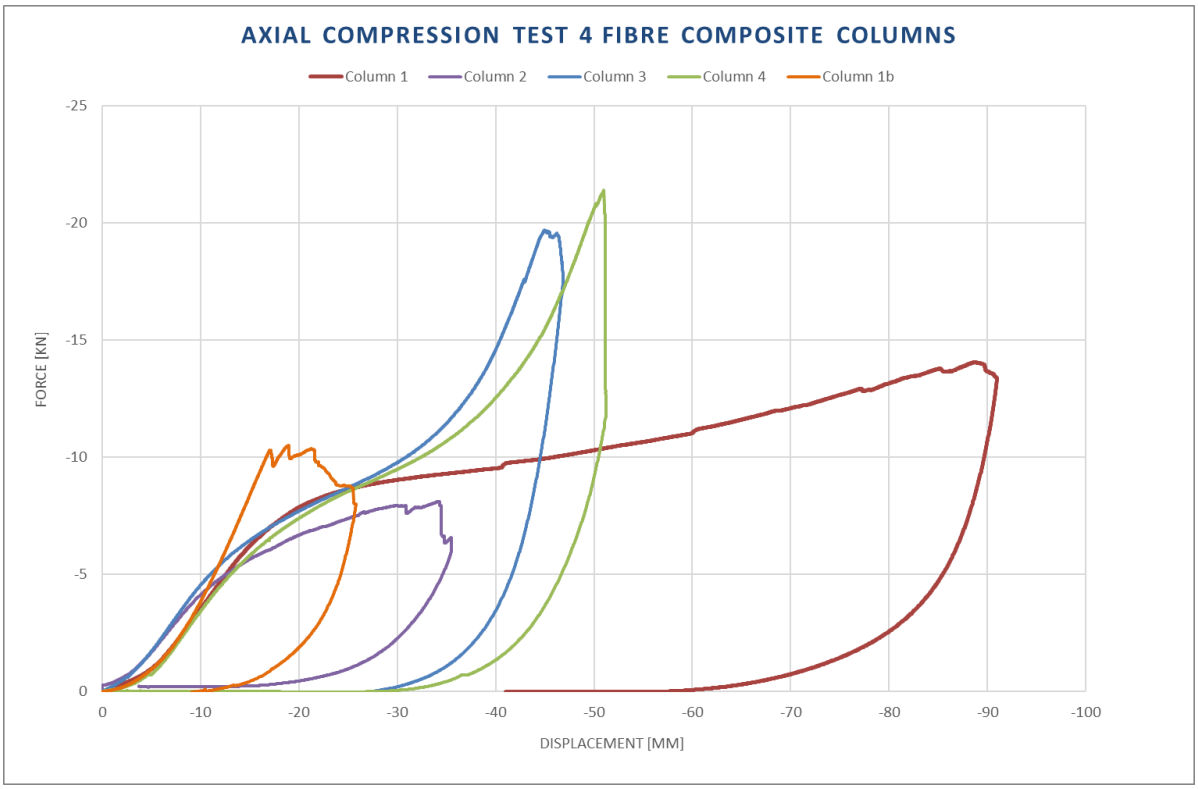

Figure 75 Force-displacement diagram of four fibre composite columns tested in axial compression

It can be discussed why local buckling of the sisal rope first occurs at the top of all columns, and not at both column ends at the same time. After manufacturing the columns, the epoxy resin still had a relatively low viscosity when placed in the climate room. The columns were placed vertically against the wall of the climate room. This caused the fluent resin to leak a bit, resulting in more resin at the bottom of the column, which was visible on the aluminium bottom plate as well. The columns were tested in the same vertical position as they were cured. An increased amount of epoxy resin can result in increased strength and bonding conditions, due to which the ropes are less likely to detach and buckle. If the columns were cured rotating in a horizontal position, failure of the columns would probably occur more symmetrical.

From Table 8, an average factor difference of 1.87 is found between the test and numerical results for the buckling load. This difference can be caused by a number of factors. First, in the numerical optimization, Karamba3D assumes perfect bonding between all ropes crossing each other. In reality, the contact area between the vertical and diagonal ropes is less, since the fibres are sequentially wrapped. This results in decreased bonding conditions, which can cause local buckling to occur before the maximum force calculated by the numerical model is reached.

Secondly, since natural fibres derive from nature, the cross-section throughout the fibre length and the mechanical properties can vary strongly due to the growth location and environmental conditions. Additionally, mechanical properties of woven fibres highly depend on the yarn twist, fibre orientation, and fibre-to-fibre cohesion. All of these factors could not be controlled for the manufactured columns.

Thirdly, moisture and relative humidity can influence the strength of the composite material. The technical datasheet of the two-component epoxy system provided no prescriptions regarding the dimensions of a storage room or the relative humidity in it. The only prescription was that a minimum temperature of 20 degrees Celsius had to be guaranteed while the columns were stored before post-curing. The only location where this could be ensured was the climate room in the SED lab with a RH of 60%. After the columns were stored for a maximum of 20 hours, the columns felt somewhat sticky already, which possibly indicated that the resin started to cure. After post-curing at 40 degrees Celsius, the columns still felt somewhat sticky. The waxy film over the sisal rope, amine blush, is possibly caused by the hardener of the two-component epoxy system reacting with the carbon dioxide and moisture in the air while stored in the climate room for 20 hours. Amine blush can affect the mechanical properties of the material, which may have affected the compressive strength of the columns.

10 Conclusions

This research project aimed to design an optimized three-dimensional lightweight structure to transfer an axial compressive force, and to manufacture this structure by robotic filament winding of resin-impregnated bio-based sisal rope. The one meter heigh structural element should be simply supported and able to be placed in a spaceframe, for which an end node is designed.

The research was started by conducting a literature study into robotic filament winding, lightweight structures, and axially loaded simply supported columns. To create a lightweight structure, material should be placed according to the flow of forces. The flow of forces and principle stresses were studied by a FEM-analysis. Moreover, it was found that buckling is the governing failure mechanism for slender structures loaded in axial compression. From this study, the three optimization goals were found, namely, minimize mass and internal elastic energy, and maximize resistance against buckling. Furthermore, it was found which geometrical shapes the optimization script should be able to generate, resulting in a set of parameters. These parameters and optimization goals are used to set up the numerical model in the parametric modelling software Rhinoceros, through a script written in Grasshopper. While changing geometrical parameters, the script searches for an optimized lightweight structure to take an axial compressive force. After the optimized geometrical design was found, an iterative sizing optimization was conducted. This iterative process distributes the material based on the strain energy. As a result, the amount of ropes increases for highly stressed lines and decreases for less stressed lines, resulting in a final design with a slightly decreased mass and an increased stiffness and buckling resistance.

After finding the optimized column design, a winding path was determined which allowed the column to be manufactured in one continuous winding session. Robot Components was used to combine all actions with the moveable work object and specified robot. This resulted in RAPID-code, which was loaded into Robot Studio to simulate the complete winding path and manufacture the structure.

For manufacturing, a non-structural formwork had to be designed which should be able to be removed after the structure was cured. Through trial and error, a final formwork design was made of MDF elements placed on a threaded rod, which could manually be connected to the rotation table. Furthermore, the design of the robot end effector was adapted several times to improve the winding process. The final structure was manufactured using a 4 mm three-strand sisal rope, impregnated with InfuGreen 810 epoxy resin and SD 8824 hardener. This material was chosen to continue on previously conducted studies at TU/e. The sisal rope was unwound from the spool and guided through a resin bath, after which the impregnated rope was tensioned by a rubber and directed to the end effector. The full filament winding process was tested multiple times before final manufacturing.

In total, four columns were manufactured, one of which was not fully finished due to the occurrence of a robot error during the manufacturing process. The columns were stored in a climate room for a maximum of 20 hours at ambient temperature, after which they were post-cured for eight hours at an elevated temperature of 40 degrees Celsius. After curing, the internal formwork was removed and small column imperfections such as skewing were noticed, caused by the manually attached formwork. Furthermore, some columns felt somewhat sticky as a result of the hardener reacting with carbon dioxide and moisture while being stored at ambient temperature before post-curing.

The cured fibre composite columns were tested in axial compression in the compression testing machine, after which an average factor difference of 1.87 was found between the test and numerical results for the buckling factor. The governing failure mechanism of the axial compression tests was local buckling. Since the filament-winded column is not one single element but an interaction of multiple elements, it is more likely that local buckling of the sisal rope occurs before global buckling of the column.

After this research, it can be concluded that it is feasible to manufacture a numerically optimized column design through robotic filament winding using biobased sisal rope. Besides some imperfections caused by the manually attached formwork and the curing process, the structural behaviour of the winded columns was promising. Further research should be conducted into the curing process of the epoxy resin and the formwork design to improve the process and conclude whether robotic filament winding with sisal rope is suitable for large-scale structural purposes.

11 Recommendations

Reflecting on the total process from numerical optimization to final testing, several elements are recommended for further research. First of all, the numerical optimization consists of two parts, an Octopus optimization to find an optimized geometrical design and an iterative sizing optimization based on the strain energy. These two optimizations can be combined into one by adapting the data management of the script. Parameters should be added to the script, so that one cross-sectional area can be set for each type of line, making use of symmetry. However, in the iterative sizing optimization the constraint is set such that the cross-sectional area may not vary more than ten percent compared to the previous cross-sectional area for each iteration. If both optimizations are combined, this will result in Octopus requiring a lot of time to find the optimal design since the amount of solutions increases significantly. Time and efficiency will have to be weighed against each other to determine whether combining the two optimizations in one improves the numerical optimization process.

Secondly, the environmental impact of the materialization should be considered. One of the aims of this research was to reduce the environmental pollution caused by the traditional design and manufacturing process of the construction sector. Therefore, the structure is completely winded of biobased sisal rope, made from natural sisal fibre. However, the SR InfuGreen 810 epoxy resin used to impregnate the sisal rope only has a carbon green content of 38%. To design a fully biobased structure, it is recommended to study epoxy resins with a higher carbon green content, but still having a favourable curing cycle and viscosity during manufacturing.

Thirdly, the formwork design should be improved to limit imperfections. For each new column manufactured, the formwork had to be reconnected to the robot bed. Since the formwork was manually connected at both ends, this resulted in some columns having more imperfections than others. Furthermore, the first formwork design using the expanding mechanisms could be improved to prevent it from rotating inwards during manufacturing. This can for example be done by using a stronger material than MDF, or by adding an additional threaded rod passing through the mechanisms to prevent it from rotating during manufacturing. If the expanding mechanism principle functions as intended, the formwork could continuously be reused resulting in time, material and waste reduction. The aluminium ends of the formwork could be improved as well. The drill holes in the aluminium ring for fastening the bolts were created manually. This resulted in some bolts being slightly off-axis, which caused a collision between a bolt and the end effector while manufacturing the second column. Automating this process would have prevented this collision. Moreover, the aluminium elements are removed after curing. It would be more efficient to wind the sisal rope around elements that can be reused to connect the end node.

Fourthly, it is recommended to examine whether the reaction of the hardener with carbon dioxide and moisture in the storage room, resulted in decreased mechanical properties. This can be done by creating five small test samples. First, a sample can be cured directly after resin impregnation. Secondly, one can be placed in a smaller storage room to limit contact with the air. Thirdly, a sample can be placed in a storage room with a lower relative humidity. Fourthly, a sample should be cured the same way as during this study. Lastly, one can be cured using similar conditions as the latter, however, using a slower hardener such as SD 4771. The mechanical properties of the five samples can be compared by conducting compressive tests. The results will have to point out whether the occurred stickiness is caused by the curing cycle, and if it influenced the mechanical properties.

Lastly, to manufacture these columns on a larger scale, the filament winding process can be improved. Disposable aluminium trays were used for the resin bath to prevent materials from the lab from being damaged by the resin. Furthermore, the SR InfuGreen 810 / SD 8824 was mixed according to the prescribed mixing ratio by weight using a weighing scale. To manufacture on a larger scale, the resin content and mixing should be controlled and a more professional winding setup should be designed. Also, the numerical script can be expanded to use it for other optimization purposes and different loading conditions as well.

Bibliography

ABB. (2022). *Product specification - IRB 1200* (Document ID: 3HAC046982-001 Revision: S). Retrieved March 14, 2023, from https://search.abb.com/library/Download.aspx?DocumentID=3HAC046982-001&LanguageCode=en&DocumentPartId=&Action=Launch

Ahmed, F. (2022, January 7). *The environmental impact of industrialization and foreign direct investment: empirical evidence from Asia-Pacific region.* SpringerLink. Retrieved from https://link.springer.com/content/pdf/10.1007/s11356-021-17560-w.pdf?pdf=button

Amziane, S., & Sonebi, M. (2016). *Overview on bio-based building material made with plant aggregate.* RILEM Technical Letters, 31-38

Arch2O. (2020, October 16). *ICD/ITKE Research Pavilion 2012.* Arch2O.com. Retrieved form https://www.arch2o.com/icditke-research-pavilion-2012/

Beukers, A. & Hinte, V. E. (2013, April 30). *Lightness: The Inevitable Renaissance Minimum Energy Structures* (4th edition). nai010 publishers

Bio-Epoxy Infusion 1800 ECO. (n.d.). Retrieved March 6, 2023, from https://www.scabro.com/epoxies/bio-epoxie/1800-eco/

Burggraf / Reichert. (2017). *ICD-ITKE Research Pavilion 2016-17 / ICD/ITKE University of Stuttgart.* Archdaily. Retrieved from https://www.archdaily.com/869450/icd-itke-research-pavilion-2016-17-icd-itke-university-of-stuttgart

BUGA Fibre Pavilion 2019 | Institute for Computational Design and Construction | University of Stuttgart. (2019). Retrieved February 7, 2023, from https://www.icd.uni-stuttgart.de/projects/buga-fiber-pavilion/

Chem Europe. (n.d.). *Buckling.* Retrieved February 28, 2023, from https://www.chemeurope.com/en/encyclopedia/Buckling.html#:~:text=In%20engineering%2C%20buckling%20is%20a,material%20is%20capable%20of%20withstanding.

Christie, J., Bodea, S., Solly, J., Menges, A. & Knippers, J. [THINkSHELL]. (2021, 30 april). *13: Filigree Shell Slabs - Christie et al* [Video]. YouTube. Retrieved September 15, 2022, from https://www.youtube.com/watch?v=Eyc1Ag98l7Q

Crawford, R. H. (2022). *Greenhouse Gas Emissions of Global Construction Industries.* IOP Publishing Ltd. Retrieved September 6, 2022, form https://iopscience.iop.org/article/10.1088/1757-899X/1218/1/012047/pdf

Estrada, R., Kannenberg, F., Wagner, H., Yablonina, M., & Menges, A. (2020). *Spatial winding: cooperative heterogeneous multi-robot system for fibrous structures.* Construction Robotics, 4(3–4), 205–215. https://doi.org/10.1007/s41693-020-00036-7

Fennell, P., Driver, J., Bataille, C. & Davis, S. (2022, March 24). *Going net zero for cement and steel.* Nature. Retrieved September 13, 2022, from https://media.nature.com/original/magazine-assets/d41586-022-00758-4/d41586-022-00758-4.pdf

Fredrickson, T. (2014, August 18). *Interview with ICD/ITKE team on fiber-woven research pavilion 2013-14.* Designboom | Architecture & Design Magazine. Retrieved from https://www.designboom.com/architecture/icd-itke-research-pavilion-2013-14-interview-08-18-2014/

Habraken, A. (2021). Lecture material Resource Efficient Structural Engineering and Design 7PP5M0. The Netherlands, Eindhoven.

Halbe, R. (2016). *Elytra Filament Pavilion, Victoria & Albert Museum.* achimmenges.net. Retrieved from http://www.achimmenges.net/?p=5922

Halbe, R. (2016, June 9). *ICD/ITKE Research Pavilion 2014-15*. DIVISARE. Retrieved from https://divisare.com/projects/319707-achim-menges-roland-halbe-www-rolandhalbe-de-icd-itke-research-pavilion-2014-15

Halbe, R. (2019). *BUGA Fibre Pavilion 2019.* achimmenges.net. Retrieved from http://www.achimmenges.net/?p=21027

Hurk, B. (2020). *The effect of moisture on the tensile strength, stiffness and maximum strain of bidirectional flax fibre reinforced epoxy* [Master thesis]. Eindhoven: Eindhoven University of Technology.

Idicula, M., Joseph, K. & Thomas, S. (2009) *Mechanical Performance of Short Banana/Sisal Hybrid Fiber Reinforced Polyester Composites.* Retrieved January 9, 2023, from https://journals.sagepub.com/doi/epdf/10.1177/0731684408095033

Jansen, D. (2021). *An integrated building method based on robotic winding* [Master thesis]. Eindhoven: Eindhoven University of Technology.

Jawaid, M., Thariq, M., & Saba, N. (2019). *Mechanical and Physical Testing of Biocomposites, Fibre-Reinforced Composites and Hybrid Composites* (Woodhead Publishing Series in Composites Science and Engineering). Woodhead Publishing. https://doi.org/10.1016/C2016-0-04437-6

Khan Academy. (n.d.). *What is elastic potential energy?* Retrieved March 31, 2023, from https://www.khanacademy.org/science/physics/work-and-energy/hookes-law/a/what-is-elastic-potential-energy

Karamba3D. (n.d.). *Welcome to Karamba3D - Karamba3D 2.2.0: The official guide to using Karamba3D 2.2.0.* Retrieved February 23, 2023, from https://manual.karamba3d.com/

Karamba3D (2.2.0.15-220706). (2022). [Computer software].

Karimah, A., Ridho, M. R., Munawar, S. S., Adi, D. S., Ismadi, Damayanti, R., Subiyanto, B., Fatriasari, W., & Fudholi, A. (2021, July 1). *A review on natural fibers for development of eco-friendly bio-composite: characteristics, and utilizations.* Journal of Materials Research and Technology; Elsevier BV. https://doi.org/10.1016/j.jmrt.2021.06.014

Leech, C. (2002, March 1). *The modelling of friction in polymer fibre ropes.* International Journal of Mechanical Sciences; Elsevier BV. https://doi.org/10.1016/s0020-7403(01)00095-9

Lepelaar, M., Hoogendoorn, A., Blok, R., & Teuffel, P. (2016). Bio-based composite pedestrian bridge. Part 2: materials and production process. In K. Kawaguchi, M. Ohsaki, & T. Takeuchi (Eds.), *Proceedings of the IASS Annual Symposium 2016 "Spatial Structures in the 21st Century", 26–30 September, 2016, Tokyo, Japan* (pp. 1-10)

Louer, L. (2022). *Optimization and Production of a Bio-based Bridge Railing through Robotic Filament Winding* [Master thesis]. Eindhoven: Eindhoven University of Technology.

Ma, Q., Rejab, R., Sahat, I. M., & Merzuki, M. N. M. (2019, January 4). *Robotic filament winding technique (RFWT) in industrial application: A review of state of the art and future perspectives.* ResearchGate. https://www.researchgate.net/publication/330132811

Menges, A. (2019). *BUGA Fibre Pavilion 2019 | achimmenges.net.* achimmenges.net. Retrieved January 5, 2023, from http://www.achimmenges.net/?p=21027

Miller, N. (2021). *The industry creating a third of the world's waste. BBC Future.* Retrieved September 6, 2022, from https://www.bbc.com/future/article/20211215-the-buildings-made-from-rubbish

Ministry of Infrastructure and Water Management. (2021, December 23). *Circular Dutch economy by 2050.* Circular economy | Government.nl. Retrieved September 13, 2022, from https://www.government.nl/topics/circular-economy/circular-dutch-economy-by-2050

Octopus. (2023, February 13). Food4Rhino. https://www.food4rhino.com/en/app/octopus

Palaniswamy, N. & Mohamed, A. (2005). *Effect of single yarn twist and ply to single yarn twist ratio on strength and elongation of ply yarns.* Journal of Applied Polymer Science, 98, 2245-2252. doi:10.1002/app.22010

Pawlyn, M. (2016, October 6). *Biomimicry in Architecture* (2nd edition). RIBA Publishing.

Ramakrishnan, T., Kumar, S., Chelladurai, S. J. S., Gnanasekaran, S., Geetha, N. K., Arthanari, R., & Debtera, B. (2022, January 28). *Effect of Moisture Content on Mechanical Properties of AAM Natural Fiber-Reinforced Isophthalic Polyester Composites.* Advances in Materials Science and Engineering; Hindawi Publishing Corporation. https://doi.org/10.1155/2022/3533143

Rhinoceros (7). (2022). [Computer software].

Rosenfield, K. (2016, February 3). *Gallery of Achim Menges to Create Robotic Pavilion for V&A.* Archdaily. Retrieved from https://www.archdaily.com/781521/achim-menges-to-create-robotic-pavilion-for-v-and-a

SCIA Engineer (21.1.3026). (2021). [Computer software].

Shah, D. U., Schubel, P. J., & Clifford, M. J. (2013). *Modelling the effect of yarn twist on the tensile strength of unidirectional plant fibre yarn composites.* In Journal of Composite Materials (Vol. 47, Issue 4). https://doi.org/10.1177/0021998312440737

Sicomin Epoxy Systems. (2017). *SR InfuGreen 810: Green Epoxy systems for Injection and Infusion* (Version 01/03/2017) [Dataset]. Sicomin. Retrieved January 16, 2023, from http://sicomin.com/datasheets/product-pdf1167.pdf

Sicomin Epoxy Systems. (2015). *SR GreenPoxy 56 Clear epoxy resin* (Version 08/12/2015) [Dataset]. Sicomin. Retrieved March 6, 2023, from http://sicomin.com/datasheets/product-pdf1152.pdf

Statistics Netherlands. (2022, June 15). *Greenhouse gas emissions 11 percent lower in Q1 2022.* Retrieved September 6, 2022, from https://www.cbs.nl/en-gb/news/2022/24/greenhouse-gas-emissions-11-percent-lower-in-q1-2022

Sustainability of biobased materials in a circular economy (n.d.). Retrieved September 12, 2022, from https://www.maastrichtuniversity.nl/research/sustainability-of-biobased-materials-circular-economy

Technical Data Sheet SUPER SAP® CLR Epoxy System. (2013, February). Fine Boat Kits. Retrieved March 6, 2023, from https://www.fyneboatkits.co.uk/data-sheets/TDS_CLR_v7-EU.pdf

urbanNext (March 15, 2023) *BUGA Fiber Pavilion: Glimpse of Future Construction.* Retrieved from https://urbannext.net/buga-fiber-pavilion/.

Väisänen, T., Das, O., & Tomppo, L. (2017). *A review on new bio-based constituents for natural fiber-polymer composites.* Cleaner Production, 149, 582-596.

Vellaichamy, P., Kumarasamy, K., Navaneetha, S., & Veerasamy, S. (2019). *Buckling Analysis of columns.* IOSR Journal of Engineering. https://www.researchgate.net/publication/344584982_Buckling_Analysis_of_columns

Wally. (2022). *Amine Blush - Composite Envisions.* Composite Envisions - Providing the Largest Selection of Composite Fabrics & Materials. Retrieved March 28, 2023, from https://compositeenvisions.com/document/amine-blush/

Zhang, D., Milanovic, N. R., Zhang, Y., Chu, P. K., & Miao, M. (2014). *Effects of humidity conditions at fabrication on the interfacial shear strength of flax/unsaturated polyester composites.* Composites Part B-Engineering, 60, 186–192. https://doi.org/10.1016/j.compositesb.2013.12.031

List of figures and tables

Figure 1 Schematization research question 9
Figure 2 Left: ICD/ITKE Research Pavilion 2012 (Arch2O, 2020) 9
Figure 3 Right: ICD/ITKE Research Pavilion 2013-14 (Fredrickson, 2014) 9
Figure 4 Left: ICD/ITKE Research Pavilion 2014-15 (Halbe, 2016) 9
Figure 5 Right: ICD/ITKE Research Pavilion 2016-17 (Burggraf / Reichert, 2017) 9
Figure 6 Left: Elytra Filament Pavilion, Victoria & Albert Museum (Halbe, 2016) 10
Figure 7 Right: BUGA Fibre Pavilion 2019 (Halbe, 2019) 10
Figure 8 Euler buckling shape and formula to predict critical load (Beukers & Hite, 2013) 10
Figure 9 Four equally stiff elements using shape and material optimization (Pawlyn, 2016) 11
Figure 10 (a) Typology optimization (b) Flow of forces (c) Principle stresses (d) Tensile stresses (e) Compressive stresses 11
Figure 11 Parameters to determine base geometry 12
Figure 12 Examples of geometrical shapes that can be generated by the Grasshopper script 12
Figure 13 Parameters to determine wire design 13
Figure 14 Convert geodesic lines into straight lines between intersection points with vertical lines 13
Figure 15 Effect of yarn twist on the tensile strength (Shah et al., 2013) 14
Figure 16 Hierarchical structure of sisal rope made from natural fibres (Leech, 2002) 14
Figure 17 Schematization (a) filament winding on a mandrel (b) coreless filament winding (Estrada et al., 2020) 17
Figure 18 BUGA Fibre Pavilion 2019 elements produced by coreless filament winding (urbanNext, 2023) 17
Figure 19 Robot Studio illustration of ABB IRB 1200-5/0.9 and rotation table placed on robot bed 18
Figure 20 End effector designed by Louer (2022) and Jansen (2021) 18
Figure 21 Final design end effector 19
Figure 22 Filament winding process (Louer, 2022) 19
Figure 23 Duration to wind one column (Robot Studio) 20
Figure 24 Internal elastic energy (Khan Academy, n.d.) 22
Figure 25 Process model numerical optimization 23
Figure 26 LineToBeam component (Karamba3D) 24
Figure 27 Defined supports (Karamba3D) 24
Figure 28 Visualization of the supports, stiff elements, and point load on the structure 24
Figure 29 Defined loads (Karamba3D) 24
Figure 30 Overview Karamba3D structural analysis in Grasshopper script 25
Figure 31 Octopus component for geometrical optimization 25
Figure 32 Solutions Octopus optimization 26
Figure 33 Design resulting from Octopus optimization (Rhinoceros) → 26
Figure 34 First buckling modes Karamba3D (left) and SCIA Engineer (right) 27
Figure 35 Process model iterative sizing optimization 28
Figure 36 Start of the iterative loop (Grasshopper) 28
Figure 37 Calculate equivalent radius (Grasshopper) 28
Figure 38 Structural analysis final design (a) before and (c) after sizing optimization, with corresponding buckling modes (b) before and (d) after sizing optimization. (e) Principle stress analysis 29
Figure 39 Create an Eulerian path using the Leafvein plug-in (Grasshopper) 30
Figure 40 Eulerian path for robotic winding, visualized from left to right 30

Figure 41 (a) Robot path and plane orientation end effector, rotation table and first target point (b) Aligned plane orientations of target points (Rhinoceros) 31
Figure 42 Robot movement creation (Grasshopper) 31
Figure 43 Robot Components visualization of robotic winding 32
Figure 44 Simulation Robot path (Robot Studio) 32
Figure 45 Elements expanding mechanism 33
Figure 46 3D-view of expanding formwork 33
Figure 47 Expanding mechanism 34
Figure 48 Test manufacturing with expanding formwork 34
Figure 49 Final formwork design 35
Figure 50 (a) and (b) Connection formwork to robot bed (c) Result final test manufacturing 35
Figure 51 Filament winding setup for manufacturing 36
Figure 52 Aluminium end node for manufacturing 37
Figure 53 Removed internal formwork after curing → 37
Figure 54 Final fibre composite columns after curing 38
Figure 55 End node design 39
Figure 56 Spaceframe connection 39
Figure 57 Test setup axial compression test 40
Figure 58 Force-displacement diagram axial compression test 1 – column 1 41
Figure 59 Settlement of the ropes into styrofoam between points (a) and (b) 41
Figure 60 Situation at point (c) 42
Figure 61 Axial compression test 1 - column 1 42
Figure 62 Force-displacement diagram axial compression test 1b – column 1 43
Figure 63 Axial compression test 1b - column 1 43
Figure 64 Force-displacement diagram axial compression test column 2 44
Figure 65 Local bucking sisal rope at location bolt hole 44
Figure 66 Axial compression test column 2 45
Figure 67 (a) Cable ties to mimic end node (b) Local buckling sisal rope 45
Figure 68 Force-displacement diagram axial compression test column 3 46
Figure 69 Axial compressive test column 3 46
Figure 70 Local buckling occurring during axial compression test column 4 47
Figure 71 Force-displacement diagram axial compression test column 4 47
Figure 72 Axial compression test column 4 48
Figure 73 Visible local buckling of the sisal rope after testing 48
Figure 74 Four fibre composite filament winded columns after testing 49
Figure 75 Force-displacement diagram of four fibre composite columns tested in axial compression 50

Table 1 Differences in mechanical properties of natural sisal fibre 14
Table 2 Carbon green content for different epoxy systems 15
Table 3 Tensile test results of single fibre and bundles fibre specimens of sisal rope Ø 4 mm cured with Sicomin SR InfuGreen 810 epoxy resin and SD 8824 hardener (Louer, 2022) 16
Table 4 Parameter input final design 26
Table 5 Verification of Karamba 3D structural analysis in SCIA Engineer 27
Table 6 Structural analysis before and after sizing optimization 29
Table 7 Curing cycle of manufactured columns 37
Table 8 Test results of axial compression tests 49

Appendixes

Appendix 1 Sicomin technical datasheet

Appendix 2 Product specifications ABB IRB 1200-5/0.9

Appendix 3 Overview Grasshopper scripts

Appendix 4 Visualizations spaceframe

Appendix 5 Videos manufacturing process

Appendix 6 Videos axial compression test

Appendix 1 Sicomin technical datasheet

Numerical optimization and manufacturing of a bio-based 3D structure through robotic filament winding

L.P.J. Krijnen

Eindhoven, May 2023

SR InfuGreen 810

Green Epoxy systems for Injection and Infusion

The ***InfuGreen* 810** is a two-component epoxy system. It has been specially formulated for resin transfer processes, such as injection or infusion.
This system has a very low viscosity at ambient temperature.
The different hardeners allow the production of small to very large parts.
The cured system gives a temperature resistance up to 100°C (Tg onset)
The hardeners SD 4770 and 4771 are designed for very thick laminates by infusions.

***SR InfuGreen* 810** Epoxy resin is produce with about 38 % of carbon from plant origin and has a lower environmental impact than standard Epoxy systems.
The bio-based Carbon content of our resin is certified by an independent laboratory using Carbon 14 measurements (ASTM D6866 or XP CEN/TS 16640).
This percentage is function of the carbon origin contained in the epoxy molecule.

***SR InfuGreen* 810** is DNV-GL *Maritime* approved DNV·GL.

GreenPoxy®

Sicomin, 31 avenue de la Lardière, 13220 Châteauneuf les Martigues, France
T: +33 (0)4 42 42 30 20 / F: +33 (0)4 42 81 29 29 / E: info@sicomin.com / www.sicomin.com

Epoxy resin *SR InfuGreen* 810

Aspect		Clear liquid
Color Gardner		1 maximum
Viscosity (± 20 % mPa.s)	@ 15 °C	2 200
	@ 20 °C	1200
	@ 25 °C	750
	@ 30 °C	470
	@ 40 °C	210
Carbon Green content (± 3 %)	GreenPoxy®	38 %
Density	@ 20 °C	
Pycnometer (±0.01)		1.16
Helium (±0.005)		1.152
Refractive index (± 0.0020)	@ 25 °C	1.5491

Storage stability	24 Months @ ambient temperature

Can crystallize at low temperature or after a long storage.
If SR InfuGreen 810 develops a haziness or crystallizes during storage, warming it @ 50 to 60 °C, with stirring, will restore it to its original state

Hardeners SD 882x SD 477x

Reference		SD 8825.2	SD 8824	SD 8822	SD 4772	SD 4771	SD 4770
Reactivity type		**Fast**	**Standard**	**Slow**		**Ultra-slow**	**Mega slow**
Aspect / colour		Light yellow liquid					
Color Gardner		3 maximum	4 maximum	5 maximum	3 maximum		
Viscosity (+ 20 % mPa.s)	@ 15 °C	9	7	27	13		
	@ 20 °C	7	6	20	11		
	@ 25 °C	6	5	16	9		
	@ 30 °C	5	4	13	7		
	@ 40 °C	4	3	9	5		
Carbon Green content	%	none					
Storage stability	AT	24 months Hardeners react with carbon dioxide and moisture. Keep tightly closed packaging, minimize maximum contact with the air.					
Density Pycnometer (±0.010)	@ 20 °C	0.915	0.944	0.935	0.927	0.944	0.944
Refractive index (± 0.002)	@ 25 °C	1.4785	1.4982	1.4712	1.4822	1.4594	1.4604

SR InfuGreen 810 / SD 8822 SD 477x Mixes

References		SD 8825.2	SD 8824	SD 8822	SD 4772	SD 4771	SD 4770
Mixing ratio by weight		100 / 22	**100 / 22**	**100 / 31**	**100 / 29**		
Mixing ratio by volume		100 / 28	**100 / 27**	**100 / 39**	**100 / 36**		
Initial mix viscosities	@ 20 °C	230	200	320	330	235	142
	@ 30 °C	130	100	120	90	115	100
Time to reach 300 cps “ Optimal infusion time’’	@ 20 °C	28’	44’	/	/	60’	3 h 20’
	@ 30 °C	40’	50’	67’	90’	130’	160’
Carbon Green content maximum Calculated (+/- 3 %)	GreenPoxy®	31	31	29	29	29	29

Viscosities increase on 1 mm film thickness

@ 20 °C

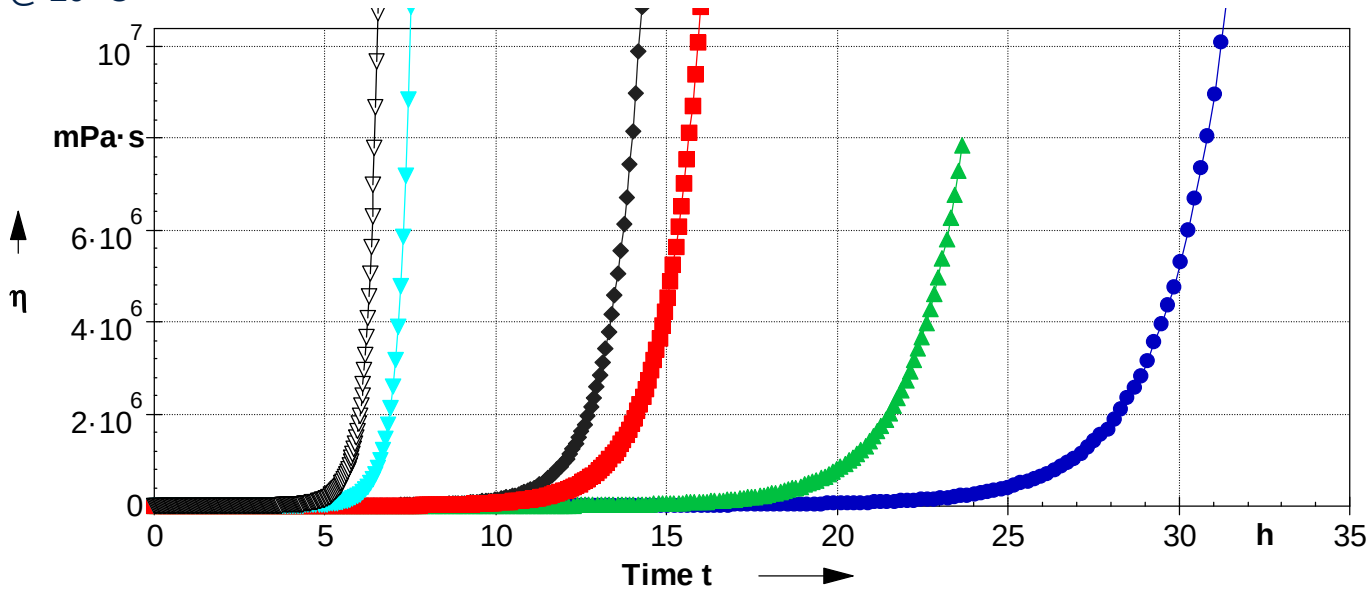

- InfuGreen 810 / SD 4770 @ 20°C
- InfuGreen 810 / SD 8822 @ 20°C
- InfuGreen 810 / SD 4771 @ 20°C
- InfuGreen 810 / SD 8824 @ 20 °C
- InfuGreen 810 / SD 4772 @ 20 °C
- InfuGreen 810 / SD 8825.2 @ 20°C

Zoom initial @ 20 °C

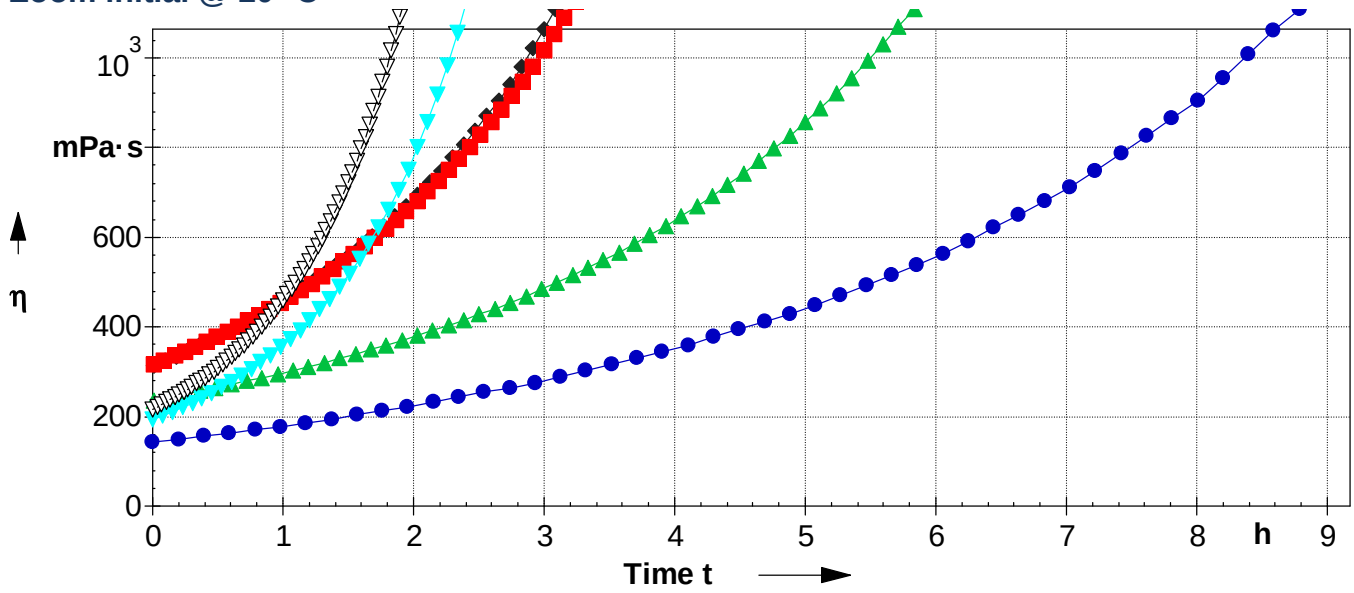

- InfuGreen 810 / SD 4770 @ 20°C
- InfuGreen 810 / SD 8822 @ 20°C
- InfuGreen 810 / SD 4771 @ 20°C
- InfuGreen 810 / SD 8824 @ 20 °C
- InfuGreen 810 / SD 4772 @ 20 °C
- InfuGreen 810 / SD 8825.2 @ 20°C

@ 30 °C

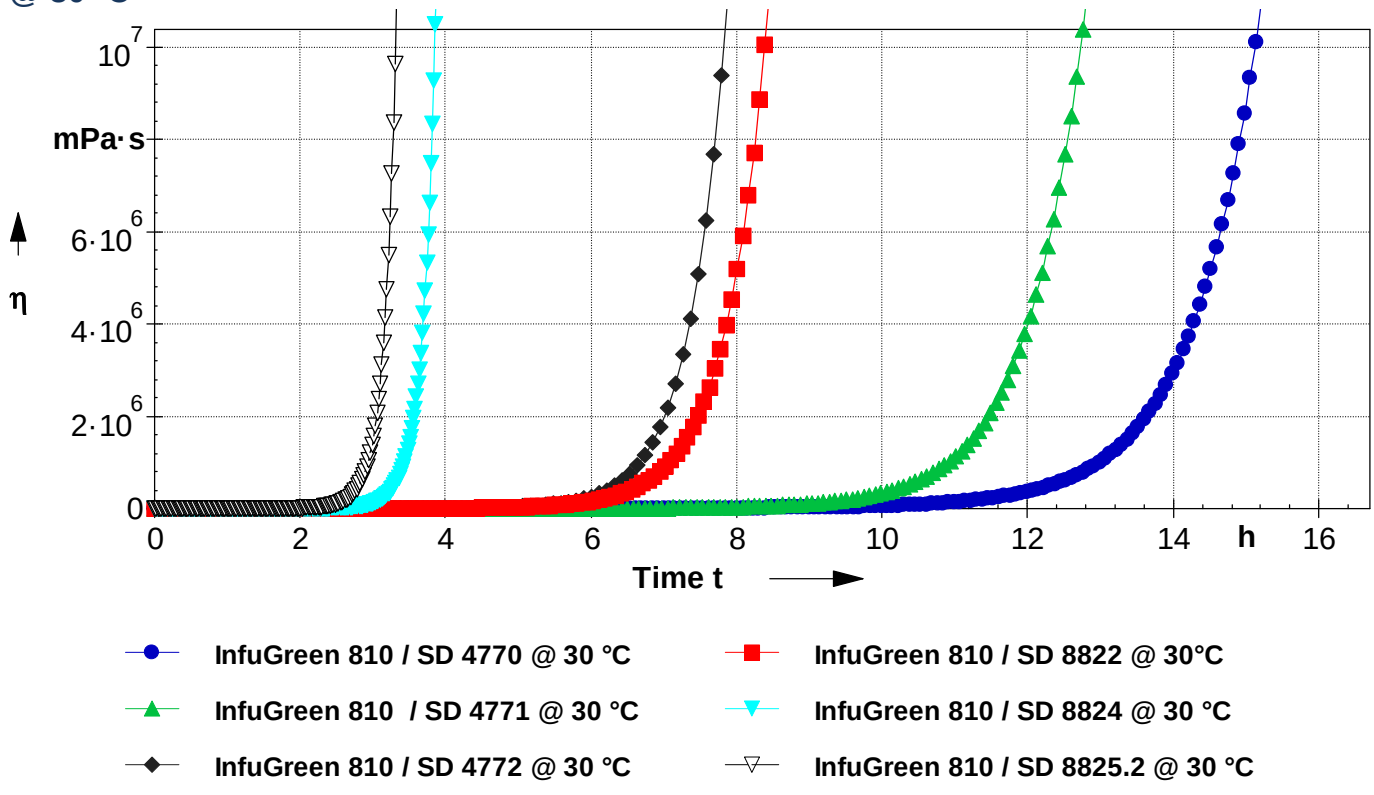

Zoom initial @ 30°C

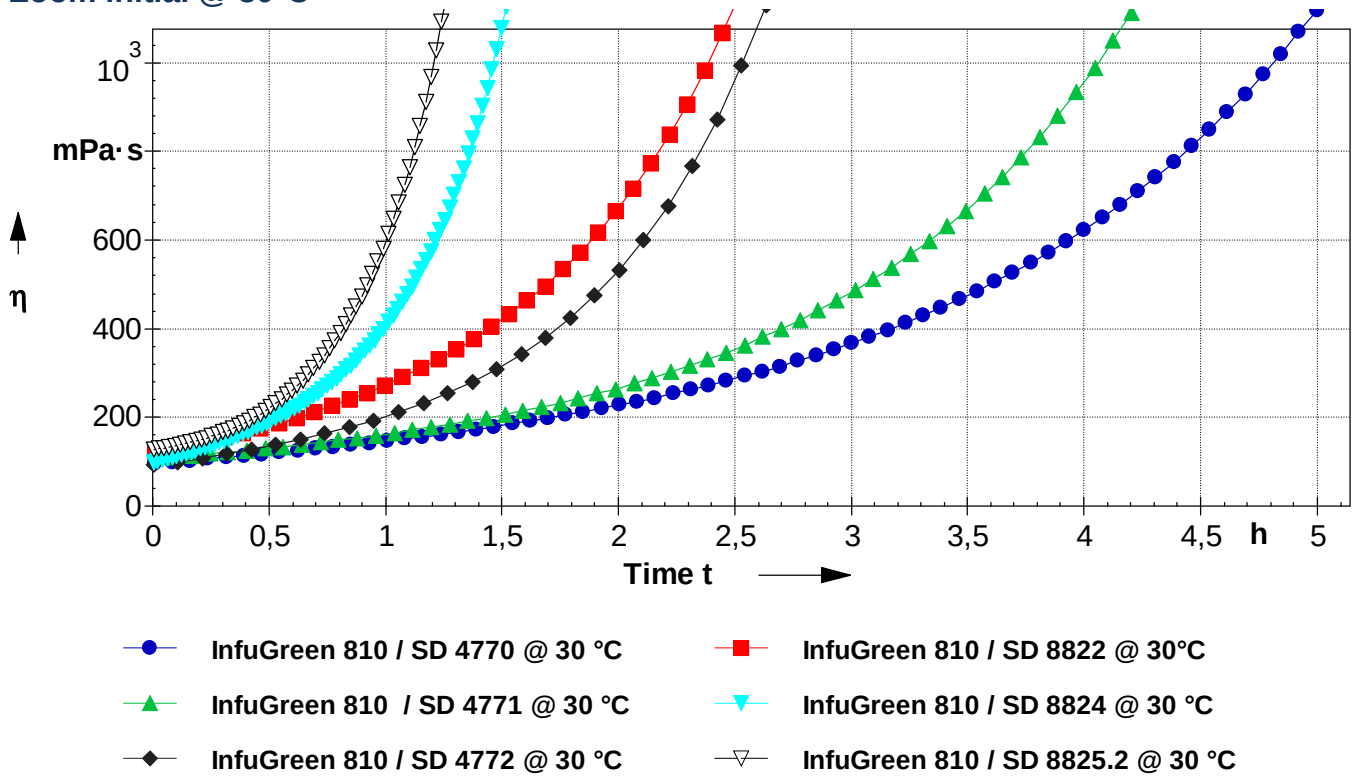

Mechanical properties on cast resin

		***SR InfuGreen* 810 / SD 8825.2**			***SR InfuGreen* 810 / SD 8824**		
Curing cycle →		AT + 24 hrs 40 °C	AT + 16 hrs 60 °C	AT + 8 hrs 80 °C	AT + 8 hrs 40 °C	AT + 16 hrs 60 °C	AT + 8 hrs 80 °C
Tension							
Modulus of elasticity	N/mm^2	3000	2700	2600	3000	2800	2600
Maximum resistance	N/mm^2	69	68	67	68	65	60
Resistance at break	N/mm^2	55	53	64	57	57	52
Elongation at max.load	%	3.8	4.8	5.7	3.6	4.4	5.0
Elongation at break	%	5.9	9.1	8.0	5.3	5.9	9.5
Flexion							
Modulus of elasticity	N/mm^2	3000	2700	2600	3100	2800	2600
Maximum resistance	N/mm^2	113	112	108	109	107	101
Elongation at max.load	%	4.9	6.1	6.6	4.6	5.7	6.0
Elongation at break	%	12.6	11.6	11.9	12.6	9.3	13.4
Shear strenght							
Maximum resistance	N/mm^2	46	45	45	43	42	41
Compressive							
Compressive yield strength	N/mm^2	98	95	93	91	87	82
Offset compressive yield	%	11.7	15.1	15.7	12.3	13.0	14.9
Impact Choc Charpy							
Resilience	KJ/m^2	80	80	70	100	90	90
Glass Transition							
Tg1 onset	**°C**	72	91	96	69	83	82
Tg1 onset maximum	**°C**			94			82

		***SR InfuGreen* 810 / SD 8822**			***SR InfuGreen* 810 / SD 4770**		
Curing cycle →		AT + 24 hrs 40 °C	AT + 24 hrs 40 °C	AT + 16 hrs 60 °C	AT + 8 hrs 80 °C	AT + 16 hrs 60 °C	AT + 8 hrs 80 °C
Tension							
Modulus of elasticity	N/mm^2	3000	2900	2700	3160	3100	2700
Maximum resistance	N/mm^2	66	67	61	71	74	70
Resistance at break	N/mm^2	55	60	53	70	68	69
Elongation at max.load	%	3.5	4.4	4.9	3.1	4.2	5.0
Elongation at break	%	4.3	6.1	8.0	3.2	5.1	5.6
Flexion							
Modulus of elasticity	N/mm^2	2900	2800	2700	3250	3000	2770
Maximum resistance	N/mm^2	99	106	101	116	116	115
Elongation at max.load	%	4.4	5.6	6.0	4.6	5.4	6.4
Elongation at break	%	15.5	13.6	13.6	9.8	7.4	7.8
Shear strenght							
Maximum resistance	N/mm^2	43	43	41	47	47	45
Compressive							
Compressive yield strength	N/mm^2	91	91	84	104	100	95
Offset compressive yield	%	11	12	13	11.3	12.8	14.6
Impact Choc Charpy							
Resilience	KJ/m^2	85	88	75	85	83	80
Glass Transition							
Tg1 onset	**°C**	63	74	85	69	84	97
Tg1 onset maximum	**°C**			84			98

Measures undertaken according to the following norms:

Tests carried out on samples of pure cast resin, without prior degassing, between steel plates.

Tension:	*ISO 527 - 2*
Flexion:	*ISO 178*
Charpy impact strength:	*NF T 51-035*
Shear Strength:	*ASTM D 732 - 93*
Compression:	*ISO 604*
Water absorption:	*Internal. Polymerization according to cycle, machining, weighing, time spent in distilled water at 70 °C / 48 hours, weighing 1 hour after emerging,*

Glass transition DSC: *ISO 11357-2: 1999 -5°C to 180 °C under nitrogen gas*
T_{G1} or Onset: 1st point at 20 °C/min *T_{G1} maximum or Onset: second passage*

Glass transition DTMA: *ISO 11357-1 - T_G onset G'* *Temperature ramp 0 °C to 180 °C @ 2°C/min*
ASTM D4065 - T_G peak G''

Physical tests according standard:

Gardner color:	*NF EN ISO 4630*	*Visual method*
Refractive index:	*NF ISO 280*	
Viscosity:	*NF EN ISO 3219*	*Rheometer 50 mm, shear 10 s^{-1}*
Density:	*NF EN ISO 2811-1*	*Pycnometer*
Density solid	*NF EN ISO 845*	
Gel time:	*Cross G' G''*	*Rheometer CP50 - Shear rate 10 s^{-1}*
Green Carbone content:	*ASTM D6866 or XP CEN/TS 16640 Avril 2014*	

AT: *Ambiant temperature*

LEGAL NOTES:

The information given in writing or verbally, in the context of our technical assistance and our trials, do not engage our responsibility. They are given in good faith based on SICOMIN's current knowledge and experience of the products when properly stored, handled and applied under normal conditions in accordance with SICOMIN's recommendations. So, we advise the users of SICOMIN products, to check by some practical trials they are suitable for the envisaged processes and applications. The customer's storage, the use, the implementation and the transformation of the supplied products, are not under our control and your responsibility only will respond for it.

SICOMIN reserves the right to change the properties of its products. All technical data stated in this Product Data Sheet are based on laboratory tests. Actual measured data and tolerance may vary due to circumstances beyond our control.

If our responsibility should nevertheless be involved, it would be, for all the damages, limited to the value of the goods supplied by us and implement by the customer. We guaranty the non-reproachable quality of our products, in the general context of sales and delivery. Users must always refer to the most recent issue of the local Product Data Sheet for the product concerned, copies of which will be supplied on request.

Appendix 2 Product specifications ABB IRB 1200-5/0.9

Numerical optimization and manufacturing of a bio-based 3D structure through robotic filament winding

L.P.J. Krijnen

Eindhoven, May 2023

Product specifications ABB IRB 1200-5/0.9 (ABB, 2022)

Manipulator axes

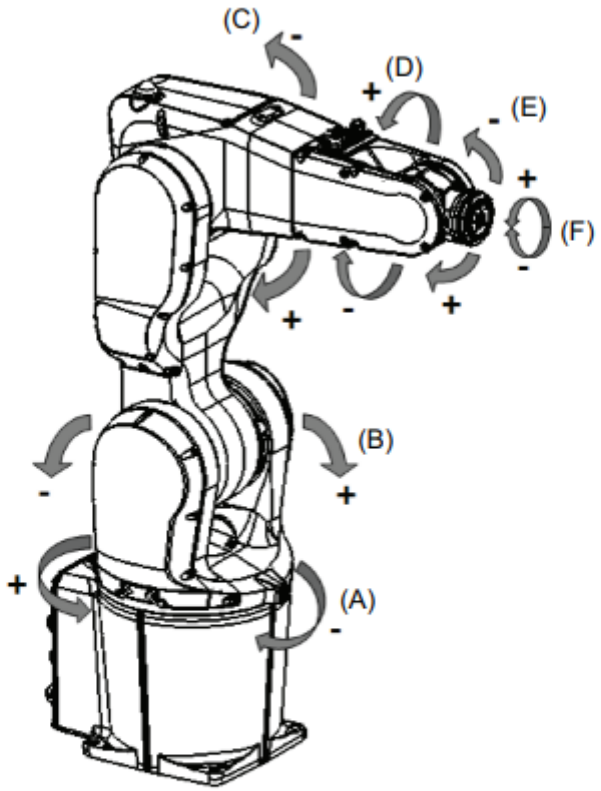

xx1300000365

Position	Description	Position	Description
A	Axis 1	B	Axis 2
C	Axis 3	D	Axis 4
E	Axis 5	F	Axis 6

General

The IRB 1200 is available in two versions and both can be mounted on floor, inverted or on wall in any angle (around X-axis or Y-axis).

Robot type	Handling capacity (kg)	Reach (m)
IRB 1200	5 kg	0.9 m

Weight, robot

The table shows the weight of the robot.

Robot model	Weight
IRB 1200	IRB 1200-5/0.9: 54 kg IRB 1200-7/0.7: 52 kg

Note

The weight does not include tools and other equipment fitted on the robot.

Dimensions IRB 1200-5/0.9

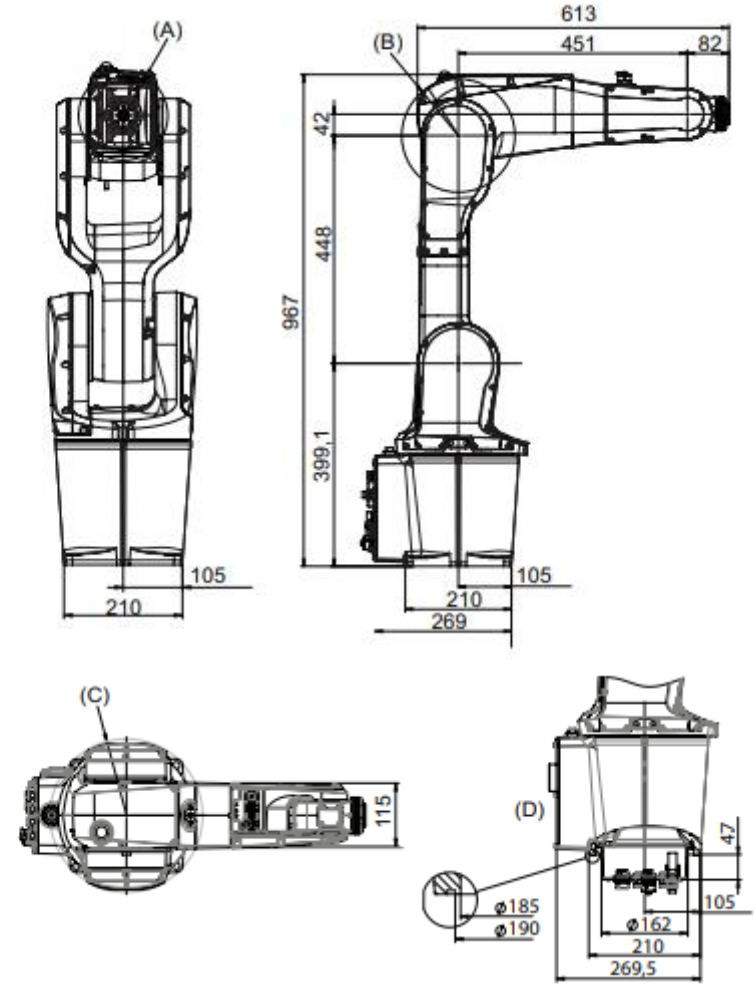

xx1400000339

Pos	Description
A	Minimum turning radius axis 4 R=79 mm
B	Minimum turning radius axis 3 R=111 mm
C	Minimum turning radius axis 1 R=138 mm
D	Valid for option Robot cabling routing, 966-1 From below

Robot tool flange

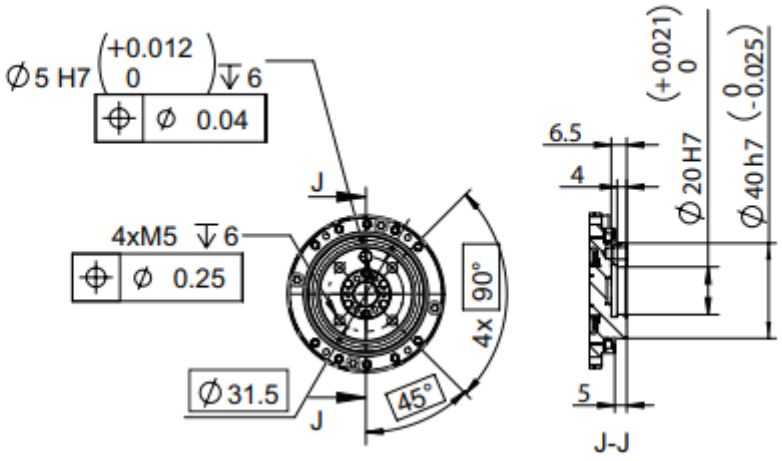

Robot motion

Location of motion	Type of motion	IRB 1200-7/0.7	IRB 1200-5/0.9
Axis 1	Rotation motion	+170° to -170°	+170° to -170°
Axis 2	Arm motion	+135° to -100°	+130° to -100°
Axis 3	Arm motion	+70° to -200°	+70° to -200°
Axis 4	Wrist motion	+270° to -270°	+270° to -270°
Axis 5	Bend motion	±130° (not Hygienic robots) ±128° (Hygienic robots)	±130° (not Hygienic robots) ±128° (Hygienic robots)
Axis 6	Turn motion	Default: +400° to -400° Maximum revolution: ±242[i]	Default: +400° to -400° Maximum revolution: ±242[i]

[i] The default working range for axis 6 can be extended by changing parameter values in the software. Option Independent axis can be used for resetting the revolution counter after the axis has been rotated (no need for "rewinding" the axis).

Working range

IRB 1200-5/0.9 Working range, positions at wrist center and angle of axes 2 and 3

The illustration shows the unrestricted working range of the robot.

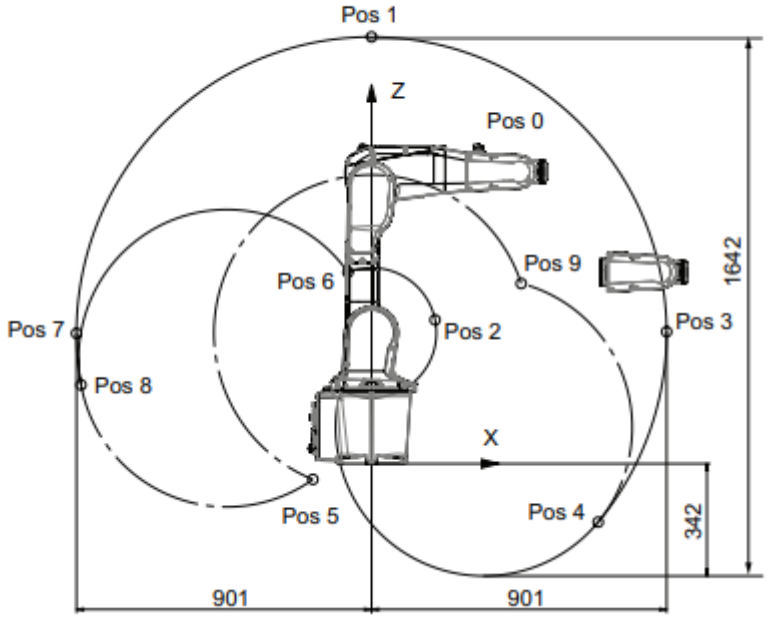

Position in the figure	Positions at wrist center (mm)		Angle (degrees)	
	X	Z	Axis 2	Axis 3
Pos0	451	889	0º	0º
Pos1	0	1300	0º	-85º
Pos2	194	438	0º	+70º
Pos3	901	402	+90º	-85º
Pos4	692	-178	+130º	-85º
Pos5	-179	-48	-100º	-200º
Pos6	-72	583	-100º	+70º
Pos7	-901	397	-90º	-85º
Pos8	-887	240	-100º	-85º
Pos9	458	549	+130°	-200°

Appendix 3 Overview Grasshopper scripts

Numerical optimization and manufacturing of a bio-based 3D structure through robotic filament winding

L.P.J. Krijnen

Eindhoven, May 2023

Grasshopper script numerical optimization

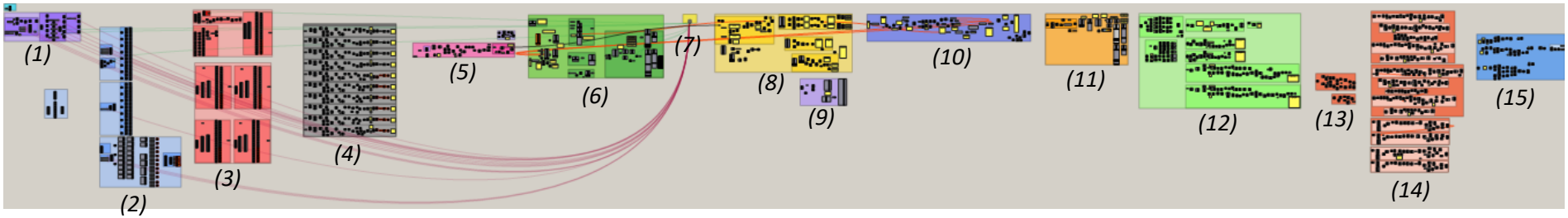

Figure 1 Overview script numerical optimization (Grasshopper)

(1) Define base geometry of the column by filling in the first four parameters.
(2) Define diagrid wire rope design by filling in parameters that determine the angle of the diagonals.
(3) Create geodesic curves based on defined parameters.
(4) Convert geodesic curves to straight line elements based on intersections with vertical lines and rings.
(5) Create straight lines between all intersections and manage which line segments are one line in practice.
(6) First structural analysis in Karamba3D.
(7) Octopus optimization to find design that is minimized in mass and deformation energy, and maximized in stiffness.
(8) Analyse Karamba3D results. Manage data to get maximum stresses per line, total line lengths and cross-sectional area per line.
(9) Create an XML-file using the Koala plug-in, to export the model to SCIA-Engineer.
(10) Iterative sizing optimization using the Anemone plug-in.
(11) Structural analysis of final model using Karamaba3D.
(12) Create an Eulerian winding path for verticals and diagonals.
(13) Create semicircles around the end nodes to wind around bolts, and create a loop around first bolt.
(14) Divide semicircles in points and replace previous end nodes in winding path by new points.
(15) Combine Eulerian paths based on the results of the sizing optimization. After each winding layer the points move 4 mm outwards to prevent collision with previous winded wire ropes. The final winding path is defined as a list of points.

Robot Components script

The input of the Robot Components script is the output of the previous Grasshopper script, namely the list of points defining the winding path.

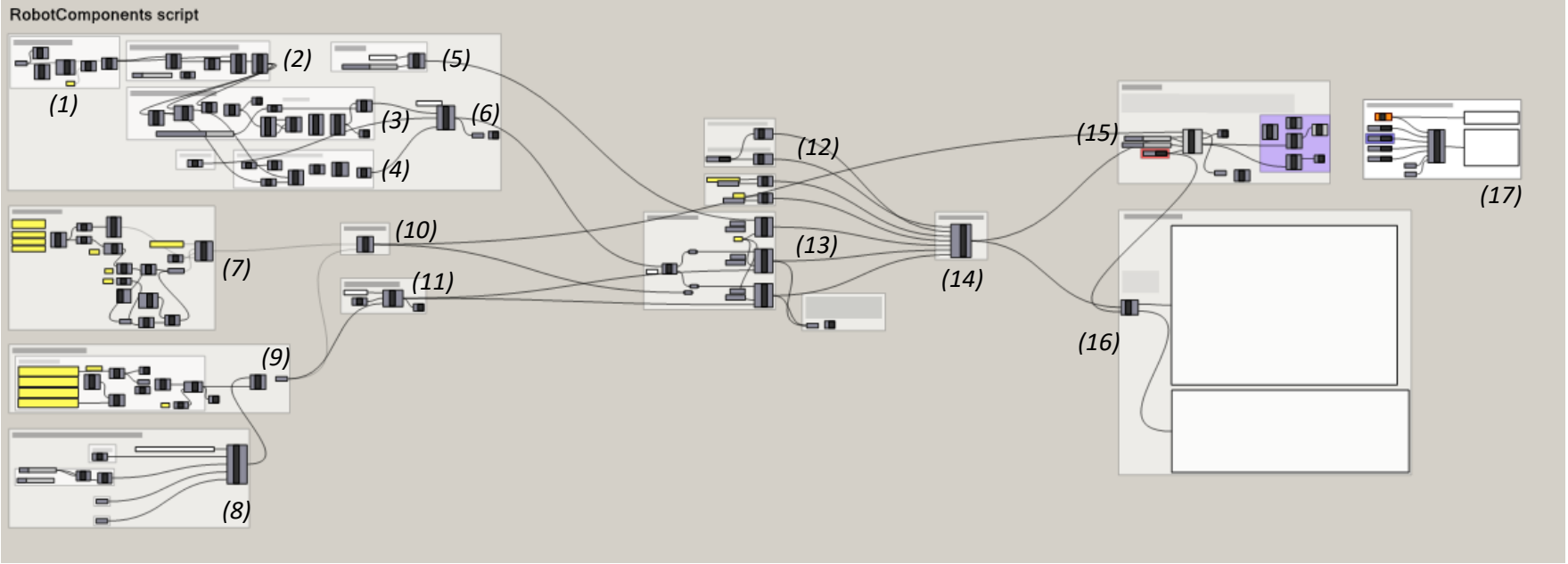

Figure 2 Overview Robot Components script (Grasshopper)

(1) Move all target points outwards to prevent collision between end effector and formwork.
(2) Insert a start- and endpoint to the target points.
(3) Create target planes for moveable work object.
(4) Calculate the external axis value for each target.
(5) Insert initial target position.
(6) Create robot targets.
(7) Define robot end effector.
(8) Define external rotational axis for moveable work object.
(9) Orient external rotational axis to calibrated position of the robot.
(10) Robot definition ABB IRB 1200-5/0.9.

(11) Define moveable work object.
(12) Disable linear configuration control and joint configuration control.
(13) Create movements by defining speed data, movement type and zone data for all target points.
(14) Combine all actions.
(15) Robot path generator.
(16) RAPID-code generator.
(17) Optional: send data directly to RobotStudio.

Appendix 4 Visualizations spaceframe

Numerical optimization and manufacturing of a bio-based 3D structure through robotic filament winding

L.P.J. Krijnen

Eindhoven, May 2023